

Long term trends of currents and hydrography along the equatorial Indian Ocean

A thesis submitted to Goa University
for the award of the Degree of

DOCTOR OF PHILOSOPHY
in
Marine Sciences

By
Chinnu Sachidanandan

Research Guide
P.M.Muraleedharan

Goa University
Taleigao, Goa
March 2020

To,

My parents, Sister and My Husband

Statement

As required under the University Ordinance OB-9A, I state that this thesis entitled “*Long term trends of currents and hydrography along the equatorial Indian Ocean*” submitted to Goa University for the award of the degree of Ph.D. in Marine Sciences is based on studies carried out by me at the CSIR- National Institute of Oceanography, Dona Paula, Goa under the supervision of Dr. P. M. Muraleedharan.

The work is my original contribution and the same has not been submitted on any previous occasion for the award of any degree or diploma in any University or institution. The literature related to the problem investigated has been appropriately cited. Due acknowledgements have been made wherever facilities and suggestions have been availed of.



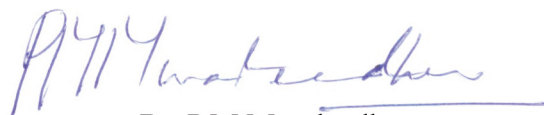
Chinnu Sachidanandan

CSIR- National Institute of Oceanography, Goa
10. March. 2020

Certificate

This is to certify that the thesis entitled “*Long term trends of currents and hydrography along the equatorial Indian Ocean*” submitted by Ms Chinnu Sachidanandan to Goa University for the degree of Doctor of Philosophy in Marine Science, is based on original studies carried out by her under my supervision.

The thesis or any part thereof has not been previously submitted for any other degree or diploma in any University or institution.



Dr. P.M.Muraleedharan
Research Supervisor

10. March. 2020

Acknowledgments

It's time for me to recollect the bitter sweet memories of my Ph.D life, and to express my profound gratitude toward the people who offered strong support and motivation throughout the course of my Ph.D dissertation. It was my father, Mr. P. V. Sachith, a mechanic by profession, who persuaded me to move away from my hometown for my research, so I could experience the outside world and meet people. I am grateful to him for this, because joining *CSIR-National Institute Oceanography* provided me with the wonderful opportunity of harnessing my full potential, and moulding me to stand independent in my field of research. I thank the University Grants Commission immensely, for providing me with the fellowship that supported my research work at the *CSIR- NIO*.

I am thankful to my junior Remya. R. who helped me immerse myself into the basics of FORTRAN and Ferret. It was Miss. Dominique Frances Hoover, who helped me write a good thesis proposal. I am indebted to her for helping me, and the days that I spent with her at *CSIR-NIO* were one of the best times of my life.

Dr. Matthieu Lengaigne, visiting scientist at *CSIR-NIO* from L'OCEAN Laboratory (Paris, France) taught me how to address the practical aspect of a research problem. I would like to extend my heartfelt gratitude towards him, for his patience and dedication in areas of my research work.

I would like to express my sincere gratitude towards three significant people, who practically made my thesis completion possible. They are, my supervisor Dr.P.M. Muraleedharan, Chief Scientist (Retired, *CSIR- NIO*), my father, Mr. P. V. Sachith and my husband Mr. Prasanth. P. S.

My guide, Dr. Muraleedharan, is a person full of optimism, responsibility, dedication and care, who not only supervised my research work, but also patiently listened to my personal sorrows and hardships, and tried to help me cope with these, with sincerity. He constantly encouraged me to meet and discuss with the visiting scientists at *CSIR- NIO*, and those who visit the institution for conferences and workshops. This further helped me to keep abreast of new trends and tunes in the research world. Most people after retirement spend their time with their families and in personal matters, but Dr. Muraleedharan spent a good bit of his time guiding me and helping me complete my thesis. I pray that God grants him strength and a long, fruitful and peaceful life.

It gives me great sorry, knowing that my father is not with me now to share in this joy of completing my Ph.D research. It was his dream that his daughter would get a doctoral degree, so I hope that I have made him proud through my efforts. It was his faith and will power that helped

me embark on this journey. I hereby dedicate this thesis first to my dear father, then to my husband - an epitome of patience who has supported and encouraged me in my work right till the point of its completion. In hard times and times when I doubted my ability to move forward, it was my husband who constantly encouraged me and helped me realize that I can complete my journey. He always made himself available, despite his busy work schedule as a Logistics Coordinator. Thank you dear for your care and support to conquer my dream.

I extend my sincere thanks to Dr. Basil Mathew, HoD, Department of Physical Oceanography, KUFOS, who guided me on the “*Changes in inter-annual variability of temperature at the equatorial Indian Ocean in different epochs*” as part of Ph.D work and corrected thesis chapter. I would like to thank Dr. M. T. Babu and Dr. V. V. Gopalakrishna for giving an opportunity to join the XBT project for three months at CSIR-NIO, which helped me to complete my research paper publication. I would like to express my gratitude to my co guide Prof .H.B. Menon, Dean, School of Earth Atmospheric and Ocean Sciences, Goa University, for his immense understanding and patience in helping me submit the thesis. I am thankful to the office staff, Mr. Yeshwant at School of Earth Atmospheric and Ocean Sciences for his support, which made the academic interactions with the university easy.

I would like to extend my heartfelt thanks to Dr. Pankajakshan, Dr. M.R. Ramesh Kumar (VC's nominee) and Dr. Prasanna Kumar from CSIR- NIO for their valuable advice and suggestions regarding my research work. I am thankful to Dr. Benny N. Peter, adjunct professor from KUFOS, helped in clarifying my doubts on variability of hydrographic properties of the Indian Ocean on various time scales. I sincerely thank Dr. R. Sajeev and Dr. P. K. Saji from CUSAT who motivated me during my Ph.D.

Here I would like to thank my classmates, Mr. Sivakumar, Mr. Renosh, Mr. Amol, Mr. Praveen, Mrs. Betty, Mr. Manu, Mr. Saheed, Mrs. Divya, Mr. Jineesh and Mr. Renjith who made my CSIR-NIO life more colourful and stress free. I thank all my juniors, especially Mr. Charles Antony and Mr. Nidheesh, who helped me in clearing doubts on data analysis. I am grateful to Mrs. Ashwini Anirudhan who helped me during my last days at CSIR- NIO. Without her help, those days would have been very difficult for me. I thank Mr. Jesbin who helped me in submitting the thesis on time at the Goa University. During my term at CSIR-NIO, I lost a loving junior of mine, Gokul, who was like a younger brother to me. He cheered me with his wits and helped me on personal errands. I will always cherish the moments I spent with him at CSIR-NIO. I am grateful to my former colleagues Dr. Umesh and Dr. Sajan for their encouragement and well wishes throughout the term of my Ph.D.

Last but not least, my mother Mrs. C.P. Sunandha and my younger sister Miss. Chinju P. Sachith, the two people who patiently waited for this thesis completion despite the bad situation our family was going through. It was their constant prayers and blessings that made this thesis complete. I am grateful to them for being with me on this journey. I would like to thank my

mother in law and father in law for believing in me and providing me with the support I needed during my Ph.D life.

I am grateful to the organizations that made their data available for use in my thesis and during the course of my research. I acknowledge the DRAKKAR project for providing NEMO model simulations. I thank the data management division at *CSIR-NIO*, Goa, for giving me access to ADCP data; APDRC and INCOIS for the ARGO data; the NASA Physical Oceanography Data Center, PO.DACC for OSCAR surface current data; PEARL, NOAA for RAMA mooring data; and the Met Office, UK for HADISST data. I also thank the University of Hamburg for GECCO2 simulations from the ICDC, and the ECMWF for the ORAS4 simulations.

Above all, I owe it all to Almighty God for granting me the wisdom, health and strength to undertake this research work and enabling its completion.

CSIR- National Institute of Oceanography

Chinnu Sachidanandan

Abstract

For studying the dynamical response of ocean to the forcing on various scales, latitudinal divisions of ocean such as Equatorial, Mid-latitudes and High- latitudes are necessary. This sub division is logical since the planetary vorticity and the meridional gradients in thermal forcing on Earth are changing with the latitude. Among these three regions, equatorial regions are the most significant due to the diversity in the forcing mechanisms. They play crucial role in regulating the world's climate scenario. Due to the disappearance of Coriolis force at the equator, these regions exhibit different dynamics other than mid-latitudes and high latitudes. Equatorial regions receive maximum amount of solar radiation which is released to atmosphere in the form of latent heat that sub sequentially modifies the atmospheric general circulation. High surface water temperature, complexity in different water mass mixing, strong vertical motions and the intense exchange of energy between the ocean and atmosphere are the peculiarities of this region. Due to the reversing Coriolis effect on either side, the equator acts as a wave guide for the propagation of waves, which have a major role in adjusting Equatorial Ocean to unsteady wind forcing.

Ocean currents and atmosphere winds themselves were nature's best contributors in regulating the global climate by redistribution of dynamic and thermodynamic properties within them and they dominate mainly the inter-annual fluctuations in the global weather patterns. So, the equatorial processes are always the centre of attraction for an oceanographer to understand the influence of ocean on the atmosphere. Even though the emergence of satellite oceanography contributed immensely to study the ocean surface in both space and time, it hardly contributed to the understanding of the subsurface due to very sparse data coverage. During the recent years the progress in ocean modelling helps one to study in detail the temporal and spatial structure of currents and hydrography in detail.

Unlike Pacific and Atlantic, Indian Ocean remains to be the least studied regions of the world oceans although it has the potential to serve as the unique laboratory with several complexities due to its peculiar geographical positioning. By realising this potential, the global oceanographic community has started showing interest in this unexplored semi enclosed basin. Several mooring equipment's have been deployed at the equatorial regions by national and

international agencies to collect long time observational time series data of currents and hydrography apart from surface meteorological parameters. Subsequent to this, a collaborative effort had been made to deploy ARGO (Array of Real time Geostrophic Oceanography) floats to cover the entire global oceans. That is the first attempt to put in place a global real time *in situ* observing system that provides real-time data for use in climate, weather, oceanographic and fisheries research.

The present thesis aims at investigating inter-annual variability of currents and waves in the equatorial Indian Ocean (EIO) and the changes in inter annual equatorial Indian Ocean temperature in different epochs along with the long-term variability and trends in hydrography at both surface and subsurface depths. As the observational data for currents and hydrography at the equatorial Indian Ocean are limited for long term study, this thesis made an attempt to improve the understanding about the inter annual to decadal scale variability at equatorial Indian Ocean through model and reanalysis data sets.

This thesis made an attempt to study the main features of equatorial Indian Ocean currents and their response to inter annual climate modes. The present study revealed two main modes of equatorial current variability on interannual time scale. The dominant mode exhibited maximum variability in fall and largely described the variability of the fall Wyrcki jet intensity. The second mode was maximum in winter and largely described the inter-annual variability of the subsurface currents in winter, with a weaker surface expression. Fall Wyrcki jet intensity was modulated by Indian Ocean Dipole (IOD) by modulating the equatorial wind system during that season. Delayed effect of IOD wind signal on to equatorial thermocline modulates the subsurface currents variations until December. Influence of El Niño/Southern Oscillation (ENSO) to the equatorial Indian Ocean current system was weak and delayed. Also, the remote influence of ENSO intensifies the winter Equatorial Undercurrent in the Indian Ocean.

The inter annual variability of equatorial Indian Ocean temperature consists of two main modes, first mode is Indian Ocean Basin Mode warming associated with ENSO and secondary mode is associated with IOD. The correlation between the first and second modes with the climate indices revealed that ENSO had strong influence on the equatorial temperature system.

The present study also addressed the changes in inter-annual equatorial Indian Ocean temperature before (before 1976) and after the climate shift (after 1976) period. During PRE76 the ENSO related warming occurred during winter while its peak shifted to spring and summer with increased intensity in POST76. The IOD signals were strongest during September-November during both epochs. The IOD signals were strongest in the thermocline region during both epochs. The correlation between surface and subsurface IOD signals weakened from PRE76 to POST76. The co-occurring events of ENSO and IOD which were less frequent before the climate shift increased considerably thereafter. These decreased the strength of ENSO induced basin scale warming while at the same time they increased the strength of IOD induced fall warming after the climate shift.

Present study made an attempt to study decadal variability and trends in equatorial Indian Ocean temperature and salinity at both surface and at depths. On decadal scale, the mean pattern of temperature at EIO was the eastern (western) equatorial warming (cooling) and was more prevalent during 1976-95. The subsurface temperature patterns also corroborated well with these dynamics during this period in the decadal time scale. The Wyrcki Jet intensification (negative IOD) is therefore, the mean pattern of variability during this period. However, prior to 1976 and post 1995 periods, due to the prevailing easterlies when the descending branch of walker cell migrated to the maritime continent brought upwelling at the Sumatra coast and down welling off Somalia. At depths, the warmer thermocline at west appeared to shoal towards east causing upwelling off Sumatra coast during these periods corroborated with the surface dynamics. Therefore, the Wyrcki Jet reduction (positive IOD) is the mean pattern of variability during this period. The surface and subsurface salinity variabilities in the decadal time scale supported the dynamics explained in the temperature field.

The EIO temperature indicated a warming trend of $0.12\text{ }^{\circ}\text{C}/\text{decade}$ which was higher than the Pacific and Atlantic since 1950s with an accelerated warming in post 1970 period. The eastern half of the EIO is warming much higher than the western counterpart during 1950-2014 period in the decadal time scale. The eastern equatorial warming trend, however, intensified between 1950 and 1990, on the contrary, it witnessed accelerated cooling in the 1980-2014 period especially the south-eastern equatorial Ocean. On the other hand, the subsurface layer (80-150m)

appears to be cooling in the decadal scale with accelerated cooling at the western equatorial IO. The spatial trend in sea surface salinity during 1960-2014 periods, on an average, indicated a positive slope all along the equator with slightly steeper ones occupying the eastern equatorial ocean. The contrast was much more severe during the moderate warming period of 1960-1990 with steeper slopes indicating that the surface water of Arabian Sea and the equatorial waters become more and more saltier and accelerated freshening in southern Arabian Sea and Bay of Bengal under the notion of increasing (decreasing) salinity when evaporation (precipitation) exceeds precipitation (evaporation) in the warming climate.

Publication from thesis

Sachidanandan C., Lengaigne M, Muraleedharan P.M, Mathew B. (2017) Interannual variability of zonal currents in the equatorial Indian Ocean: respective control of IOD and ENSO, Ocean Dynamics, DOI 10:1007/s10236-017-1061-4.

Contents

Statement.....	iii
Certificate.....	iv
Acknowledgement.....	v
Abstract.....	viii
Contents.....	xii
Acronyms.....	xv
List of Figures.....	xviii
List of Tables.....	xx

1. General Introduction

1.1 Motivation	1
1.1.1 Uniqueness of Tropical Indian Ocean	1
1.2 Equatorial Dynamics and Summer monsoon rainfall.....	2
1.3 The Climate Link beyond the impact on ISMR.....	4
1.4 Organization of the thesis	5
1.4.1 The thesis manuscript is organized as follows:	5

2. Background information and relevance of the present work

2.1 Equatorial regions: A global perspective	6
2.2 Equatorial Regions: An Indian Ocean perspective	9
2.3 Seasonal Indian Ocean climate.....	18
2.4 Equatorial Indian Ocean: Inter-annual variability	22
2.4.1 An overview.....	22
2.4.2 Inter annual climate modes	22
2.4.3 Equatorial Indian Ocean response.....	25
2.4.4 The tropical Indian Ocean.....	27
2.4.5 The Climate variability	27
2.4.6 Air-Sea Interface of the Tropical belt.....	28
2.4.6.1 Wind Forcing	28
2.4.6.2 Thermocline topography.....	29
2.4.6.3 Sea Surface Temperature and Precipitation	30
2.4.7 Upper Ocean Circulation.....	30
2.4.7.1 Equatorial Indian Ocean	32
2.4.7.2 Meridional Overturning Cells	33
2.4.7.3 Cross-Equatorial Cell.....	33
2.4.8 Inter-ocean Circulations	35
2.4.8.1 Indonesian through flow	35
2.4.9 Oceanic Processes	36
2.4.9.1 Upwelling and Thermocline Depth.....	36
2.4.9.2 Remote Forcing triggered by planetary Waves	36
2.4.9.3 Bjerknes Feedback.....	37

3. Data and Methods

3.1 Introduction	39
3.2 Inter-annual variability of currents and waves in the equatorial Indian Ocean.....	39

3.2.1	Model data set	39
3.2.2	Observational data set	40
3.2.2.1	Moored Buoy/ADCP data	40
3.2.2.2	OSCAR data	41
3.2.3	Model validation	42
3.2.3.1	The seasonal circulation – Surface currents	42
3.2.3.2	The seasonal circulation- Currents at the depth	44
3.2.3.3	Inter-annual circulation – Surface currents	46
3.2.3.4	Inter-annual circulation- currents at depths.....	46
3.3	Changes in inter-annual variability of surface temperature at the equatorial Indian	48
3.3.1	Model data set	48
3.3.2	Climate indices definition	49
3.3.3	Statistical methods	50
3.3.3.1	Empirical Orthogonal Function Analysis.....	50
3.3.3.2	Partial Regression Analysis.....	51
3.3.3.3	Partial Correlation Analysis	51
3.3.3.4	Fisher’s r to z transformation for comparing correlations.....	52
3.4	Variability and trend analysis of hydrographical parameters in the decadal time scale.....	53
3.4.1	Trend analysis	53
3.4.2	Observational data products	54
3.4.3	Reanalysis/model data products	55
3.4.4	Validation of model data – At the surface	56
3.4.4.1	ORAS4 and HADISST data.....	57
3.4.4.2	GECCO2 and HADISST data.....	58
3.4.5	Validation of vertical profiles of temperature from ORAS4 and GECCO2	59
3.4.5.1	ORAS4 with ARGO data	59
3.4.5.2	GECCO2 with ARGO data	61
3.4.6	Validation of vertical profiles of salinity from ORAS4 and GECCO2	63
3.4.6.1	ORAS4 with Argo data	63
3.4.6.2	GECCO2 with Argo data	64
3.5	Limitations in the validation experiment in analysing decadal trends/variability.....	66
4.	General description of the inter-annual current variations at the equatorial Indian Ocean	
4.1	An Overview	68
4.2	Brief description of the data and method.....	69
4.3	Inter-annual current variability at the Equatorial Indian Ocean.....	69
5.	Mechanisms responsible for the inter-annual variability of the Indian Ocean Equatorial current system	
5.1	An overview of the equatorial dynamics	76
5.2	Mechanisms responsible for the subsurface current variability.	77
5.3	Respective influence of IOD and ENSO on equatorial current variations.....	79
6.	Changes in inter-annual variability of temperature at the equatorial Indian ocean in different epochs	
6.1	An overview	86
6.2	Climate Shift Era	87
6.3	Brief description of Data and Methodology	87
6.4	Main patterns of Inter-annual temperature variations on PRE76 and POST76 epochs	90
7.	Variability and trend analysis of hydrographic parameters in the decadal time scale	

7.1	Introduction	101
7.2	The data sets used in the decadal trend/variability analysis.....	102
7.2.1	Decadal variability of Temperature at the equatorial Indian Ocean	102
7.2.2	Decadal variability of Salinity at the equatorial Indian Ocean.....	105
7.2.3	Linear trend analysis of temperature and salinity in decadal time scale at the.....	107
7.2.3.1	Linear trends in temperature at the surface	107
7.2.3.2	Linear trends in temperature at depths	109
7.2.3.3	Linear trends in salinity at the surface	111
7.2.3.4	Linear trends in salinity at depths	113
8.	Summary and Conclusions	
8.1	Summary	115
8.2	Concluding remarks.....	120
8.3	Future Programs	124
	References.....	125
	List of Publications	149

List of acronyms

ADCP	Acoustic Doppler Current Profiler
APB	Autonomous Pinniped Bathythermograph
AMSRE	Advanced Microwave Scanning Radiometer Earth observing System
APDRC	Asia Pacific Data Research Center
ARGO	Array of Real Time Geostrophic Oceanography
ARMEX	ARabian sea Monsoon EXperiment
AS	Arabian Sea
AVISO	Archiving Validation and Interpretation of Satellite Oceanographic data
BoB	Bay of Bengal
BOBMEX	Bay Of Bengal Monsoon Experiment
CEC	Cross Equatorial Cell
COAPS	Center for Ocean-Atmospheric Prediction Studies
CTD	Conductivity Temperature Depth
DFS	DRAKKAR Forcing Set
DJF	December January February
DMI	Dipole Mode Index
DOD	Department of Ocean Development
EACC	East African Coastal Current
ECC	Equatorial Counter Current
ECCO	Estimating the Circulation and Climate of the Ocean
ECMWF	European Center for Medium- Range Weather Forecasts
EEIO	Eastern Equatorial Indian Ocean
EIO	Equatorial Indian Ocean
EJ	Equatorial Jet
ENSO	El Niño / southern Oscillation
EN3v2	Enhanced Ocean Data Assimilation and Climate Prediction/ENSEMBLES3(version2)
EOF	Empirical Orthogonal Function
E-P	Evaporation – Precipitation
EQUINOO	Equatorial Indian Ocean Oscillation
ERA	ECMWF Re-Analysis
EUC	Equatorial Under Current
GCM	General Circulation Model
GECCO	German contribution of the Estimating the Circulation and Climate of the Ocean
GOCO	Gravity Observation COmbination
JGOFAS	Joint Global Ocean Flux Study Arabian Sea Experiment
HadISST	Hadley Centre Global Sea Ice and Sea Surface Temperature
ICOADS	International Comprehensive Ocean-Atmospheric Data Set
IIOE	International Indian Ocean Expedition
INCOIS	Indian National Center for Ocean Information Systems
INDEX	INDian Ocean EXperiment
INDOOS	INDian Ocean Observing System
IOBM	Indian Ocean Basin Mode
IOD	Indian Ocean Dipole
IODMI	Indian Ocean Dipole Mode Index
IODZM	Indian Ocean Dipole / Zonal Mode
IO	Indian Ocean

ISCCP-FD	International Satellite Cloud Climatology Project-Flux Data
ISMR	Indian Summer Monsoon Rainfall
ITCZ	Inter Tropical Convergence Zone
ITF	Indonesian Through Flow
JAMSTEC	Japan Agency for Marine-Earth Science and Technology
JASME	Joint Air-Sea Monsoon Experiment
JASON	Joint Altimetry Satellite Oceanography Network
JPL	Jet Propulsion Laboratory
MAM	March April May
MJO	Madden Julian Oscillation
MIT	Massachusetts Institute of Technology
MONEX	MONsoon EXperiment
MRG	Mixed Rossby Gravity
NASA	National Aeronautics and Space Administration
NCEP/NCAR	National Centers for Environmental Prediction/National Center for Atmospheric Research
NE	North East
NEC	North Equatorial Current
NEMO	Nucleus for European Modelling of the Ocean
NETCDF	NETwork Common Data Format
NH	Northern Hemisphere
NIO	National Institute of Oceanography
NMC	North-east Monsoon Current
NOAA	National Oceanic and Atmospheric Administration
NOPP	National Oceanographic Partnership Program
NW	North West
OCS	Ocean Climate Station
OGCM	Ocean General Circulation Model
ONI	Oceanic Niño Index
OOS	Ocean Observation Studies
ORAS	Ocean Reanalysis/Analysis System
OSCAR	Ocean Surface Current Analysis Real-time
PCA	Principal Component Analysis
PC	Principal Component
PIRATA	PredIction and Research moored Array in the Tropical Atlantic
PMEL	Pacific Marine Environmental Laboratory
POP	Parallel Ocean Physics
PSU	Practical Salinity Unit
QBO	Quasi Biennial Oscillation
RAMA	Research moored Array for African-Asian-Australian Monsoon Analysis and prediction
RMS	Root Mean Square
SCTR	Seychelles Chagos Thermocline ridge
SE	South East
SEC	South Equatorial Current
SECC	South Equatorial Counter Current
SH	Southern Hemisphere
SLP	Sea Level Pressure
SMC	South-west Monsoon Current
SO	Southern Oscillation
SODA	Simple Ocean Data Assimilation

SON	September October November
SSH	Sea Surface Height
SSHA	Sea Surface Height Anomaly
SSM/I	Special Sensor Microwave/ Imager
SSS	Sea Surface Salinity
SST	Sea Surface Temperature
SSTA	Sea Surface Temperature Anomaly
STC	Southern subTropical Cell
TAO/TRITON	Tropical Atmosphere Ocean/TRIangle Trans-Ocean buoy Network
TIO	Tropical Indian Ocean
TOGA	Tropical Ocean Global Atmosphere
TOPEX/POSEIDON	TOPOgraphy Experiment-Positioning Ocean Solid Earth Ice Dynamics Orbital Navigator
WOA	World Ocean Atlas
WOCE	World Ocean Circulation Experiment
XBT	eXpendable Bathy Thermograph

List of Figures

Figure 2. 1 RAMA buoys	10
Figure 2. 2 NIO moorings	11
Figure 2. 3 Argo floats	12
Figure 2. 4 Illustration of Argo float deployment, profiling and transmitting via satellite	13
Figure 2. 5 Monsoonal system of Indian Ocean	14
Figure 2. 6 Surface circulation of Indian Ocean	16
Figure 2. 7 Boreal summer and winter net heat flux and wind stress and SST and precipitation fields in the IO	19
Figure 2. 8 A model of surface temperatures, winds, areas of rising air, and the thermocline in the tropical Pacific during El Niño, normal, and La Niña conditions	23
Figure 2. 9 Indian Ocean Dipole modes	24
Figure 2. 10 Time scales of various climate modes in IO	28
Figure 2. 11 Monsoon wind stress fields from the 1990–1998	29
Figure 2. 12 Schematic representation of identified current branches during the summer (southwest) monsoon	31
Figure 2. 13 As in Figure 3 but for the winter (northeast) monsoon	32
Figure 2. 14 Indian Ocean cross equatorial cell shown schematically	34
Figure 2. 15 Schematic of the positive Bjerknes atmosphere-ocean feedback and the negative biological feedback in the eastern equatorial Pacific	38
Figure 3. 1 Location map of Acoustic Doppler Current Profiler moorings	41
Figure 3. 2 Longitude-time evolution of seasonal climatology of equatorial zonal surface currents from OSCAR dataset and model outputs. The corresponding zonal wind stress climatology from the model is overlaid on each panel	43
Figure 3. 3 Correlation map between the seasonal currents from OSCAR and the model output. These seasonal currents are computed over the common 1993–2007 period	44
Figure 3. 4 Vertical section of seasonal equatorial zonal currents and temperature at 80.5° E and 90° E from NIO-ADCP, RAMA moorings and model output	45
Figure 3. 5 Correlation values for vertical section of seasonal equatorial zonal currents at (a) 77° E (NIO-ADCP), (b) 80.5° E (RAMA) and (c) 90° E (RAMA) between moorings and model output	46
Figure 3. 6 Standard deviation maps of interannual zonal surface currents from OSCAR dataset and model output; And correlation maps between interannual zonal current anomalies derived from OSCAR and model outputs	47
Figure 3. 7 Interannual anomalies of equatorial zonal currents at (a) 80.5° E and (b) 90° E from RAMA buoys and simulation. Corresponding correlations between modelled and observed interannual anomalies of equatorial zonal currents at 80.5° E and 90° E	48
Figure 3. 8 Climate indices calculated using HADISST data from 1958 to 2007	50
Figure 3. 9 Standard deviations from HADISST and ORAS4 data are plotted at the equatorial domain during 1960–2014 periods. Coefficient of correlation and RMS error between model and <i>in situ</i> data are plotted during the same period	57
Figure 3. 10 Standard deviations from HADISST and GECCO2 data are plotted at the equatorial domain during 1960–2014 periods. Coefficient of correlation and RMS error between model and <i>in situ</i> data are plotted during the same period	58
Figure 3. 11 Correlation and Root mean square error between ARGO and ORAS4 vertical section of temperature for the period 2002 to 2014 for 1° S–62° E, 5° N–62° E, 7° S–70° E and 10° S–100° E	60
Figure 3. 12 Correlation and Root mean square error between ARGO and GECCO2 vertical section of temperature for the period 2002 to 2014 for 1° S–62° E, 5° N–62° E, 7° S–70° E and 10° S–100° E	62

Figure 3. 13 Correlation and Root mean square error between ARGO and ORAS4 vertical section of salinity for the period 2002 to 2014 for 1° S-62° E, 5° N-62° E, 7° S-70° E and 10° S-100° E.....64

Figure 3. 14 Correlation and Root mean square error between ARGO and GECCO2 vertical section of salinity for the period 2002 to 2014 for 1° S-62° E, 5° N-62° E, 7° S-70°E and 10° S-100°E.....65

Figure 4. 1 Time series (PCs) of surface and subsurface EOFs and monthly standard deviation of normalized principal components of the first EOF of inter-annual surface zonal current anomalies and equatorial vertical section of inter-annual zonal current anomalies from the model over the 1960–2007 period. The corresponding first EOF pattern of surface zonal current anomalies and equatorial vertical sections of zonal current anomalies are in right panel. Climatological fall currents (September–November) are overlaid.....70

Figure 4. 2 Time series (PCs) of surface and subsurface EOFs and monthly standard deviation of normalized principal components of the second EOF of inter-annual surface zonal current anomalies and equatorial vertical section of inter-annual zonal current anomalies from the model over the 1960–2007 period. Corresponding second EOF pattern of surface zonal current anomalies and equatorial vertical sections of zonal current anomalies are in right panel. Climatological winter currents (December–February) are overlaid.....71

Figure 4. 3 Lag correlation of the principal components of EOF1 and EOF2 of surface and equatorial vertical section of inter-annual zonal current anomalies.....73

Figure 4. 4 Sea surface temperature and wind stress anomalies regressed onto of the principal components of EOF1 and EOF2 of the equatorial vertical section of inter-annual zonal current anomalies. Simple lag-correlation of PC1 and PC2 of equatorial vertical section of inter-annual zonal current anomalies onto IOD and ENSO indices over the 1960–2007 periods.....74

Figure 5. 1 20 °C isotherm depth anomalies regressed onto the principal components of EOF1 and EOF2 of inter-annual equatorial subsurface zonal current analysis. And for wind stress curl and wind stress anomalies.77

Figure 5. 2 Simple regression of vertical section of zonal currents and equatorial zonal winds averaged over the [2°N–2° S; 65° E– 85° E] region onto DMI index and ENSO index over the 1960–2007 period. Corresponding vertical sections of climatological zonal currents are overlaid80

Figure 5. 3 Partial regression of 20 °C isotherm depth anomalies, wind stress curl and wind stress onto DMI index with the influence of ENSO index removed and ENSO index with the influence of the DMI index removed over the 1960–2007 period for fall, winter and spring.81

Figure 5. 4 Partial regression of vertical section of zonal currents, equatorial zonal winds and zonal surface currents averaged over the [2° N–2° S; 65° E–85° E] region, zonal subsurface currents averaged over the [2° N–2° S; 65° E–85° E; 80–180 m] region and equatorial thermocline averaged over the [5° N–5° S; 80° E–100° E] region onto DMI index with the influence of ENSO index removed and ENSO index with the influence of the DMI index removed over the 1960–2007 period. Corresponding vertical sections of climatological zonal currents are overlaid.....83

Figure 6. 1 First mode of EOF patterns for surface (a- PRE76 period & c-POST76 period) and vertical fields (b- PRE76 period & d-POST76 period) and corresponding time series of normalized principal components (e- PRE76 period & f-POST76 period; Black line is surface and red line is vertical field). 1960-1976 periods are called PRE76 and 1977-2007 periods are called POST76. Correlation between the surface and vertical fields are written inside the figure..... 91

Figure 6. 2 Monthly standard deviation of normalized principal components of surface and vertical modes of first EOF of inter annual temperature anomaly for 1960-1976(a) and 1977-2007(b). 92

Figure 6. 3 Second mode of EOF patterns for surface (a- PRE76 period & c-POST76 period) and vertical fields (b- PRE76 period & d-POST76 period) and corresponding time series of normalized principal components (e- PRE76 period & f-POST76 period; Black line is surface and red line is vertical field). 1960-1976 periods are called PRE76 and 1977-2007 periods are called POST76. Correlation between the surface and vertical fields are written inside the figure..... 94

Figure 6. 4 Monthly standard deviation of normalized principal components of surface and vertical modes of second EOF of inter annual temperature anomaly for 1960-1976(a) and 1977-2007(b).	95
Figure 6. 5 Lead-lag correlation between surface and vertical fields of first EOF for PRE76 (a) and POST76 (b) period	96
Figure 6. 6 Lead-lag correlation between surface and vertical fields of second EOF for PRE76 (a) and POST76 (b) period	97
Figure 6. 7 Simple regression analysis performed between Indian Ocean surface temperature (shaded) onto IOD and ENSO indices for PRE76 (a & c) and POST76 (b & d) period. Vectors are windstress anomalies.	98
Figure 6. 8 Partial correlation analysis performed between the first (PC1) and second (PC2) EOFs of equatorial Indian Ocean surface temperature onto IOD and ENSO indices for PRE76 (a & c) and POST76 (b & d) period. Red line is ENSO and black line is IOD.	99

Figure 7. 1 EOF analysis performed on surface temperature (a & b) and temperature at depths (c & d) from GECCO2 data for the period 1950-2014. The spatial (EOF) and temporal (Principal Component) patterns were displayed in left and right panels respectively. The temperature at depths was averaged between 10°N and 10°S before submitting to EOF analysis.	103
Figure 7. 2 Empirical orthogonal function patterns for surface salinity (a&b) and vertical section of salinity(c&d) from ORAS4 model data. The spatial (EOF) and temporal (Principal Component) patterns are displayed in left and right panels respectively. The salinity at depths are averaged between 10°N and 10°S before submitting to EOF analysis.	105
Figure 7. 3 Spatial distribution of the slopes of linear trend of surface temperature anomaly determined grid-wise in decadal time scale over the tropical Indian Ocean using GECCO2 model data for the period 1950 – 2014 (a), 1950-1990 (b) and 1980- 2014 (c). The linear trend of monthly mean temperature anomaly computed within the equatorial box bounded by 10°N-10°S latitude and 40°E-110°E longitude for the period 1950-2014 (d). 7year running mean is applied in all cases to remove seasonal and inter annual oscillations to highlight the decadal signals.	108
Figure 7. 4 Vertical distribution of the slopes of linear trend of temperature anomaly in decadal time scale along the equatorial Indian Ocean by averaging the meridional values using GECCO2 model data for the period 1950 – 2014 (a). The linear trend of monthly mean temperature anomaly (80-150m) computed within the equatorial box bounded by 10°S-10°N latitude and 40°E-11°0E longitude for the period 1950-2014 (b). Seven year running mean is applied to remove seasonal and inter annual oscillations to highlight the decadal signals.	110
Figure 7. 5 Spatial distribution of the slopes of linear trend of surface salinity anomaly determined grid-wise in decadal time scale over the tropical Indian Ocean using ORAS4 model data for the period 1960 – 2014 (a), 1960-1990 (b) and 1980-2014 (c). The linear trend of monthly mean salinity anomaly computed within the equatorial box bounded by 10°N-10°S latitude and 40°E-110°E longitude for the period 1960-2014 (d). Seven year running mean is applied in all cases to remove seasonal and inter annual oscillations to highlight the decadal signals.	111
Figure 7. 6 Vertical distribution of the slopes of linear trend of salinity anomaly in decadal time scale along the equatorial Indian Ocean by averaging the meridional values using ORAS4 model data for the period 1960 – 2014 (a). The linear trend of monthly mean salinity anomaly (80-150m) computed within the equatorial box bounded by 10° S-10° N latitude and 40° E-110° E longitude for the period 1950-2014 (b). Seven year running mean is applied to remove seasonal and inter annual oscillations to highlight the decadal signals.	113

List of Tables

Table 3. 1 Details of ADCP data used for model validation.	41
Table 3. 2 Brief description of observational and model data used in this chapter	56

General Introduction

1.1 Motivation

1.1.1 Uniqueness of Tropical Indian Ocean

Several features make the Indian Ocean unique. Unlike Pacific and Atlantic the Indian Ocean is land-locked at the north promoting differential heating that give rise a peculiar air sea interaction process that drives the strongest event on Earth called Indian Ocean monsoon which causes large scale seasonal variations in ocean currents including reversal of Somali Current and Indian Monsoon Current. The Asian land mass at the north blocks heat export thereby preventing ventilation of the Indian Ocean thermocline. The seasonal reversal of monsoon current causes the reversal of cross equatorial heat and momentum transport that has tremendous implications on the regional climate variability. South of the equator the Indian Ocean is gaining heat during June-October during the austral winter and loosing heat during November – March during the austral summer. Another uniqueness of the equatorial Indian Ocean compared to other two major Oceans is the semi-annual appearance of eastward flowing jet (Wyrтки, 1973) during the monsoon transition periods (April-May and October-November) and the absence of equatorial upwelling in the annual scale.

It is also worth mentioning that the northern extent of the equatorial domain of the Indian Ocean is exposed to two contrasting water bodies called Arabian Sea and Bay of Bengal. The saline Arabian Sea and its adjoining water bodies (Persian Gulf and Red Sea) are dominated by evaporation while the low saline Bay of Bengal is dominated by runoff from all major rivers of India, Bangladesh and Myanmar. The interaction of these two contrasting water bodies happens through the seasonally reversing circulation pattern. The surface and sub-surface zonal currents along the equator can easily be tracked by the east-west water masses of contrasting characteristics. During boreal summer the Bay of Bengal contributes more than half of the runoff water ($\sim 2950 \text{ km}^3$) to the Indian Ocean and flows into the Arabian Sea while part of it flows

south across the equator and joins with low saline Pacific equatorial water seeping through the low latitude Indonesian archipelago often referred to as Indonesian Through flow (ITF). This mixed fresh water feed the South Equatorial Current in the south-eastern tropical zone. Therefore, the Indian Ocean Equatorial Water is a conglomeration of all the three contrasting water masses originating from Arabian Sea, Bay of Bengal and from the equatorial Pacific through ITF.

Indian Ocean is the warmest Ocean in the world. The core of the world's largest warm pool lies in the equatorial Indian Ocean. The western cross equatorial flow both in ocean and in atmosphere dominate the south-west summer monsoon circulation. The Indo-Pacific warm pool extending right across the eastern equatorial Indian Ocean act as a source region for atmospheric convection often triggers the westerly wind bursts at the western equatorial Pacific modulating the surface ocean condition to the formation of El Niño at the equatorial Pacific. The ensuing dynamics are dominated by the propagation of low frequency planetary waves such as Kelvin and Rossby waves.

At interannual time scales an interesting feature appears to dominate the equatorial Indian Ocean with cold temperature anomalies off Sumatra coast in the eastern equatorial Indian Ocean and warm anomalies at the western equatorial Indian Ocean. This feature is explained as an internal mode of the Indian Ocean and is widely known as Indian Ocean Dipole/zonal mode (IODZM) (Saji et al., 1999; Murtugudde et al., 2000; Webster et al., 1999; Iizuka et al., 2000). Although this internal mode resembles the much bigger Pacific El Niño, its influence on the summer monsoon rainfall over the sub-continent is yet to be understood.

1.2 Equatorial Dynamics and Summer monsoon rainfall.

The relationship between Indian Summer Monsoon Rainfall (ISMR) and the southern Oscillation was noticed and documented by Sir. Gilbert Walker¹ in late 1800s when he visited India for investigating the cause of severe droughts. The teleconnection between these two oceanic domains were further investigated to satisfactorily explain the physical mechanism

¹Sir Gilbert Thomas Walker (1868 –1958) was an English physicist and statistician of the 20th century. He was the director general of Indian meteorological department (IMD). He is known for his contribution in monsoon forecasting and the groundbreaking description of the Southern Oscillation. He developed the time series analysis method that is now called the Yule-Walker equations.

behind the tendency of drier than usual Indian Monsoon preceding peak El Niño conditions (vice versa for La Niña event) by Klein et al. (1999); Krishnamurthy and Kirtman (2003) and Annamalai and Liu (2005). Annamalai et al. (2005a) have documented the characteristics of the inter-relationship in pre and post climate shift era. As El Niño develops in boreal spring, the eastward shift of the Walker circulation over the centre of the Pacific trigger subsidence over South Asia that suppresses convection resulted in the weakening of the ISMR. The ENSO-ISMR relationship was dominantly negative during pre-climatic shift period indicating weaker ISMR preceding a stronger El Niña event (Annamalai and Liu, 2005). The relationship appears to be weakened in the post-climatic shift era probably because of the warming climate (Krishna Kumar et al., 1999). The logic of the teleconnection got more complex by the discovery of Indian Ocean Zonal Mode (IOZM) (Webster et al., 1999; Saji et al., 1999) which appears to co-occur with the ENSO. The IOZM is an independent coupled mode of variability of the Indian Ocean. The IOZM and its relationship with ENSO and their impact on the ISMR has been subject of intense debate for several years (Fisher et al., 2005; Saji and Yamagata, 2003; Annamalai et al., 2003; Baquero-Bernal et al., 2002; Allan et al., 2001; Iizuka et al., 2000).

Recently Indian Ocean Dipole (IOD) has been categorized as one of the major ocean-atmosphere coupled phenomena in the tropical Indo-Pacific and hence is natural to explore its possible influence on the ISMR. Ashok et al. (2001) have projected the IOD as having a significant role as a modulator of ISMR and that it influences the correlation between ENSO and ISMR. Their studies revealed that the anomalous summer monsoon circulation induced by ENSO over the south Asian continent is either complemented or opposed by the IOD induced circulation, depending upon the interaction of phase and amplitude of these two major climate modes in the Indo-Pacific equatorial belt. Recently it has been observed that the correlation between Indian Ocean Dipole Mode Index (IODMI) and ISMR is robust and appears to be increasing. Hence it is worthwhile to examine the possibility of using the IODMI for predicting the monsoon rainfall over India (Ashok et al., 2001).

1.3 The Climate Link beyond the impact on ISMR

The significant correlation was reported by Gadgil et al. (2004) between the interannual variability of ISMR and the equatorial Indian Ocean oscillation (EQUINOO) which is the atmospheric component of IOD represented by the normalized index of the equatorial surface zonal wind anomaly. Although Saji et al. (1999) observed a weak correlation (0.32) between IODMI and ISMR, the strong positive IOD events in the 1958-97 periods have exhibited significant correlation (0.73) with positive rainfall anomalies and few negative IODs with negative rainfall anomalies. It has been observed that an inverse relationship exists between the ENSO-ISMR correlation and the IOD-ISMR correlation (Ashok et al., 2001, 2004). He further explained that the positive IOD events can alter the influence of El Niño on ISMR or act as a modulator of the ISMR variability.

It was generally perceived that the Indian Ocean-climate link beyond the impact of monsoon was not very appreciable, particularly in the vicinity of 10-degree equatorial belt. This understanding changed drastically especially since 1997 after witnessing a systematic sea surface temperature (SST) pattern over the tropical Indian Ocean that followed severe climate change over the western and eastern rim of the tropical basin. During this extraordinary year of 1997, very severe rainfall was recorded in East Africa during October and November and devastating flooding in Somalia, Ethiopia, Kenya, Sudan and Uganda resulted in losing thousands of lives and several thousand people displaced. At the same time severe droughts crippled Indonesia and surrounding countries in the eastern rim of the Indian Ocean. Several of Indonesian Islands witnessed uncontrolled wild fires. Smoke and haze generated created severe health problems in Indonesia and surrounding countries. The unusual phenomenon in the tropical Indian Ocean compounded by the severe El Niño in the Pacific caused these extreme climatic anomalies. The usual equatorial westerly winds suddenly switched to easterlies during late summer and fall of 1997, and eastward current (Wyrтки Jet, 1973) often found to develop during boreal fall never occurred. The quest for understanding these extraordinary features augmented the research activities to understand the peculiar air-sea interaction processes and their probable climate link.

1.4 Organization of the thesis

1.4.1 The thesis manuscript is organized as follows:

Chapter 2 provides an overview of the process occurring in the tropical Indian Ocean relevant to the equatorial processes. A comparison of equatorial circulation and associated processes of Indian Ocean with that of Pacific and Atlantic has been provided. An attempt is also made to understand the present knowledge of the Indian Ocean equatorial dynamics by analysing the impact of climate modes such as ENSO and IOD in the inter-annual scale. The historical perspective of decadal/long-time trends of hydrographical parameters at the surface and the subsurface of the equatorial Indian Ocean are presented

In Chapter 3, details of observational and modelling data sets used in this thesis are explained. Validation of model with the observational data at various time scales is undertaken to understand the accuracy of the data.

Chapter 4 provides a general description of the inter-annual variability of surface and subsurface currents in the equatorial Indian Ocean in association with IOD and ENSO climate modes.

Chapter 5 describes the interannual variability of zonal currents in the equatorial Indian Ocean to understand the respective influence of ENSO and IOD. The contents of this chapter are published in *Ocean Dynamics* (Sachidanandan et al., 2017).

Chapter 6 presents the surface and subsurface temperature variability in inter-annual time scale during pre- and post- climate shift era.

Chapter 7 illustrates the decadal variability and trends in surface and subsurface temperature and salinity at the Equatorial Indian Ocean.

The summary and future works are described in Chapter 8.

Background information and relevance of the present work

2.1 Equatorial regions: A global perspective

For studying the dynamical response of ocean to the forcing on various scales, latitudinal divisions of ocean such as Equatorial, Mid-latitudes and High-latitudes are necessary. This sub division is logical since the planetary vorticity and the meridional gradients in thermal forcing on Earth were changing with the latitude. Among these three regions, equatorial regions were the most significant due to the diversity in the forcing mechanisms. They play crucial role in regulating the world's climate scenario. Due to the disappearance of Coriolis force at the equator, these regions exhibit different dynamics other than mid-latitudes and high latitudes. Equatorial region receives maximum amount of solar radiation which is released to atmosphere in the form of latent heat that subsequently modifies the atmospheric general circulation. High surface water temperature, complexity in different water mass mixing, strong vertical motions and the intense exchange of energy between the ocean and atmosphere are the peculiarities of this region. Due to the reversing Coriolis effect on either side, equator act as a wave guide for the propagation of waves, which have major role in adjusting equatorial ocean to unsteady wind forcing. Dispersion relation derived from linear wave theory classifies waves into Kelvin waves, Rossby waves, Inertia gravity waves and Mixed Rossby Gravity waves (MRG waves/Yanai waves). They are capable of swiftly transferring the perturbation and variability from one region to other along the equator. The influence of these waves on ocean circulation considerably varies with latitude. At the middle and high latitudes change in wind stress propagates in westward direction in the form of Rossby waves and hence the western boundaries of ocean are more prone to the fury of variability's associated wind induced Rossby waves than the eastern boundaries. Whereas in low latitudes these signals propagate in eastward direction as Kelvin waves using equator as wave guide and hence make the eastern boundaries more dynamic than their western counter part. Among these equatorially trapped waves, the Yanai wave has no counterpart at higher latitudes. The necessary condition for propagation of Kelvin waves is that horizontal pressure gradient to

act opposite direction to Coriolis force. In northern hemisphere (NH), a water parcel is moving northwards, with a coastal boundary on its right side, the Coriolis force tends to reflect the parcel to the right but beyond a certain limit this is impossible. The water therefore piles up against the boundary and an offshore horizontal pressure gradient force is generated; this helps the water parcel to move parallel to the coast. As a result, the coast acts as a wave guide to these perturbations known as Kelvin waves. Kelvin waves are of two types: one is coastally trapped Kelvin waves which propagates within a certain distance to the coast, beyond that the amplitude decays and the wave can no longer be identified, this distance limit is known as Rossby radius of deformation; and other one is equatorial Kelvin waves where equator acts as a wave guide for the propagation. Since the Coriolis force is zero at the equator and geostrophic balance in meridional direction, Kelvin waves can only propagate eastward along the equator. A typical surface Kelvin waves have speed of 200-300 cm/s (Gill, 1982). The Rossby radius of deformation of a Kelvin waves is of about 2000 km. Downwelling Kelvin waves propagating along the equator deepens the thermocline thereby deepens the mixed layer that give rise to anomalously warm water at the surface. On the contrary, the upwelling Kelvin waves excited at the eastern part of the equator by the westerlies causes the thermocline to shoal bringing anomalously cold water at the surface.

Yanai waves are anti-symmetric about the equator and at higher frequency they act like Kelvin waves and at lower frequency they behave like short Rossby waves. The energy of Yanai waves propagates eastward since its group velocity is always positive; but their phase can travel either east or west depending on the frequency. Dynamical response of ocean to wind forcing and buoyancy forcing at the ocean interior and at the eastern boundaries results in Rossby waves. At low latitudes these waves can be excited by coastally trapped Kelvin waves at the eastern side of the oceans. They arise from the need for conservation of potential vorticity. Unlike the Kelvin waves, Rossby waves travels slowly, at speeds of a few cm/s. Rossby waves propagate zonally westward along the equator and other latitudes. They transfer energy to western side of the ocean. Thus, the accumulation of the energy in the west leads to an intensification of currents on the western side of all oceans. When these Rossby waves reflect at the western boundary their wavelength shortens while their wavelength lengthens when they hit at the eastern boundary. All together afore mentioned features make the equatorial region distinct from other latitudinal divisions.

Gravitational force by sun and moon, surface forcing by winds, buoyancy fluxes and turbulent diffusion are the main driving mechanisms of currents on various temporal and spatial scales. It was *Ekman*² who first elucidated the response of upper ocean to wind stress and showed how the rotation affects the currents (*Ref many textbooks and internet is the source*). Then it was *Stommel*³ who showed that the westward intensification of ocean currents is the consequence of rotation on a spherical planet, through the change of planetary vorticity with latitude (*Ref many textbooks and internet is the source*). But *Carl Gustav Rossby*⁴ was the one who laid down the foundations by simplifying the rotating sphere to a simple tangent plane with changing planetary vorticity (*Beta plane*) which is used to explain most of the low frequency changes that occur in the oceans and the atmosphere (*Ref many textbooks and internet is the source*).

Ocean currents and atmosphere winds themselves were nature's best contributors in regulating the global climate by redistribution of dynamic and thermodynamic properties within them and they dominate mainly the inter-annual fluctuations in the global weather patterns. So, the equatorial processes are always the centre of attraction for an oceanographer to understand the influence of ocean on the atmosphere. Oceanic circulation is three dimensional and the varying Coriolis force makes it more complex in nature. The current system at the equatorial region is very sensitive to changes in the prevailing winds. In 1961 *Defant*⁵ called the system of equatorial currents as the "Backbone of the ocean circulation". Equatorial regions are vast and remote, also the presence of swift currents and the strong vertical shear makes the instrumentation at the equatorial region very challenging. Because of these intricacies'

²Vagn Walfrid Ekman, (1874 – 1954) was a Swedish physical oceanographer best known for his studies of the dynamics of ocean currents. The oceanographic terms Ekman layer, denoting certain oceanic or atmospheric layers occurring at various interfaces; Ekman spiral, used in connection with vertical oceanic velocity; and Ekman transport, denoting wind-driven currents, derive from his research.(*Source : Encyclopedia Britannica*)

³ Henry "Hank" Melson Stommel (1920 - 1992) was a major contributor to the field of physical oceanography. He is noted for theories about global ocean circulation patterns and behavior of Gulf Stream. He proposed oceanic conveyor belt theory in global circulation system. (*Source: Encyclopedia Britannica*)

⁴ Carl-Gustaf Arvid Rossby (1898 - 1957) was a Swedish-born American meteorologist who first explained the large-scale motions of the atmosphere in terms of fluid mechanics. He identified and characterized both the jet stream and the long waves in the westerlies that were later named Rossby waves. (*Source : Wikipedia*)

⁵ Albert Joseph Maria Defant (1884 - 1974) was an Italian-Austrian meteorologist, oceanographer and climatologist. He published fundamental works on the physics of the atmosphere and ocean and is regarded as one of the founders of physical oceanography.(*Source: Encyclopedia Britannica*)

observations are very much limited in equatorial regions. Even though the emergence of satellite oceanography contributed immensely to study the ocean surface in both space and time, it hardly contributed to the understanding of the subsurface due to very sparse data coverage. During the recent years the progress in ocean modelling helps ones to study in detail the temporal and spatial structure of currents and hydrography in detail.

2.2 Equatorial Regions: An Indian Ocean perspective

International Indian Ocean Expedition (*IIOE*, 1962- 65) was the first massive expedition in which 40 oceanographic research vessels belonging to 13 countries surveyed the Indian Ocean and collected useful data in almost all disciplines in the marine sciences. This was also one of the first co-ordinated efforts to explore the Indian Ocean. Based on this data *Wyrtki*⁶ in 1971 prepared an oceanographic atlas of Indian Ocean, which was the first atlas of that kind. During the year 1995- 96, World Ocean Circulation Experiment (*WOCE*) was conducted, which also served as vital in understanding the Indian Ocean. Soon after the *IIOE*, two observational expeditions were conducted to improve the knowledge on seasonal variability of ocean-atmospheric circulations viz; The Indian Ocean Experiment (*INDEX*) (Luyten and Roemmich, 1982) and the Summer Monsoon Experiment (*MONEX*) (Krishnamurthy, 1985). The Tropical Ocean Global Atmosphere (*TOGA*; 1985- 94) and the World Ocean Circulation Experiment (*WOCE*; 1990- 1998) were the two significant collaborations that paved way for better understanding on air-sea interactions and basin scale circulation patterns related to IO climate. There were also short regional expeditions carried out in the IO such as Bay of Bengal Monsoon EXperiment (*BOBMEX*) (Bhat et al., 2001), the ARabian Sea Monsoon EXperiment (*ARMEX*) (Rao and Sikha, 2005) and the Joint Air-Sea Monsoon Experiment (*JASME*) (Webster et al., 2002). These expeditions significantly contributed to the knowledge on processes controlling the climate variability in those specific areas. Moreover, the Joint Global Flux Study Arabian Sea Experiment (*JGOFAS*) (Smith et al., 2001) provided vital information on understanding the biogeochemical cycles and marine productivity related monsoon forcing.

⁶ Klaus Wyrtki (1925 – 2013) was an American physical oceanographer. Wyrtki is known for his work on understanding and forecasting El Niño. He established a tidal gauge network, gave an explanation for the Pacific oxygen minimum zone under the thermocline and discovered the Indian Ocean current jet that now bears his name, the "Wyrtki Jet". He is also known for his work on thermohaline circulation. (*Source : Wikipedia*)

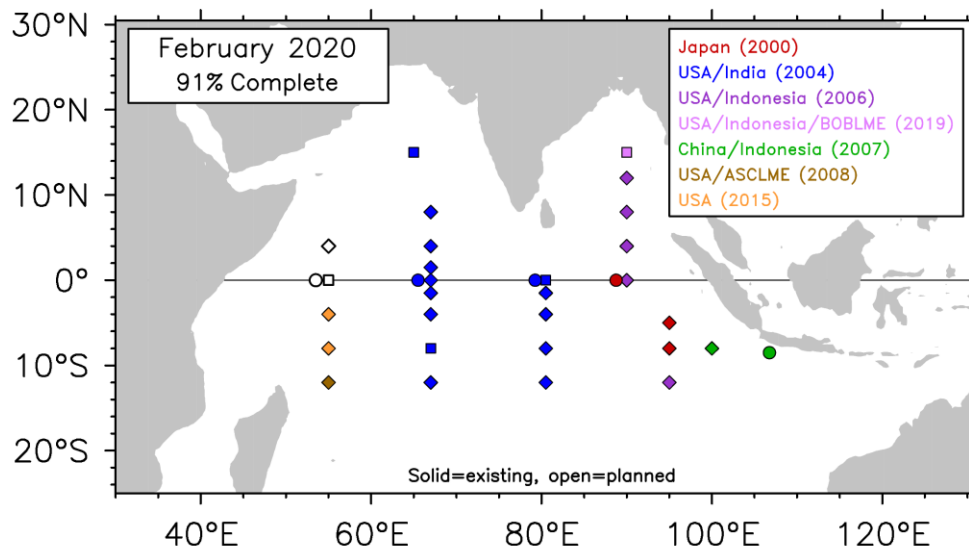


Figure 2.1 RAMA buoys [courtesy: <https://www.pmel.noaa.gov/gtmba/rama-array-map>]

All these observational studies laid firm foundation on oceanic atmospheric variability and the climate change in the IO region. Yet there was an urge for a sustainable and systematic ocean observing system in the IO. In the Pacific, there exists a sustainable observing system related to ENSO monitoring, similar observational platforms were not in place in the IO for a long time that could have given access to studying the broad ranging spectrum of diurnal to multi-decadal variability existing in the IO. Then in the year 2004 a systematic array moored buoys were developed, referred as the Research moored Array for African-Asian-Australian Monsoon Analysis (RAMA; McPhaden et al., 2009) and initiated as a part of INDIan Ocean Observing System (INDOOS) in the IO mainly concentrating on EIO.

RAMA buoys consist of 38 surface and 8 subsurface moorings of which five are Acoustic Doppler Current Profiler (ADCP) to provide long time series of current measurements in upper 300-400 m and the remaining are spread over 35 sites in the tropical IO (Figure 2.1). The main equatorial moorings providing the current measurements along the equator are located at 80.5° E and 90° E. The data delivery and the quality control checks are done by Pacific Marine environment Laboratory (PMEL) of National Oceanic and Atmospheric Administration (NOAA) [<https://www.pmel.noaa.gov/tao/drupal/disdel/>].

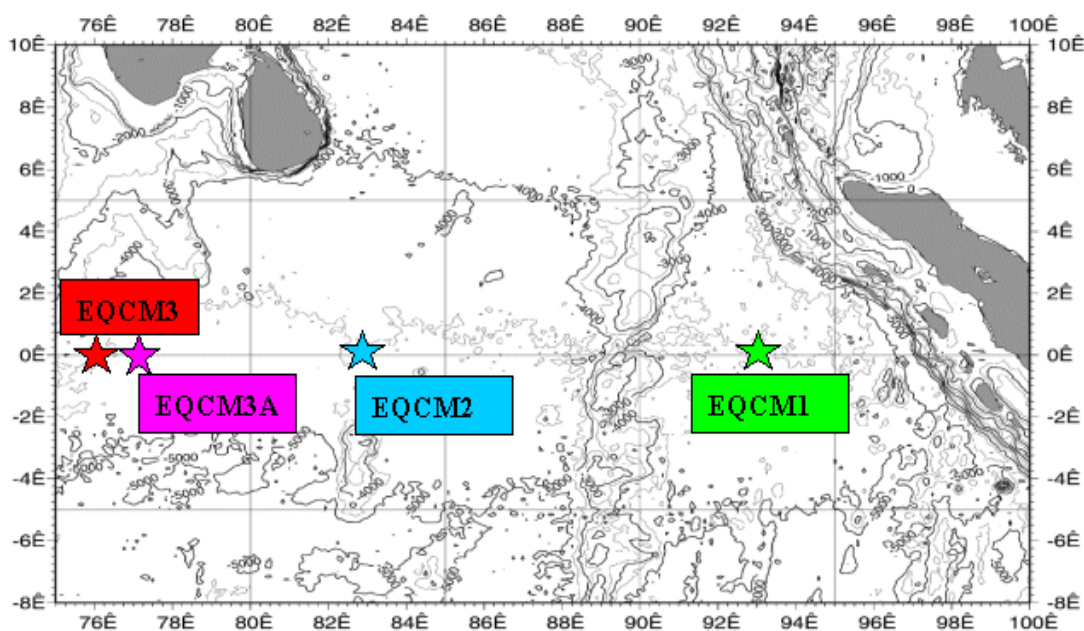


Figure 2.2 NIO moorings [courtesy: <http://www.niobioinformatics.in/oceanclimate31.php>]

As a part of Ocean Observation Studies (OOS) initiated by Department of Ocean Development (DOD) in the year 1997, National Institute of Oceanography (NIO), India had deployed current meter moorings at three different locations in the equatorial Indian Ocean to study the long term variability of dynamics of currents at the equatorial Indian Ocean and the associated climatic variability. At three locations viz: 76° E, 83° E and 93° E (Figure 2.2), Aanderaa Recording Current Meters were deployed in the year 2000. The western mooring station 76° E was subsequently shifted to longitude 77° E in the year 2003. An upward looking Acoustic Doppler Current Profilers (ADCP) was added to the configuration in the year 2004 in all three locations to measure the currents above 400 m at closer intervals. This mooring program was also an initiative of INDOOS (INDian Ocean Observing System). So altogether there exists four fixed mooring locations along the EIO to provide the time series current measurements, viz 76° E, 77° E, 83° E, and 93° E.

The fixed mooring platforms provided long aspired systematic observational records till date, yet for a spatial study they are inadequate. Subsequent to this, a collaborative effort had been made to deploy ARGO (Array of Real time Geostrophic Oceanography) floats to cover the entire global oceans. That is the first attempt to put in place a global real time *in situ* observing

system that provides real-time data for use in climate, weather, oceanographic and fisheries research. To meet the demand for high quality hydrographic data on real/ near- real time, the International Argo project was launched in the year 2000. The ultimate goal of the program is to build a monitoring system of upper- and middle-layer temperature and salinity fields of the world oceans with about 3000 profiling floats. The floats measure the temperature and salinity data with random depth resolution with in 2000m depth over a 5/10- day repetitive cycle. Although drifting floats had been deployed during the 'World Ocean Circulation Experiment' in the 1990s, Argo floats began to be deployed in earnest in the early 2000s. The target number of 3,966 deployed floats was reached till the date (Figure 2.3). The number of floats is replaced as and when the floats are lost or expired. Nominally, some 800 new floats are deployed each year to sustain the system. The floats have nominal 300 km spacing, although the exact separations depend on the randomness of the float drift.

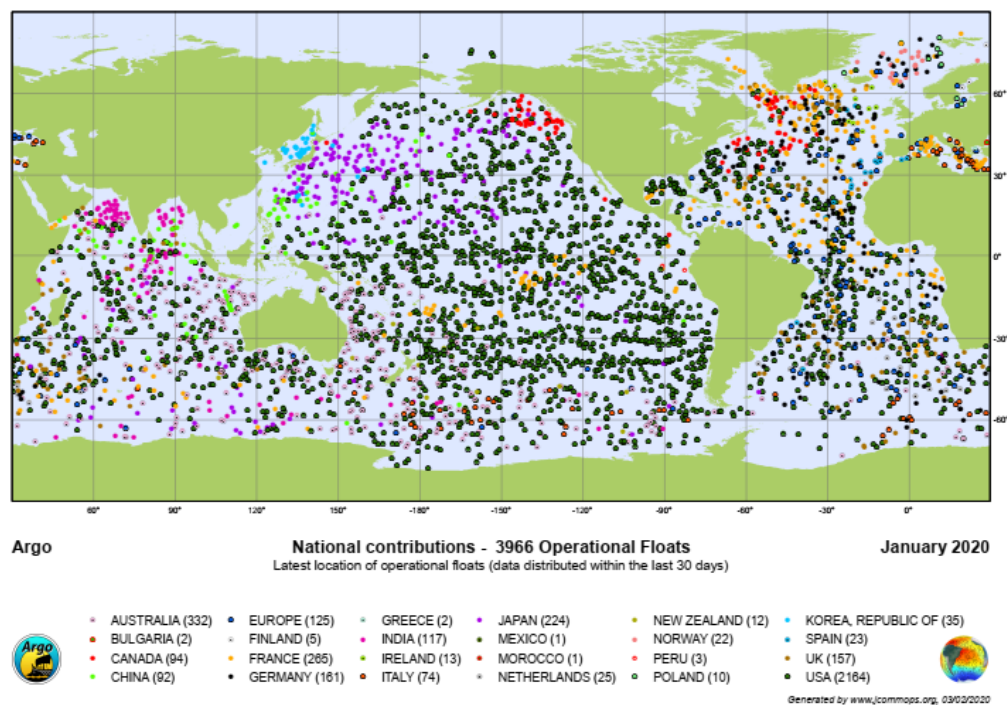


Figure 2.3 Argo floats [courtesy: http://www.argo.ucsd.edu/About_Argo.html]

The Argo program was designed to operate on the same 10-day duty cycle to match the existing satellite measurements of the ocean's sea surface. These satellites, called Topex/Poseidon and Jason-I measure changes in the surface topography of the ocean. With such measurements,

information about temperature, mass redistribution, or surface currents can be inferred. The Argo floats measure subsurface changes in temperature and salinity; hence the float measurements are complementary to the altimetry. The Argo temperature and salinity measurements are yielding valuable information about the large-scale water properties and currents of the ocean, including the variability of these properties over time scales from seasonal to decadal. Argo floats drift at a fixed pressure (usually around 1,000 metres depth) for 10 days. After this period, within the relatively short time of around two hours, the floats move to a profiling pressure (usually 2,000 metres deep) then rise, collecting instantaneous profiles of pressure, temperature, and salinity data on their way to the surface. Once at the surface, the floats remain there almost for under a day, transmitting the data collected via a satellite link back to a ground station and allowing the satellite to determine their surface drift. The floats then sink again and repeat their mission. (Figure 2.4)

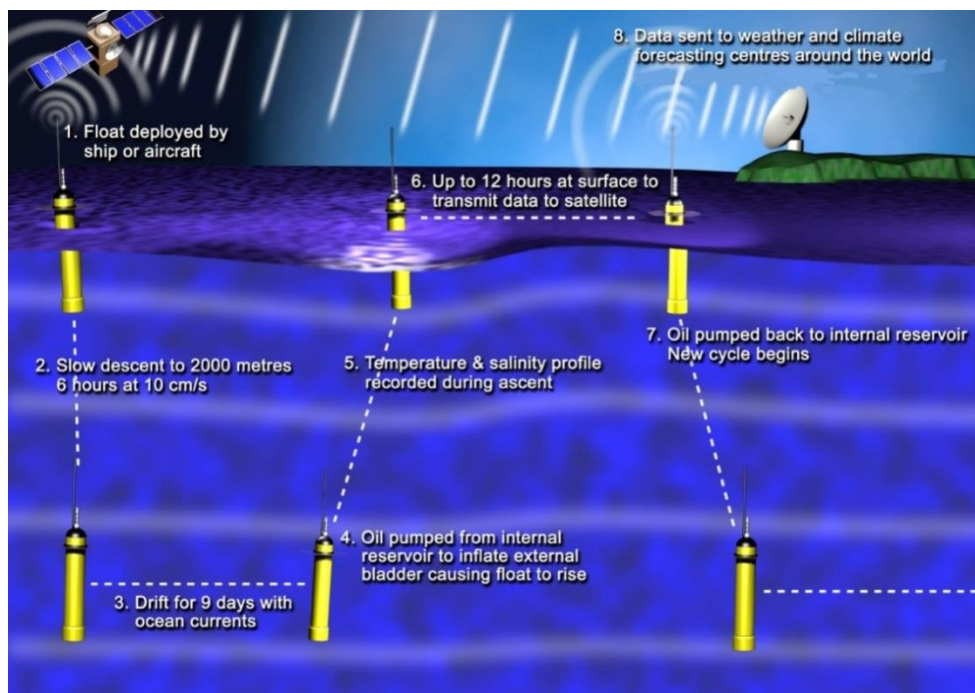


Figure 2.4 Illustration of Argo float deployment, profiling and transmitting via satellite.
[Courtesy: http://www.argo.ucsd.edu/How_Argo_floats.html]

After 50 years of first IIOE expedition, the Second International Indian Ocean Expedition (IIOE-2) is proposed as a major global scientific program which will engage the international scientific community in collaborative oceanographic and atmospheric research from coastal

environments to the deep sea over the period 2015-2020, revealing new information on the Indian Ocean (i.e. its currents, its influence upon the climate, its marine ecosystems) which is fundamental for future sustainable development and expansion of the Indian Ocean's blue economy. The IIOE-2 activities will also include a significant focus on building the capacity of all nations around the Indian Ocean to understand and apply observational data or research outputs for their own socio-economic requirements and decision making. The capacity building programs will therefore be focused on the translation of the science and information outputs for societal benefit and training of relevant individuals from surrounding nations in these areas.

Indian Ocean lies well below 30° N and landlocked its northern part by Asian subcontinent and this boundary sets constraints on basin-wide circulation and heat transport in Indian Ocean, providing a major role in variability of the global climate system. This boundary in the northern part, opening to the Pacific through Indonesia and the broad connection to Southern Ocean all together contribute to highly variable heat gain by Indian Ocean. As a consequence of strong interacting process, the resultant Indian Ocean heat pool is highly variable on time scales ranging from the intra-seasonal to the multi-decadal.

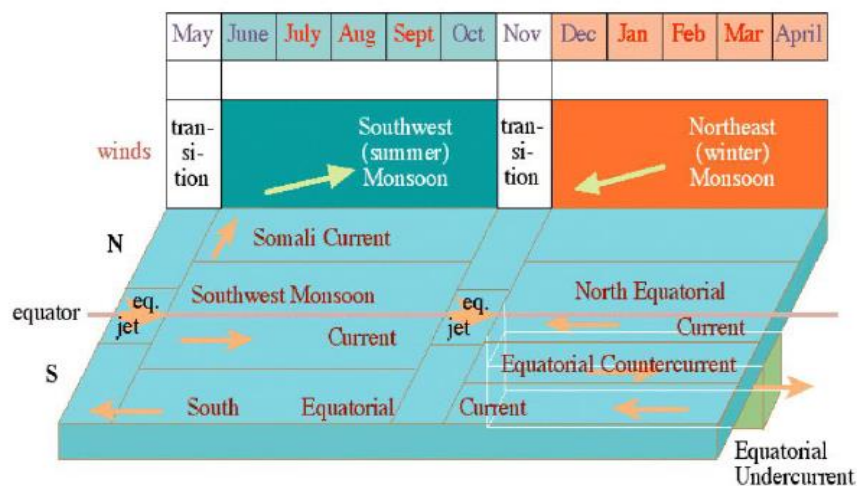


Figure 2.5 Monsoonal system of Indian Ocean (Tomczak and Godfrey [2001]).

Winds over the Indian Ocean are different from other world oceans, where the trade winds always blow in same direction. In Indian Ocean winds blow from south-west during May-September (South-West monsoon/summer monsoon) and north-east during November-February

(North-East monsoon/winter monsoon) and drive a circulation that reverses its direction twice in a year, a complete unseen scenario from other parts of world oceans (Schott and McCreary, 2001; Shankar et al., 2002) (Figure 2.5). Between the two monsoons often referred to as the transition periods, the equatorial Indian Ocean witness moderate westerlies during boreal spring (May) and fall (November) with maxima between 70° E and 90° E.

Another distinct feature is the absence of equatorial upwelling in Indian Ocean, due to the surface divergence caused by southeast trade winds blowing across the equator. Because of monsoon, the spatial distribution of sea surface temperature (SST) in the Indian Ocean is characterized by warm water in the eastern side and cold water on the west which is in contrast to the other major oceans where eastern side is cooler and west is warmer. All characteristic properties of Indian Ocean show an east-west asymmetry. Fresh water input is high on eastern side than west causing the eastern side to have a lower salinity than the west. Major upwelling systems are on the western side making those regions more biologically productive than its eastern counterpart. Consequence to this east-west contrast, the thermocline shoals in the west and deepens at the east. This asymmetry in SST therefore influences the overlaying atmosphere by promoting strong convection close to the eastern boundary and drought like situation prevails over the western boundary.

In the equatorial Indian Ocean(EIO) during the winter monsoon months (December-February), the westward flowing North Equatorial Current (NEC) sets in between 8° N and 2° S (Figure 2.6) with approximate velocity and volume transport of 0.3 m/s and 5×10^6 m³/s respectively (Figure 2.6). They are also called north-east monsoon Current (NMC) since they are found during North-East monsoon period. An equatorial counter current (ECC) flows eastward between 2° S and 8° S with a velocity of about 0.5 to 0.8 m/s. South of this is the westward flowing South Equatorial Current (SEC) with speed 0.3 to 0.5 m/s. The volume of water transported by this current is estimated to be maximum during July-August and minimum during January- February. The South Equatorial Current is a western boundary current, which does not show any seasonal variability. During south-west monsoon period the NEC reverses and combines with ECC to form South-West Monsoon Current (SMC) or summer monsoon current and spread meridionally from 15° N to 7° S (Figure 2.6).

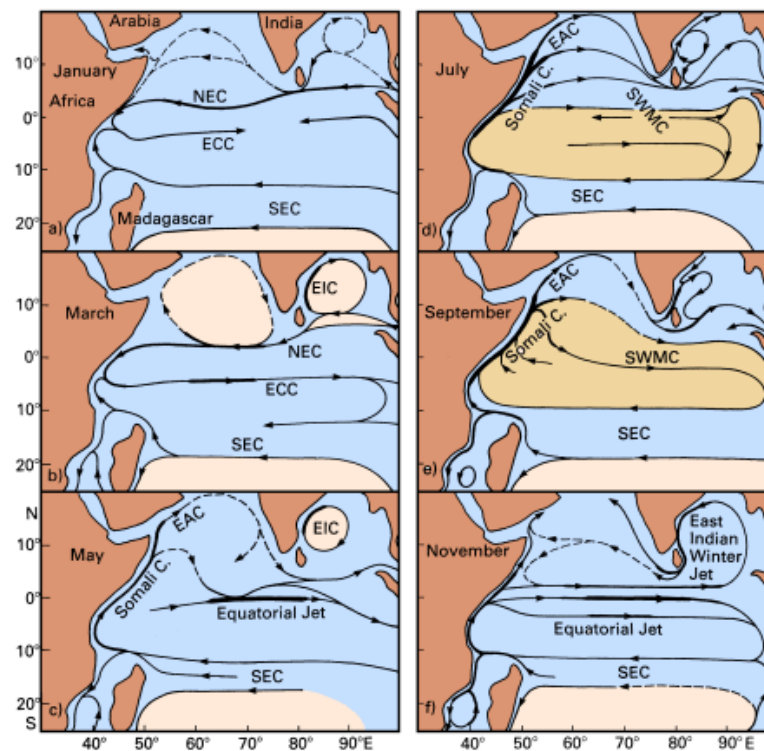


Figure 2.6 Surface circulation of Indian Ocean (Tomczak and Godfrey, [2001]).

During winter monsoon and spring inter-monsoon season at the EIO, the easterly trade winds drives both NEC and SEC westward causing mass convergence at the western boundary and the accumulation is strong enough to build up an eastward pressure gradient. The pressure gradient force is balanced by the easterly wind stress at the surface. But below the surface the wind stress can no longer balance the pressure gradient. As a result, a narrow ribbon of eastward flowing current develops at the thermocline which is often referred to as Equatorial Undercurrent (EUC). The velocity core of this eastward flow roughly follows the 20 °C isotherm running through the mid-thermocline region.

Strong westerlies during transition period (spring inter-monsoon period from April-May and fall inter-monsoon period from October-November) drive a narrow and swift eastward equatorial jet often called Wyrtki Jet with speed exceeding 1m/s (Wyrtki, 1973; Obrien and Hurlburt, 1974). They are best developed in the upper 100m between 60°-90° E within 2° N and S of the equator (Reppin et al., 1999). However, the jet weakens as it moves away from the

equator (Rao et al., 1989; Visbeck and Schott, 1992). It disappears in western part of the equator where the meridional component of current over shoots the zonal component. Joseph et al. (2012) have observed a weaker spring jet for six years from 2006 since the supporting wind stress was too weak and at times, they even reversed its direction to westward as seen in 2008. Observations showed that Wyrki jet influences the path of south-west monsoon current in the eastern equatorial Indian Ocean (Vinayachandran et al., 1999).

The Kelvin and Rossby waves associated with the eastward jet has the potential to modify the Indonesian Through Flow (ITF) causing serious alterations in the basin scale heat budget calculations (Yamagata et al., 1996). The monsoon wind reversal along the equatorial region in the transition period causes depressions in thermocline along with the rise in ocean surface; this propagates eastward as downwelling Kelvin waves (McCreary et al., 1993). When the equatorial Kelvin wave hits the eastern boundary, it splits into two coastal Kelvin waves propagating pole ward along the coast on either side of the equator. The northward Kelvin wave travels along the periphery of Bay of Bengal and Andaman Sea (Potemra et al., 1991) and radiate westward moving Rossby waves with same frequency. These Rossby waves propagate westward into the interior Bay of Bengal and modify the Bay of Bengal circulation (McCreary et al., 1996). Model studies by (Potemra et al., 1991; Yu et al., 1991; McCreary et al., 1993) showed that coastally trapped Kelvin waves along the Bay of Bengal boundary travels to the entire coast of Sri Lanka and reach the west coast of India. These waves further move poleward along the west coast of India and a part of it radiate into the Arabian Sea as westward propagating Rossby waves (McCreary et al., 1993).

Observational studies showed pronounced warming at the surface of the tropical Indian Ocean over the past century (Alory et al., 2007; Ihara et al., 2008; Alory and Meyers, 2009; Roxy et al., 2015). The tropical Indian Ocean contains one of the major and largest warm pool systems ($SST > 28\text{ }^{\circ}\text{C}$) among the world oceans. The eastern equatorial Indian Ocean has an SST that is warmer than $27.5\text{ }^{\circ}\text{C}$, the threshold required for intense convection in the tropics (Gadgil et al., 1984), and hence forms a part of the Indo-Pacific warm pool. Studies of Du and Xi (2008) and Hoerling et al. (2004) provide evidence of widening the warm pool region of the equatorial Indian Ocean as a result of the basin scale warming. The monsoon Hadley cell appears to weaken

as the warming spread to the central equatorial Indian Ocean. In such a scenario the central equatorial warming plays an active role in modulating the climate on regional (Chowdary et al., 2015) and global scales (Schott et al., 2009).

The present study aims at investigating inter-annual variability of currents and waves in the equatorial Indian Ocean along with the long-term trends in hydrography using model/reanalysis data.

2.3 Seasonal Indian Ocean climate

Indian Ocean climate variability spans in different time scales from diurnal to inter-annual and is strongly connected to seasonal cycle (Schott. et al., 2009). The IO is characterised by a strong seasonal cycle associated with one of the largest monsoon circulations on earth. The IO climate is divided into four seasons such as summer monsoon, winter monsoon and the two inter-monsoons due to the energetic seasonally reversing monsoon winds. As the influence of monsoon is prominent north of 10° S, a natural monsoon regime is evolved and demarcated by the latitude 10° S. The seasonal cycle of other tropical basins (Pacific and Atlantic) resembles the southern IO (south of 10° S) with south-east trades and other related current and their strength varies with the progress of the season. The parameters like SST and net heat flux over the northern tropical basin undergoes a semi-annual cycle with two seasons of warming during inter-monsoon and two seasons of cooling during summer and winter monsoon. The northern IO also exhibits energetic seasonally reversing surface currents as a direct response to the seasonal wind forcing. The major atmospheric and oceanographic features of the northern tropical IO in response to each of these four seasons are presented below.

As the summer monsoon advances, the Asian continent warms up faster than southern IO resulting in the formation of a low-pressure system over the Asian subcontinent and high-pressure system south of it by virtue of the strong land-sea temperature gradient in the northern hemisphere. The meridional pressure gradient drives a low-level cross-equatorial jet (Findlater, 1969) over the Arabian Sea (Figure 2.7a) causing moisture flux towards the Asian landmass that eventually initiate precipitation that appears to be strengthening along the Western Ghats due to

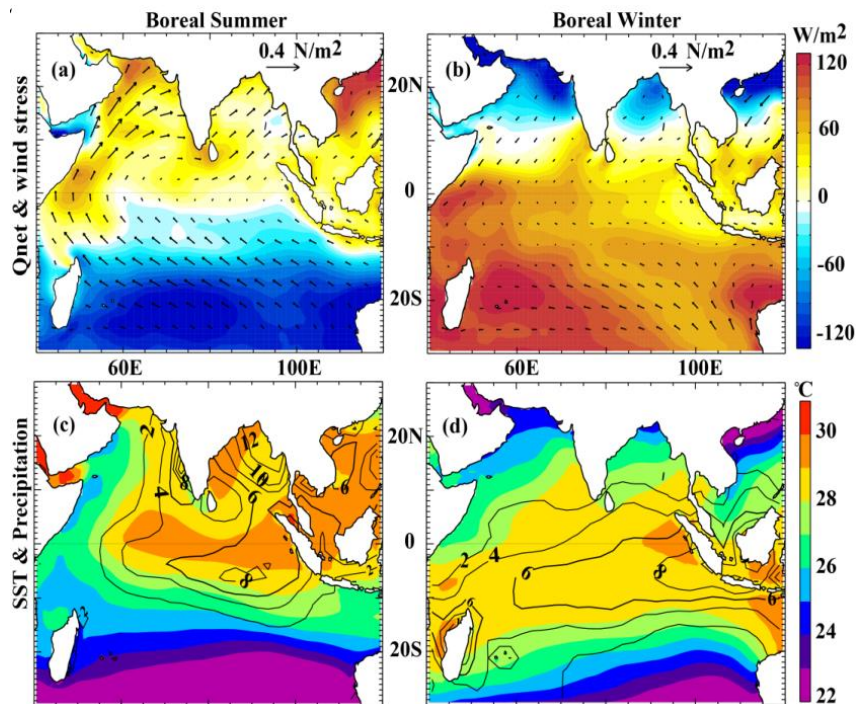


Figure 2.7 Boreal (left panel) summer and (right panel) winter (top panel) net heat flux (shade) and wind stress (vectors) and (bottom panel) SST (shade) and precipitation (contours) fields in the IO (Keerthi, 2017)

the orographic uplift (Figure 2.7c). The SST changes are mainly driven by air-sea fluxes (Figure 2.7a&c). The low-level jet also triggers a strong northward current along the coast of Somalia. The strong westerly wind also derives the summer monsoon current. During summer monsoon winds blow from SW in the Northern Hemisphere (NH) and the SE trades continues to blow at the Southern Hemisphere (SH) especially in western equatorial Indian Ocean, with the preponderant meridional component toward north.

During boreal (northern) winter (December-February), the north-easterlies drive the climate of the northern IO in response to the annual march of the sun shifting the Inter tropical convergence zone (ITCZ) to the south of the equator (Figure 2.7d). The Asian landmass, colder than the surrounding seas, generate high pressure system that drives cold, dry north easterly continental winds away from the Asian continent (Figure 2.7b). Therefore, the season is often known as dry season. During winter when the equatorial Indian Ocean resembles the other equatorial regions of the world ocean, the NEC flows westward from north of equator and

extends up to 2° S, followed by ECC between 2° S and 8° S flowing towards east. South of ECC, the SEC flows towards west.

The fall inter-monsoon (October- November) and spring inter-monsoon (April- May) are the transition phases between the two monsoons. During these periods, both monsoon circulation and related surface wind forcing weakens. The associated reduced latent heat loss and increased insolation results in net heat gain and strong vertical stratification that causes the SST to rise all over the northern basin. The stratification is compounded by the fresh water influx and enhanced precipitation along with river runoff in the BoB. The winds change direction along the equator associated with the movement of Walker circulation causing stronger equatorial westerlies. The strong imbalance associated with the westerly wind stress and the zonal pressure gradient generates a strong eastward jet in the ocean often referred as Wyrтки jet (Wyrтки, 1973). The monthly surface-current climatology of the tropical IO from satellite tracked drifting buoy data (Molinari et al., 1990) during boreal winter and spring showed two counter-rotating gyres which break down during boreal summer. During these periods, the SEC move closer to the equator and the NEC is replaced by the Southwest Monsoon Current (SMC). The large-scale gyre reappears during boreal autumn with the reappearance of the equatorial jets. Observations from the ship drift data and drifting buoy analysis (Molinari et al., 1990; Qiu et al., 2009) and the model simulations (Yuan and Han, 2006) showed that equatorial jet tends to propagate towards west due to the westward migration of semi-annual winds and influence of equatorial Rossby waves coined by Qiu et al. (2009).

Using satellite altimetry data Antony et al. (2002) showed the symmetric nature of fall jet at the equator and the restriction of spring jet to south of the equator. The speed, width and maximum duration of the jet during both inter-monsoon periods were found to be about 70-80 cm/s, 400 km and 3 months respectively. The vertical advection associated with EJ causes the thermocline to sink and form a subsurface high salinity core and it is well balanced during the pre-monsoon transition period. It appears to be decreasing from 84° E to 90° E and seen that irrespective of the season after attaining peak at 84° E (Muraleedharan and Prasanna Kumar, 1992; Muraleedharan, 1993). Wyrтки jet transport upper warm water towards the east, near the boundary causing the thermocline in the east to become deeper than in the west. Thermocline

slope becomes greater during the spring and fall and the volume of warm water and the heat content of Indian Ocean is larger on the eastern side than the west. The warm pool in the equatorial Indian Ocean deepens to about 80m during the May-June and November-December happens due to EJ (Vinayachandran et al., 1991).

Since Indian Ocean is dominated by the seasonally reversing monsoons, the mean winds are westerly almost in a year along the equator. Easterlies prevail only during north-east monsoon period (December-April) when the equatorial Indian Ocean behaves like Pacific and Atlantic. An eastward pressure gradient develops during this time in the thermocline in response to the surface easterlies. Therefore, EUC can be seen only during boreal winter and spring seasons at depths of 90-170 m. A subsurface salinity maximum is noticed along with EUC during this time. The term 'transient' is often used to describe the EUC in the Indian Ocean as it seldom seen as a permanent feature as in the Pacific and Atlantic. The EUC in the Indian Ocean often shows its presence when the winds are stronger and favourable even though for a short duration. Observations of wind and currents at Gan Island ($0^{\circ} 5^{\circ} S, 73^{\circ} E$) gives clear evidence on the occurrence of an undercurrent during spring inter monsoon period, driven by an eastward pressure gradient (Cane, 1980). Bubnov (1994) observed the presence of an eastward flowing EUC during February-May and from June-August in central and western equatorial Indian Ocean. Leetmaa et al. (1980) detected EUCs at $55^{\circ} E$ from the cross-equatorial profiles during spring season of two consecutive years and shifted southward in the following months (May and June) to merge with an eastward sub surface counter current near $3^{\circ} S$. The EUC seems to be stronger and long-lived flow in the western Indian Ocean than their eastern and central counterpart. The mass transport of the EUC was estimated to be $17 Sv^7$ in March- April 1994 and more than $10 Sv$ in August 1994 with speed of $40 m/s$ at depth of about $150 m$ (Reppin et al., 1999). Iskander et al. (2009) found that during winter the generation of an eastward pressure gradient, which drives an eastward flow in thermocline is caused primarily by upwelling Kelvin waves excited by prevailing easterly winds.

⁷ A non SI unit of volume transport in oceanography and meteorology. Named after in honor of pioneering oceanographer Harald Sverdrup. $1Sv$ is equal to one million cubic meters per second.(Source: Wikipedia)

2.4 Equatorial Indian Ocean: Inter-annual variability

2.4.1 An overview

Besides seasonal changes, the equatorial wind forcing in the Indian Ocean exhibits intense inter-annual variabilities. El Niño-Southern Oscillation (ENSO) and the Indian Ocean Dipole are the main climatic modes affecting the interannual variability of wind and precipitation over the tropical IO. The Indian Ocean Dipole (IOD) (Saji et al., 1999; Webster et al., 1999; Vinayachandran et al., 1999) and ENSO (Murtugudde et al., 2000) contribute directly to wind forcing (Saji and Yamagata, 2003; Gadgil et al., 2004; Yamagata et al., 2004) that drives anomalies in EJs in inter-annual time scales. The inter-annual variability of Indian Ocean SST is due mainly to the ENSO, through an atmospheric bridge called the Walker circulation. About four months after the basin wide SST anomalies in the equatorial Pacific, the whole of the Indian Ocean is observed with the same anomalies. This basin wide warming (cooling) of the Indian Ocean during the warm (cool) phase of ENSO is due to surface heat fluxes. Correlations between SSTA in eastern equatorial Indian Ocean and ENSO indices suggest that IOD events are forced by ENSO (Allan et al., 2001; Xie et al., 2002; Hastenrath et al., 2002; Annamalai et al., 2003). However, there are instances of IOD events occurring independently. Moreover, the developing and maturing phases of the IOD event happen during the boreal summer and fall, while those of ENSO occur during the boreal winter and spring. It is, therefore, clear that the intrinsic ocean-atmosphere coupling in the Tropical Indian Ocean is capable of leading an IOD event.

2.4.2 Inter annual climate modes

Schematic of El Niño phase, normal phase and La Niña phase in the tropical Pacific is displayed in Figure 2.8. The easterly trade winds along the equatorial Pacific, under normal condition; generate an east-west slope in the thermocline shoaling from west to east cooling the eastern Pacific by inducing an equatorial upwelling through the uplift of thermocline. The westward current forced by the easterly trade winds accumulates warm waters in the western Pacific triggering deep atmospheric convection eventually forming the limb of the walker circulation. Similar air sea interaction processes are necessary for the development of ENSO through the Bjerknes feedback process (Bjerknes, 1966) where the positive feedback between the

intensity of the surface winds and the SST come into play. In the positive feedback loop, a positive SST anomaly in the central Pacific promotes deep atmospheric convection and an associated westerly wind anomaly (Gill, 1980) which in turn drives an anomalous eastward flow in the central Pacific that pushes the warm pool eastward thereby reinforcing the initial SST warming. The process eventually leads to the development of an El Niño event often peaking towards the end of the calendar year. However, the intensification of the normal condition leads to the formation of La Niña. During this time enhanced southeast trade winds shift the warm pool westward far away from its normal position with increased east-west tilt of the equatorial thermocline. ENSO is usually described by the Niño 3 and Niño 3.4 indices, which are calculated as the SST anomalies averaged over the (150° W-90° W, 5° N-5° S) and (170° W-120° W, 5° N-5° S) regions respectively.

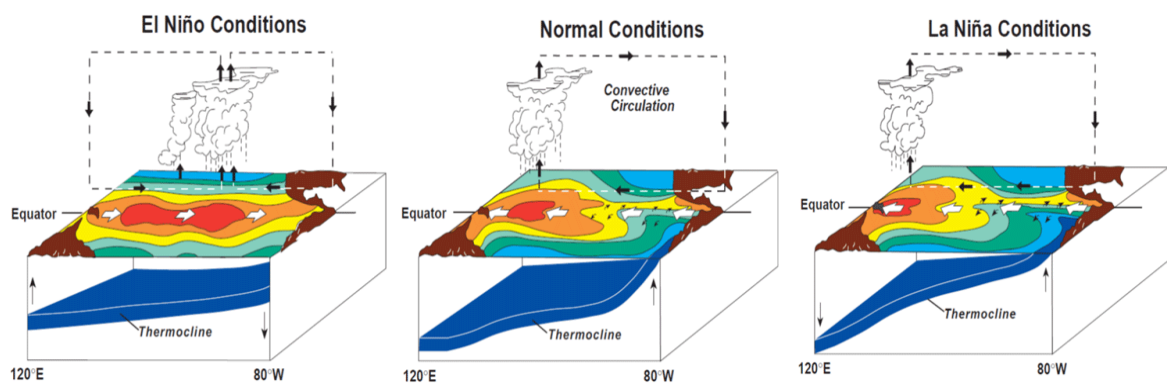


Figure 2.8 A model of surface temperatures, winds, areas of rising air, and the thermocline (blue surface) in the tropical Pacific during El Niño, normal, and La Niña conditions [Source: NOAA/PMEL/TAO Project Office, Dr. Michael J. McPhaden, Director; Image courtesy: <http://www.reefresilience.org/coral-reefs/stressors/climate-and-ocean-change/el-nino-southern-oscillation/>]

The impact of the ENSO is clearly felt on the IO climate through atmospheric teleconnections (Trenberth et al., 1998). The anomalous subsidence over the IO induced through the eastward shift of the Walker circulation during an El Niño event. During this period, the weakening of surface wind speed and the reduction of upward latent heat flux resulted in low cloudiness permitting more solar radiation to reach the surface of IO (Klein et al., [1999]; Ohba and Ueda, 2006; Lau and Nath, 2000). This leads to overall warming of the IO often initiating in the summer month of El Niño year and even persist in spring after the demise of El Niño through local air-sea interactions often termed as the so-called “capacitor” effect of the IO (Xie et al.,

2009). The warming (cooling) of the IO following El Niño (La Niña) in the Pacific is known as the Indian Ocean Basin Mode (Ohba and Ueda, 2006).

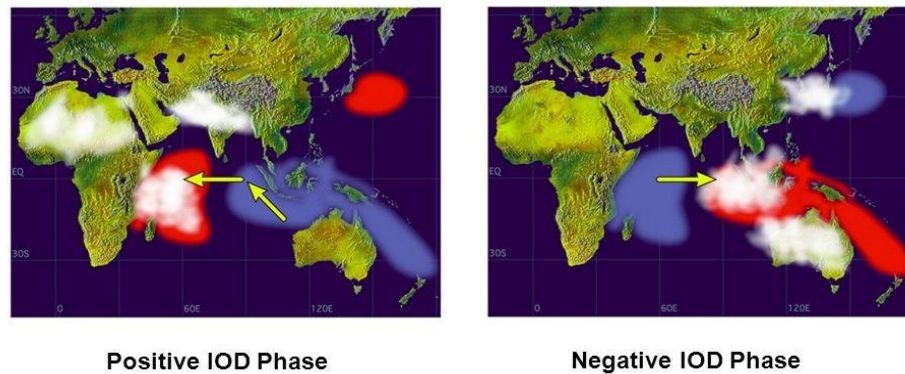


Figure 2.9 Indian Ocean Dipole modes

[Courtesy: *Jamstec*; http://www.jamstec.go.jp/aplinfo/sintexf/e/iod/about_iod.html]

Like ENSO in Pacific, the IOD is a dominant coupled mode in the tropical IO. The positive phase of IOD is often associated with negative (cold) SST anomalies off the west coasts of Java and Sumatra and positive (warm) SST anomalies in the western equatorial IO driven by the anomalous surface easterlies in the equatorial IO (Figure 2.9). This enhanced east-west gradient of SST is maintained through a positive feedback loop (Bjerknes feedback) that involves SST and surface winds (Webster et al., 1999; Saji et al., 1999) similar to the feedback mechanism critical to the ENSO development in Pacific. The warm SST anomalies promote convection in the western IO and cold SST anomalies inhibit convection in the east. The anomalous easterlies cause shoaling of thermocline in the eastern part of the basin and deepens in the western IO, exhibiting a zonal dipole-structure in sea level, SST and subsurface temperature (Rao et al., 2002; Murtugudde and Annamalai, 2004). A negative IOD phase is generally characterized by anomalies of opposite polarities. The IOD events, like ENSO, are strongly locked to the annual cycle. Its signature surfaces in May- June, peaking in fall and disappearing by the end of the year, with a total lifespan of 6 months (Saji et al., 1999). There are instances of co- occurring of both positive IOD in IO and ENSO in Pacific and at times IOD occur independently (Saji et al., 1999; Fischer et al., 2005; Annamalai et al., 2003; Yamagata et al., 2004; Song et al., 2007; Meyers et al., 2007). The positive and negative phases of IODs are usually defined using the Dipole Mode

Index (DMI), which is the difference between the SST anomalies along the western tropical IO (50° E - 70° E, 10° S - 10° N) and south- eastern tropical IO (90° E - 100° E, 10° S - 0° N).

The Indian Ocean Basin (IOB) wide warming or cooling is the leading mode of interannual SST variability in the IO (Klein et al., 1999; Alexander et al., 2002; Chowdary and Gnanaseelan, 2007; Du et al., 2009; Chowdary et al., 2015), which is induced by El Niño /La Niña in the boreal winter (Klein et al., 1999; Alexander et al., 2002; Chowdary et al., 2015). This IOB mode is triggered by Rossby wave induced Ekman convergence/divergence and variations in heat flux induced by El Niño related subsidence (e.g. Chowdary and Gnanaseelan, 2007; Du et al., 2009; Chowdary et al., 2015).

An anomalous anti-cyclonic curl that generates downwelling Rossby waves in south tropical IO during the developing phase of IOD is caused by the strong easterlies along the equator and the south- easterlies along the coast off Sumatra and Java (Rao and Behera, 2005; Yu et al., 2005). These westward propagating Rossby waves deepen the thermocline and hence warm the western equatorial waters (Murtugudde et al., 2000; Vinayachandran et al., 2002). While ENSO events as well as the IOD events that are often triggered by them are observed to frequently co-occur, they do also occur independently, resulting in an intrinsic mode of variability in the IO (e.g. Annamalai et al., 2003; Luo et al., 2010; Izumo et al., 2010, 2013).

2.4.3 Equatorial Indian Ocean response

The inter-annual variability of climate over the equatorial Indian Ocean is mainly dominated by Wyrтки jets (EJ) variability. Qiu et al. 2009, using surface drifting buoys and satellite altimeter data, found that the EJ emerge initially in the central equatorial Indian Ocean (75°– 80° E) in response to the westerly wind, and then propagate westward along with the westward migrating semi-annual wind pattern along the equator. The fall jet appears to be stronger (~0.7 m/s) than the spring jet (~0.5 m/s). The inter-annual wind stress fluctuations associated with IOD/ENSO can directly contribute to inter-annual variations in the equatorial current system of this basin. Several studies reported large inter-annual variations in the intensity of the Wyrтки jets (Reppin et al., 1999; Vinayachandran et al., 1999, 2007; Murtugudde et al., 2000; Grodsky et al., 2001; Han et al., 2004; Nagura and McPhaden, 2010a; Gnanaseelan et al.,

2012; Joseph et al., 2012) and the seasonal EUCs (Reppin et al., 1999; Iskandar et al., 2009; Swapna and Krishnan, 2008; Nyadjro and McPhaden, 2014) in response to inter-annual equatorial wind fluctuations. Easterly wind anomalies have been shown to reduce the intensity of the fall Wyrcki jet (Han et al., 2004; Thompson et al., 2006; Nagura and McPhaden, 2010a; Joseph et al., 2012). Inter-annual zonal current anomalies at the equator tend to lead the zonal wind stress anomalies by one month, as a response to the reflected Rossby waves radiating from the eastern boundary (Nagura and McPhaden, 2010a). Easterly wind anomalies also intensify the EUC in late summer/early fall, through an increase of the eastward pressure force in the thermocline (Han et al., 2004; Swapna and Krishnan, 2008; Nyadjro and McPhaden, 2014), and related off-equatorial southern hemisphere zonal winds that force equator-ward geostrophic thermocline flows (Krishnan and Swapna, 2009; Zhang et al., 2014), although recent studies generally focused on the equatorial current response to IOD forcing (Thompson et al., 2006; Swapna and Krishnan, 2008; Nagura and McPhaden, 2010a; Joseph et al., 2012; Nyadjro and McPhaden, 2014; Zhang et al., 2014). EUC can develop in IOD years and provide cool subsurface waters to the upwelling regions in the eastern Indian Ocean (Reppin et al., 1999), and ADCP observations confirmed this result. An eastward flowing EUC was present during 2006 along with a positive IOD at 83° E during mid-June and July 2006 in the depth range of 100-125 m with a speed of 20-50 m/s (Lakshmi et al., 2007). Studies on the variability of inter annual zonal transport associated with 1994 and 2006 IOD events, showed an anomalous westward flow along the equator in both IOD years and thus the development of cold SST anomalies in the eastern basin. An eastward EUC cantered around 100 m depth in February-April in 2005 and 2006 (Nagura et al., 2008) was also reported. An observed inter- annual variability of Indian Ocean Through Flow (ITF), that connects the Pacific and eastern Indian Ocean, proved that the pressure gradient in the upper layers of these two basins enhance the westward flowing ITF during La Niña and reduce during El Niño events. The anomalous conditions of the 2006 IOD year resulted in a cold SST, particularly off Sumatra, that was anomalously colder than the western Indian Ocean. The sea level was lower than normal in the east and elevated in the west, and the thermocline was shallower than normal in the east (Vinayachandran et al., 2007). He has also noticed the absence of fall Wyrcki jet during this year. Alexander et al., 2004 suggested that ENSO contributes to IOD by forming anomalous cold water on the eastern side of the TIO. It is difficult till date to disentangle the respective impacts of IOD variations and ENSO on the IO

equatorial current system because inter-annual variations of the equatorial winds are related to these two climate modes which often co-occur. Such an attempt has been recently undertaken by Gnanaseelan et al. (2012) with respect to the surface Wyrki jet in the fall. Their analysis suggests that both ENSO and IOD have a considerable impact on the IO surface currents, with IOD affecting currents throughout the equatorial IO and ENSO affecting mainly the eastern part of the basin.

2.4.4 The tropical Indian Ocean

Compared to the world oceans, the IO is smaller and younger with unique geographical positioning. The IO is surrounded by Eurasian landmass at the north, African land mass to the west and Australia and the maritime continents to the east. The average depth is about 3800 m. The bottom topography is characterised by two ridge systems (central Indian ridge and Ninety East ridge) that divides the IO into three equal parts. Due to the land locking, the northern IO extends only few degrees north of Tropic of Cancer with no temperate and polar regions inhibiting northward export of heat (Schott et al., 2009) a unique geography that has significant impact on ocean circulation and climate. The differential heating between Asian land mass and ocean south of it produce an unusual air-sea interaction patterns that results in strong seasonally reversing monsoon system in the northern IO. Lack of steady equatorial easterlies, in contrast to Pacific and Atlantic, prevent the formation of a semi-permanent upwelling system in the eastern part of this basin. Instead, the upwelling occurs along the west coast of Arabian Sea and at the tip of peninsular India (Schott et al., 2009). The shift in climatological upwelling regime from the equator to the north, the eastern IO become very warm and eventually become part of the Indo-Pacific warm pool with very active air-sea interactions over a wide range of time scales.

2.4.5 The Climate variability

The Indian Ocean experiences climate variations from intra-seasonal to seasonal, inter-annual and decadal/multi-decadal time scales. These includes Madden-Julian Oscillation (MJO) (Madden and Julien, 1971, 1972), active/break monsoon and Quasi Biennial Oscillation (QBO) in the intra-seasonal time scales, monsoon in the seasonal time scale, ENSO and IOD in the inter-annual time scale and Global warming, sea level changes, anthropogenic warming, inter-decadal pacific oscillation in the decadal to multi-decadal time scales (Figure 2.10). These climate

fluctuations strongly influence the Indian Ocean rim countries and also have remote effects. A detailed description of the climate variability at different timescales in the tropical IO is presented below.

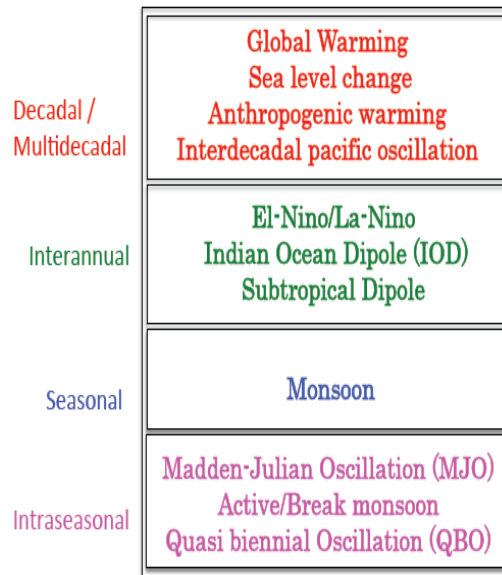


Figure 2.10 Time scales of various climate modes in IO

2.4.6 Air-Sea Interface of the Tropical belt

2.4.6.1 Wind Forcing

In the southern hemisphere south of 10° S, the southeast trades are relatively steady (Figure 2.11). But north of 10° S, the northern boundary of the trade wind shifts northward (southward) during boreal summer and fall (winter and spring) and reversing direction with the monsoons (Figure 2.11a&c). Absence of sustained easterly winds along the equatorial Indian Ocean is another striking difference from other tropical oceans. In contrast, the near equatorial winds have an easterly component during the late winter and early spring (Figure 2.11a). The inter-monsoon seasons exhibit semi-annual westerly component as shown in Figure 2.11b&d with a weak westerly annual mean.

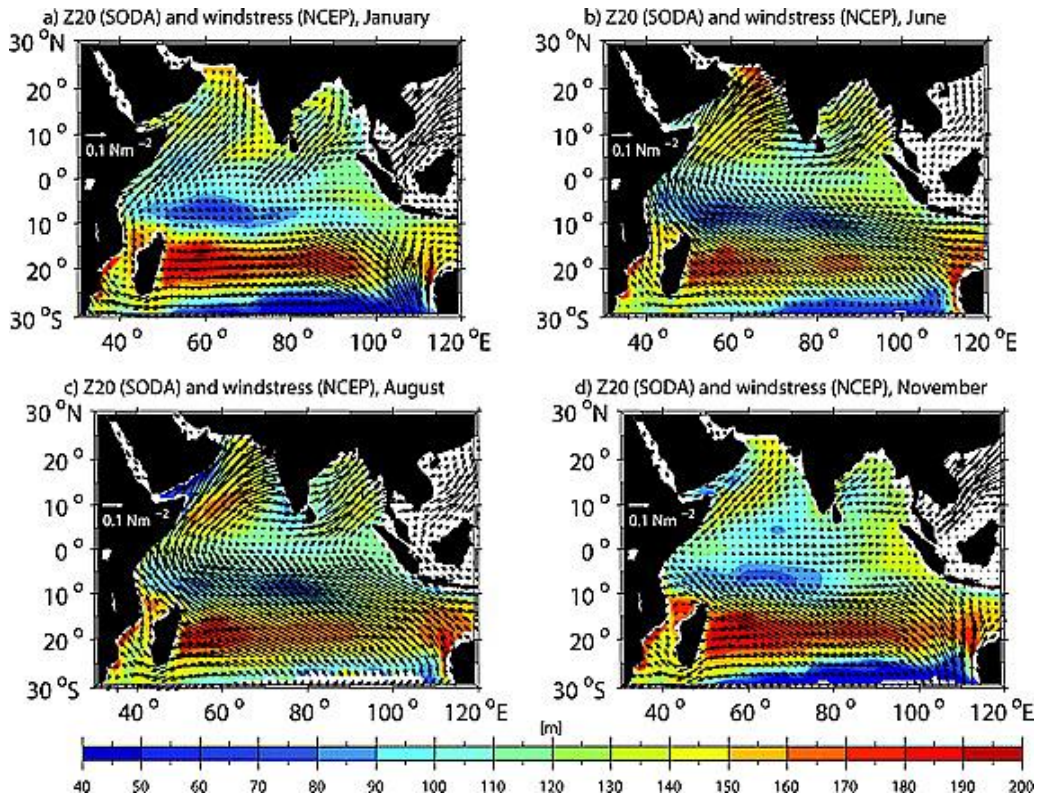


Figure 2.11 Monsoon wind stress fields from the 1990–1998 National Centers for Environmental Prediction (NCEP) (Kalnay et al., 1996) climatology (vectors) and depths of 20° C isotherm (D20) from Simple Ocean Data Assimilation (SODA) (mean for 1992–2001, colour shaded) for (a) January, (b) June, (c) August, and (d) November.

2.4.6.2 Thermocline topography

The undulations in the depth of thermocline are an indication of the dynamical response of the ocean to the surface wind forcing. The depth of 20 °C isotherms (D20) at the tropical ocean often refers to the mid-thermocline at the tropics as shown by Carton et al. (2000) in Figure 2.11 from Simple Ocean Data Assimilation (SODA) product. The mid-thermocline isotherm deepens (shoals) in regions of Ekman convergence (divergence) with Ekman pumping velocity negative (positive). The relationship for the wind-driven Ekman transport is as follows.

$$\mathbf{M}_e = (M^x, M^y) = (1/\rho_o) \hat{\mathbf{K}} \times (\boldsymbol{\tau}/f),$$

Where $\boldsymbol{\tau}$ is the wind stress vector, $\hat{\mathbf{K}}$ is a unit vector in the z direction, and f is the Coriolis parameter. The Ekman transport is directed towards right (left) of the wind forcing ($\boldsymbol{\tau}$) in the

Northern (Southern) Hemisphere. The divergence of \mathbf{M}_e is often referred to as the Ekman Pumping velocity (w_{ek}) which is closely related to the wind stress curl.

It is generally known that the Ekman pumping velocity has close link with the climate. The w_{ek} is positive in those regions where the depth of 20 °C isotherm (D20) shoals, bringing cool subsurface water to the surface. It is more pertinent at the tropical south-western Indian Ocean (SWIO) especially from 5° to 10° S where shoaling of thermocline is observed all through the year in response to the Ekman drift generated by the trade winds. Similarly, the Ekman drift favours upwelling off Java and Sumatra during boreal summer associated with positive IOD events. However, the occurrence of Wyrтки Jets (Wyrтки, 1973) during inter-monsoon appears to transport warm water from the west to the eastern equatorial ocean that deepen the thermocline and weaken or eliminate upwelling there.

2.4.6.3 Sea Surface Temperature and Precipitation

The Sea Surface Temperature (SST) pattern over the tropical Indian Ocean appears to migrate along with the Sun. The migration of the thermal equator that associated with the Sun's oscillation moves northward during boreal summer and southward during winter. The precipitation patterns over the tropical Indian Ocean resembles closely with that of the temperature, prescribes strong coupling between the two fields.

2.4.7 Upper Ocean Circulation

General pattern of the upper ocean circulation fields in the Indian Ocean during summer and winter monsoon periods are summarised in the schematic diagrams (Figure 2.12 & 2.14). The circulation patterns in the northern Indian Ocean are more or less established during both seasons unlike south of 20° S, where several circulation elements were not quantified during the year of investigation and hence the pathways shown may not reproduce the true picture. However, the present investigation is largely restricted in the equatorial domain spanning from 10° N to 10° S and from 30° E to 100° E and hence the circulation pathways referred from these figures can be used with confidence to support the circulation pattern over the equatorial domain.

During the summer monsoon, the South Equatorial Current (SEC) and East African Coastal Current (EACC) contribute to the northward flowing Somali Current. After crossing the equator, part of the current turns offshore at about 4° N and the other part recirculate back to the southern hemisphere to join the Southern Gyre. The typical circulation patterns of the summer monsoon upper ocean circulation are displayed in Figure 2.12.

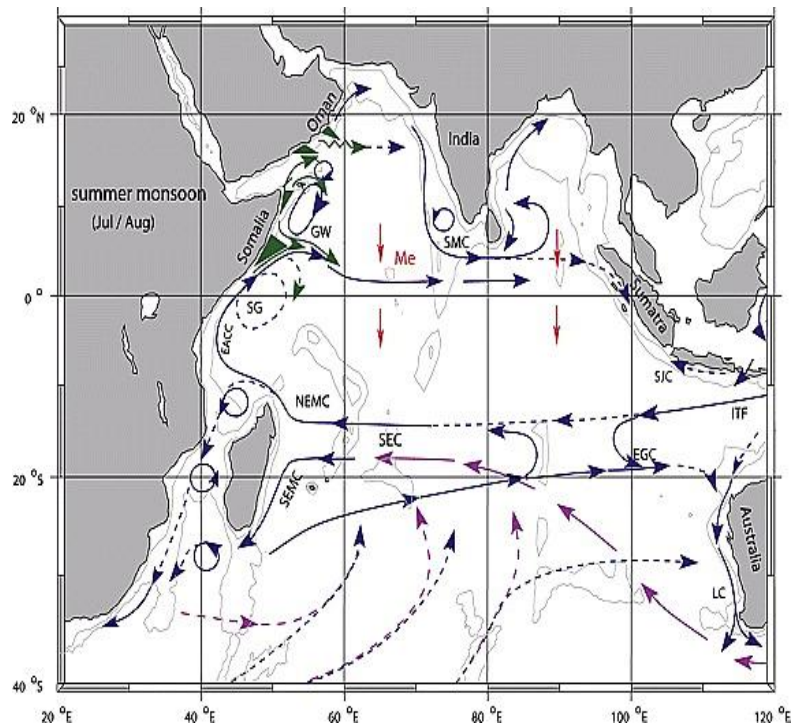


Figure 2.12 Schematic representation of identified current branches during the summer (southwest) monsoon. Current branches indicated are the South Equatorial Current (SEC), South Equatorial Counter Current (SECC), Northeast and Southeast Madagascar Current (NEMC and SEMC), East African Coastal Current (EACC), Somali Current (SC), Southern Gyre (SG) and Great Whirl (GW) and associated upwelling wedges (green shades), Southwest and Northeast Monsoon Currents (SMC and NMC), South Java Current (SJC), East Gyral Current (EGC), and Leeuwin Current (LC). The subsurface return flow of the super gyre is shown in magenta. Depth contours shown are for 1000 m and 3000 m (grey). Red vectors (Me) show directions of meridional Ekman transports. ITF indicates Indonesian Through flow. (Schott et al., 2009)

The summer monsoon winds further direct the current eastward south of Sri Lanka and then bifurcate northward into the Bay of Bengal. During the winter monsoon, the Somali Current reverse direction and flows southward meeting EACC in a confluence zone, feeding the eastward flowing South Equatorial Counter current (SECC) (Figure 2.13). Both from model (McCreary et

al., 1993) and reanalysis data (SODA-POP⁸ 2.0.3), it has been established that the SECC exists throughout the year except during summer monsoon where it goes subsurface and often masked by the westward flowing surface Ekman current. The winter monsoon current flows westward across the basin bringing fresher water to the Arabian Sea. Based on model studies of Han and McCreary (2001) and Jensen (2003), it has been observed that the Bay of Bengal water flows across the equator in the eastern equatorial basin during this season.

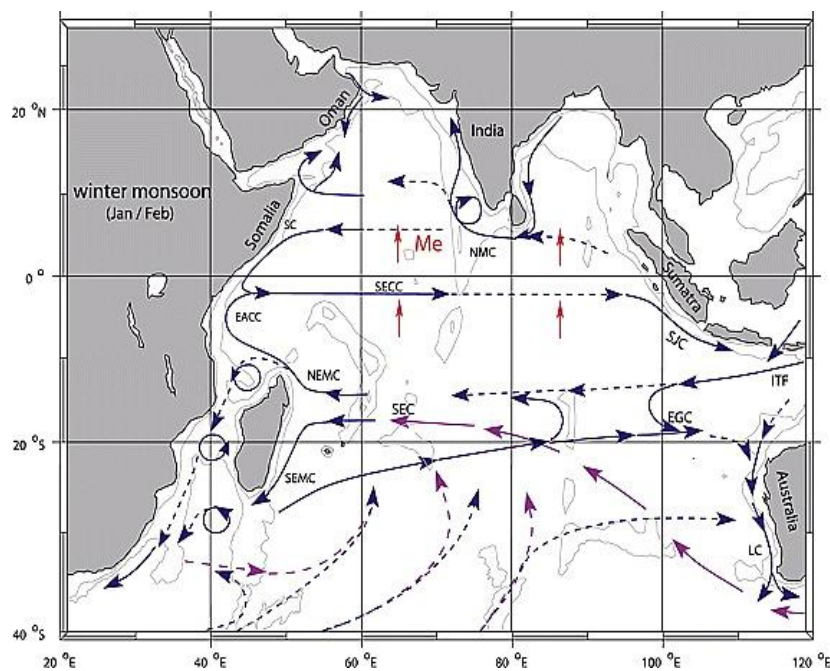


Figure 2.13 As in Figure 2.12 but for the winter (northeast) monsoon. (Schott et al. [2009])

2.4.7.1 Equatorial Indian Ocean

The intense eastward surface jets during the inter-monsoon periods, often referred to as Wyrтки Jets (WJs), are unique to the Indian Ocean driven by the semi-annual westerly equatorial winds. The WJs transports warm surface water to the east causing high sea level and thick mixed layer at the east and decreasing them westward. These dynamics make them climatically important. The eastward jet excites Kelvin waves along the equator. After hitting the eastern boundary of the basin, it propagates on either side of the equator as packets of coastal Kelvin and

⁸ The goal of (SODA Simple Ocean Data Assimilation ocean/sea ice reanalysis) is to reconstruct the historical physical and biogeochemical history of the ocean. The first version of the reanalysis is based on the Parallel Ocean Physics (POP). This model is referred to as SODA POP (Different versions are available). (source: history of SODA; university of Maryland)

Rossby waves. Hence their impact is felt well off the equator. These remote forcing interacts with the local wind-forced waves to impact the seasonal cycle of the equatorial regime and was studied by Yuan and Han (2006) using model analysis and observations. By interacting with the Sumatra upwelling regime, the WJs play a pivotal role in the IOD preconditioning.

Another peculiarity of the equatorial Indian Ocean is the absence of Equatorial Undercurrent (EUC), except during late winter to early summer, due to the absence of steady equatorial easterlies. There are intermittent appearances of EUC during other seasons when there are anomalous easterly winds (Reppin et al., 1999).

2.4.7.2 Meridional Overturning Cells

The northern and southern subtropical cells (STCs) present in both Pacific and Atlantic Oceans are shallow overturning circulations. Here the cold surface water subducts in the subtropics then transport to the equator roughly along the 20 °C isotherm and upwells in the eastern equatorial ocean (Schott et al., 2004). Unlike the Pacific and Atlantic, the IO lacks the steady equatorial easterlies and hence the primary upwelling areas shift to off equatorial regions such as coastal Somalia and Oman, tip of Indian Peninsula and at the southern thermocline ridge situated at 5°-10° S (Figure 2.11). These upwelling are the ascending limbs of the IO's shallow overturning circulations.

2.4.7.3 Cross-Equatorial Cell

The inter-hemispheric exchange of heat and mass occur predominantly due to Cross Equatorial Cell as shown by both observation and model studies (Schott et al., 2002; McCreary et al., 1993; Miyama et al., 2003; Schoenefeldt and Schott, 2006). The horizontal and vertical structures of CEC are illustrated in Figures 2.14a& b. The surface expression of the CEC displays the southward flowing cross equatorial Sverdrup transport while at thermocline depth it connects the SEC to the northward flowing Somali upwelling regime. The source of supply for the CEC

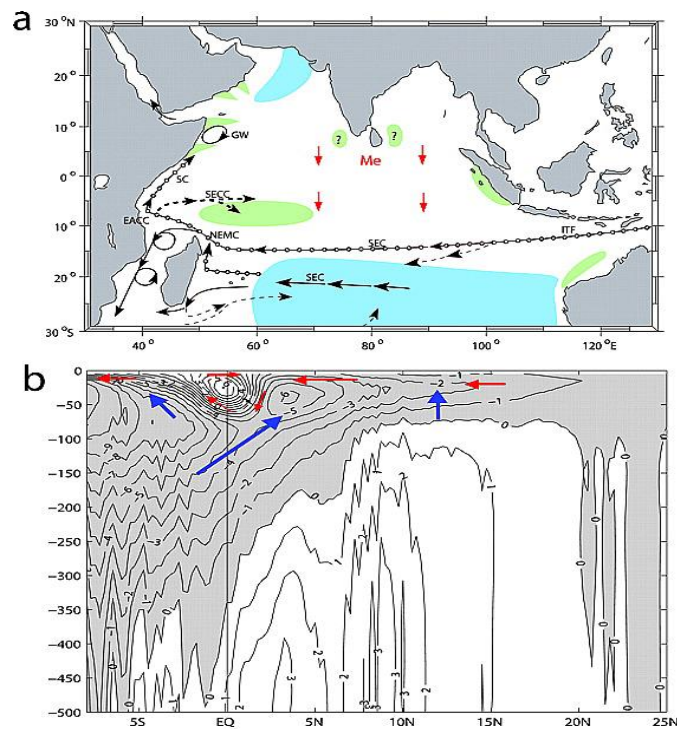


Figure 2.14 Indian Ocean cross equatorial cell shown schematically. (a) The subduction zone (blue), thermocline Somali Current (SC), the subtropical cell (STC) and the upwelling zones (green) based on (Schott et al., 2004). (b) Model generated (Miyama et al., 2003) mean overturning stream function (in Sv) showing Ekman transports (red vectors) and upwelling (blue) supplying to coastal upwelling regimes off Somalia, Arabia and the thermocline ridge (3-12 S).

comes partially from the recirculation within the subtropical gyre, subduction zones and through the ITF. The driving force of CEC is the zonally integrated wind stress curl along the equator manifested by the southward cross-equatorial Sverdrup transport (Godfrey et al., 2001; Miyama et al., 2003). The vanishing zonal component of the wind close to the equator during both monsoons appears to drive the CEC which is again roughly proportional to the distance on either side of the equator. Therefore, in the absence of the geostrophic currents, the cross-equatorial Sverdrup transport is equal to the Ekman drift because both τ^x and f vanish at the equator. Despite its shallowness, the CEC remains to be the decisive factor of cross-equatorial heat transport variability (Schoenefeldt and Schott, 2006). At the equator during both monsoon seasons the winds are more or less meridional and hence act against the Ekman transport causing it to form a minute equatorial overturning cell strictly confined to the surface-mixed layer (Wacongne and Pacanowski, 1996; Miyama et al., 2003). This miniscule process, therefore, has no impact on the oceanic heat budget or climate.

2.4.8 Inter-ocean Circulations

The inter-ocean circulation for Indian Ocean is predominantly occurring through the Indonesian passages and through the open southern boundary. The recent progresses in satellite technologies, the advanced *in situ* data collection programs and refined computational facilities, the quantification of the inter-ocean circulation is successfully attempted even at hostile and remote areas.

2.4.8.1 Indonesian through flow

Most of the transport from Pacific through ITF occurs at the upper 400m of the Ocean. Major portion of the water entering through ITF constitute the north Pacific water from Mindanao Current (Gordon, 2005) and the contribution from the South Pacific is evident at intermediate depths manifested as subsurface core (Gordon, 2005; McCreary et al., 2007). Through tidal mixing and internal wave breaking, intense water mass modifications occur at the Indonesian passages that give rise to a new water mass called Banda Sea Water that is identifiable by a salinity minimum all along the South Equatorial Current (Field and Gordon, 1992; Koch-Larrouy et al., 2007).

The mean through flow has been estimated to be about 10 Sv by combining measurements through various passages (Gordon, 2005). The computations through some global inverse model studies yielded even higher transports such as 15 ± 4 Sv and 13 ± 2 Sv by Ganachaud et al. (2000) and Lumpkin and Speer (2007) respectively. There is a seasonal cycle observed to the ITF with maximum outflow in June/July and minimum during February with amplitude of 3-4 Sv.

There is a seasonal cycle to the ITF, with maximum (minimum) outflow in June/July (February) and an amplitude of 3–4 Sv (Schott et al., 2009), and interannual variability related to ENSO and other forcing factors. Based on the repeat XBT sections across the ITF during 1970s to early 1990s it has been observed that the transport was higher during La Niñas than during El Niños (Meyers, 1996). But the observations of England and Huang (2005) using SODA reanalysis data from 1958 to 2001 indicated a rather low correlation between ENSO index and total through flow transport. In their study the ITF reduction appears to lag El Niño by 8 months.

Later, the reason for such low ITF- ENSO correlation was found to be the baroclinicity of the ITF transport variability by Potemra and Schneider (2007) using SODA reanalysis data and coupled model solution. Variations in transports in the upper 100 m within the ITF were mainly due to the interannual alongshore winds off Sumatra-Java and below 100 m were mainly driven by divergent winds between the equatorial Indian Ocean and Pacific Ocean.

2.4.9 Oceanic Processes

The SST anomalies caused by both oceanic and coupled processes often last enough to affect the regional climate. They can be further divided into processes that are primarily dynamical and thermo dynamical in nature.

2.4.9.1 Upwelling and Thermocline Depth

At the regions of upwelling, cool subsurface water replaces the surface warmer water and reduces the sea surface temperature. Those regions prone to upwelling are often linked to the atmospheric forcing through winds that tend to drive the upwelling. Tilting of thermocline is often noticed at regions of wind forced upwelling. Shoaling of thermocline implies divergence and often taken as a measure of the intensity of upwelling that generate low SST regimes. On the contrary deepening of thermocline is associated with convergence and gives rise to warmer SST regimes. It has been shown by McCreary (1981) that the wind driven upwelling is typically confined to the upper 100-200 m implying a modest shifting of thermocline depth. The repercussion is profound as it significantly changes the temperature of the upwelled water giving rise to anomalous SST regimes. The southern ridge (5-10° S) and off Sumatra are the key areas that witness similar process in the Indian Ocean.

2.4.9.2 Remote Forcing triggered by planetary Waves

The changes in thermocline depth are known to be driven by the local winds to generate upwelling and low SST regimes. Similar changes in thermocline depth can also be remotely driven by the propagation of baroclinic waves such as Kelvin and Rossby waves. The past studies indicate that the dynamics of those planetary scale waves are a prominent feature of the IO climatological circulation often generating converging/diverging zones especially at the equatorial region of the Indian Ocean basin. The impact of such waves crossing the equatorial

basin lies in the time it takes (from weeks to several months) to propagate across the basin making it possible to predict the variation in SSTs well in advance. Consider the response of the ocean to an easterly wind patch developed symmetric to the equator. In response to the wind the equatorially trapped upwelling Kelvin waves appear to propagate into the eastern ocean by shoaling the thermocline thereby triggering upwelling. The impinging Kelvin wave undergoes reflection at the eastern boundary and travel poleward in pockets of coastal Kelvin and Rossby waves. The poleward propagating Kelvin wave may be regarded as coastally trapped waves within a certain distance of the coast and beyond that distance the amplitude tend to decay and become discernible and the threshold distance is known as the Rossby radius of deformation, L , and can be calculated from $L=c/f$; where f is Coriolis parameter and c is the wave speed. The surface equatorial Kelvin wave travels very fast at about 200-300 cm/s (Gill, 1982) and their Rossby radius of deformation can be about 2000 km.

Rossby waves are the large-scale dynamical response of the ocean to wind and buoyancy forcing at the eastern boundaries and the ocean interior. Rossby waves arise from the need for potential vorticity conservation. Their surface manifestation might appear as slight rising of the mean sea surface height by a few centimetres and an increase in sea surface temperature by a fraction of a degree. Rossby waves travel westward at speeds of the order of 1–10 km/day (1.16–11.57 cm/s) carrying information from their source region. Consider the response to forcing by an off-equatorial patch of anticyclonic (downwelling) Ekman pumping in the eastern ocean. In response, downwelling favourable Rossby waves radiate from the forcing region, deepening the thermocline in the western ocean.

2.4.9.3 Bjerknes Feedback

A coupled positive feedback process between the ocean and atmosphere that links all the above processes such as easterly wind stress, thermocline depth, upwelling strength and the sea surface temperature as proposed by Bjerknes (1969). Then, “Bjerknes feedback” is the positive interaction loop summarized by

$$\Delta S S T_e \rightarrow \Delta \tau^x \rightarrow \Delta h_e \wedge -\Delta w_e \rightarrow \Delta S S T_e \text{ ----- (1)}$$

Where $\Delta \tau^x$, Δh_e , Δw_e , and $\Delta S S T_e$ represents the anomalies of zonal wind stress along the equator,

the thermocline depth, upwelling strength, and SST in the eastern equatorial ocean, respectively. The initial change can be either positive or negative, and the loop can start at any point in the cycle. For example, suppose that there is an initial decrease in SST_e . Then, according to (1), the equatorial easterlies (τ^x) strengthen in response to a stronger zonal SST gradient leading to shoaling of thermocline (h_e) by the equatorial trapped wave processes explained above followed by strengthening of upwelling (w_e) and a further decrease in SST_e . The suffix 'e' denotes the eastern equator. The schematics of these processes are shown in the clockwise loop shown at the right in Figure 2.15. There is a negative biological feedback at the eastern equatorial Pacific as shown by the left loop (anti-clockwise) in Figure 2.15. The stronger upwelling leads to enhanced chlorophyll concentration that support increased absorption of solar light in the clear sky situation. This absorption causes warming in the upper ocean that slows down the easterlies and weakens the La Niña event.

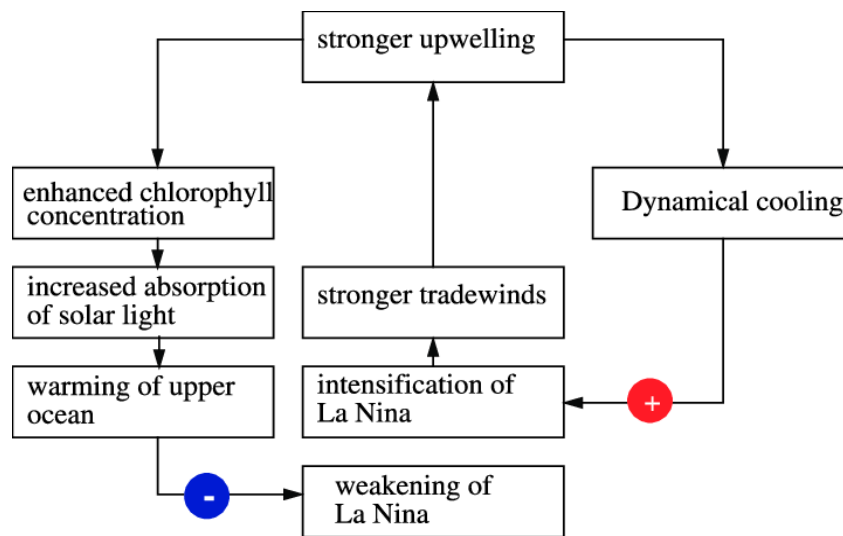


Figure 2.15 Schematic of the positive Bjerknes atmosphere-ocean feedback (right loop) and the negative biological feedback (left loop) in the eastern equatorial Pacific

Data and Methods

3.1 Introduction

This chapter describes in details the observational and model simulation data used in this thesis to study the long-term variabilities of current and hydrography at the tropical and equatorial Indian Ocean from inter-annual to decadal time scale. The observational data sets were mainly used for validating the long-term reanalysis/model products. The parameters used for addressing the inter-annual variability were currents, temperature at surface and depths, wind speed, wind stress and wind stress curl. For studying the decadal variability and trend analysis, the model derived temperature and salinity at both surface and subsurface have been extensively used after validating with observed data. The chapter also described briefly the empirical orthogonal function analysis and partial regression technique that have extensively been employed in this thesis for extracting the dominant modes of variability and disentangle the covariance observed in the inter-annual signals. The data and methodology used for studying inter-annual and decadal variabilities are given under the respective heads.

3.2 Inter-annual variability of currents and waves in the equatorial Indian Ocean

3.2.1 Model data set

The numerical simulation data used in this study is an output of DRAKKAR⁹ project (Brodeau et al., 2010). It is based on the NEMO (Nucleus for European Modelling of the Ocean) Ocean General Circulation Model (OGCM) with an eddy permitting $\frac{1}{4}^\circ$ horizontal resolution and 46 vertical levels with a 6-m spacing at the surface increasing to 250-m in the deep ocean.

⁹ DRAKKAR is a consortium of European ocean modelling teams. They are from France, Germany, Great Britain and Russia. More information on DRAKKAR can be found at (<http://www.ifremer.fr/lpo/drakkar>)

Bathymetry was represented with partial steps. The model was forced from 1958 to 2007 with the DFS3 dataset detailed in Brodeau et al. (2010). This forcing was essentially based on the corrected ERA-40 reanalysis (Uppala et al., 2005) before 2002 and ECMWF operational analysis beyond 2002 for near surface variables and corrected ISCCP-FD radiation product (Zhang et al., 2004) after 1984. The model simulation was initialized in 1958 with Levitus et al. (1998) climatology. Although, the simulation was run from 1958, it was analysed over the 1960-2007 period to allow the near equatorial ocean to spin-up over the first two years of the experiments.

This OGCM has been extensively validated with various forcing strategies in uncoupled mode (Vialard et al., 2001; Cravatte et al., 2007) and in coupled mode (Lengaigne et al., 2006; Lengaigne and Vecchi, 2009). This model accurately simulates equatorial dynamics and basin wide structures of currents and temperature in the tropics. This model was forced with a similar forcing strategy to successfully reproduce the variability over the Indian Ocean at a wide range of timescales (Akhil et al., 2014, 2016; Vialard et al., 2013) such as mixed layer variability in the Indian Ocean (Keerthi et al., 2013, 2016) and the decadal sea level variability in Indo-Pacific region (Nidheesh et al., 2013) also they reproduced observed equatorial currents and inter-annual variations of the heat content in the tropical Pacific (Lengaigne et al., 2012) accurately.

3.2.2 Observational data set

During the earlier stages of equatorial mooring experiment (1997) initiated under Ocean Observing Studies (OOS) program, Aanderaa Recording Current Meters were deployed at three locations to collect subsurface current speed and direction. Later in 2004, an upward looking Acoustic Doppler Current Profilers (ADCP) was added to the configuration to measure the currents above 400 m at closer intervals. The surface currents are not well captured by the ADCP profiler as they generate random errors. The near surface real time current velocity obtained from OSCAR (Ocean Surface Current Analysis Real-time) available from 1992 to date is used to validate the model simulated current velocity.

3.2.2.1 Moored Buoy/ADCP data

Model currents are validated using *in situ* velocity observations from upward looking Acoustic Doppler Current Profilers (ADCP) in the equatorial IO. In this study we made use of the relatively long measurements from RAMA moorings data and NIO-ADCP (more detailed

description on both mooring programs can be found on chapter 2) data from the locations viz. 77° E, 80.5° E, 83° E, 90° E and 93° E (Figure 3.1).

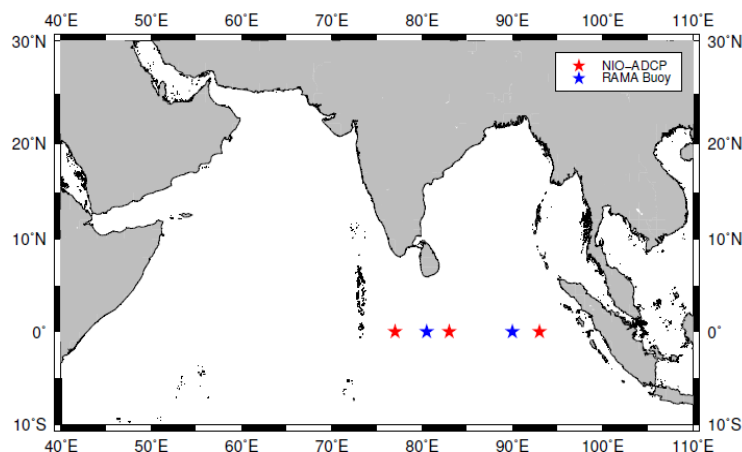


Figure 3.1 Location map of Acoustic Doppler Current Profiler moorings

Details of the current data from the ADCP mooring at the equatorial Indian Ocean is presented in the table 3.1. The frequent data gaps observed in the mooring at 83° E desist us from using it for the validation experiment by comparing it with model data in the subsurface depths in seasonal to inter-annual time scale. Similarly, the ADCP current time series at 93° E was not long enough to compute monthly mean. So, the data from these two moorings were discarded from the validation exercise.

Location	Record Length(Interval)	Depth(interval)
77E(NIO-ADCP)	01.01.2005– 25.11.2007(Daily)	48m– 180m(8m)
80.5E(RAMA-ADCP)	30.10.2004– 17.08.2012(Daily)	25m– 350m(5m)
83E(NIO-ADCP)	28.10.2004– 31.12.2007(Daily)	48m– 112m(8m)
90E(RAMA-ADCP)	14.11.2000– 24.01.2014(Daily)	30m–410m(10m)
93E(NIO-ADCP)	19.09.2006– 31.12.2007(Daily)	96m – 472m(8m)

Table 3.1 Details of ADCP data used for model validation.

3.2.2.2 OSCAR data

The upward looking ADCP often generate random errors in the surface currents as they are contaminated by acoustic signals reflected off the surface. Therefore, the model surface currents were validated using the near surface real time velocity data from OSCAR (Ocean

Surface Current Analysis Real-time) project available from November 1992 to present (Bonjean and Lagerloef, 2002). OSCAR is a NASA (National Aeronautics and Space Administration, USA) funded project to improve the calculation of near real time ocean currents. Currents were derived using quasi-linear and steady flow momentum equations (Bonjean and Lagerloef, 2002), a model based on Ekman dynamics. This model calculates the surface current averaged over the top 30m of the upper ocean with a five-day interval time. The sources of datasets were satellite derived Sea Surface Height (SSH), Wind speed (W) and Sea Surface Temperature (SST). The SSHs were obtained from TOPEX/POSEIDON and JASON-I (Lagerloef et al., 1999) missions. Wind speed was provided by the variational analysis Special Sensor Microwave Imager (SSM/I) winds (Atlas et al., 1996; October 1991 to September 2001) and the QuikSCAT gridded winds from COAPS (Center for Ocean-Atmospheric Prediction Studies) (August 2001 to present).

For SST, Reynolds and Smith's version 2 SST, a product blended from satellite and *in situ* data (Reynolds et al., 2002) were used. This current estimation was provided on 1° and 1/3° resolution grid from November 1992 to till date and they are updated on every week. The Earth and Space Research continually performs extensive calibration and validation of these current estimates using both 15 m drogued drifters (World Wide Drifter Buoy Deployment Data, http://www.aoml.noaa.gov/phod/dac/gdp_doc.html) and with moorings from the TAO/TRITON and PIRATA arrays, from the PMEL Ocean Climate Station (OCS), and other available time series *in situ* data. The data is freely available through the NASA Physical Oceanography Data Centre (PO. DAAC). The NASA (PO. DAAC) site (<http://podaac.jpl.nasa.gov>, Dataset “Ocean Circulation”) serves OSCAR currents on both 1 degree and 1/3° grid spacing in NETCDF format.

3.2.3 Model validation

3.2.3.1 The seasonal circulation – Surface currents

Seasonal variations of surface currents in the equatorial Indian Ocean from both OSCAR current data set and model outputs were compared (Figure 3.2). The zonal time series of OSCAR

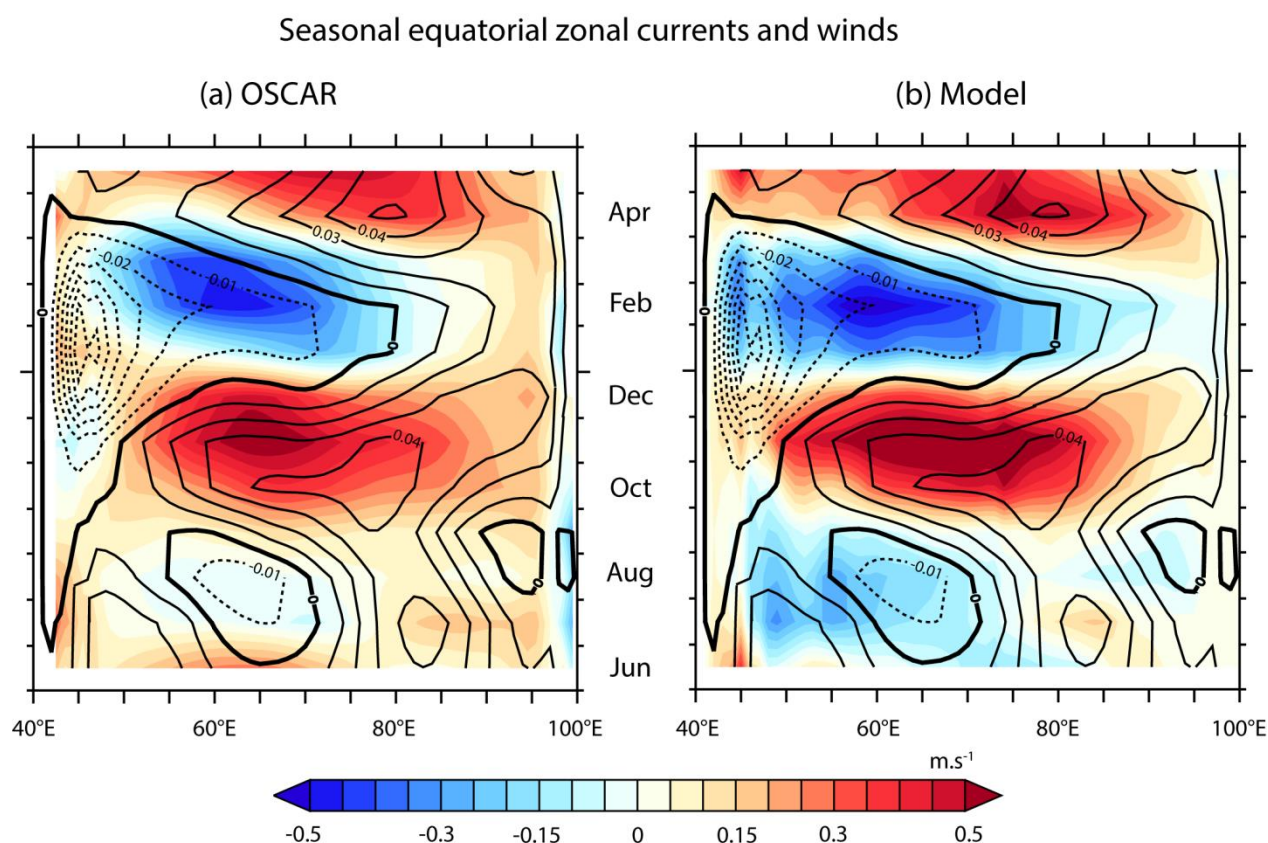


Figure 3.2 Longitude-time evolution of seasonal climatology of equatorial zonal surface currents from (a) OSCAR dataset and (b) model outputs. The corresponding zonal wind stress climatology from the model is overlaid on each panel. These climatologies are computed over the common 1993-2007 period. Units are in m/s for currents and $\text{N}\cdot\text{m}^{-2}$ for wind stresses.

data depict the evolution of seasonal surface current pattern along the equatorial Indian Ocean is displayed in Figure 3.2a. Oscar data revealed that the fall Wyrtki jet was maximum in November (up to 0.5 m/s) in the central IO between 60°E and 80°E . The spring Wyrtki jet was maximum in May. This jet was slightly weaker (up to 0.4 m/s) and did not last as long as its fall-counterpart. These seasonal surface eastward jets occurred during the biannual intensification of equatorial westerly winds and exhibited an apparent westward propagation that had been attributed to a superposition of Rossby wave signature on a wind forced jet (Nagura and McPhaden, 2010b).

Westward flow driven by the trade wind was found during winter in the west of the basin (December-January) while weak currents prevailed during the summer season (July-August). As shown in Figure 3.2b, the model was able to capture accurately these seasonal features both in terms of seasonal phasing and amplitude, despite a slight eastward surface current bias during

winter. The seasonal correlations between model and observed surface currents were highly significant and range between 0.8 and 1 all along the equator strip (Figure 3.3).

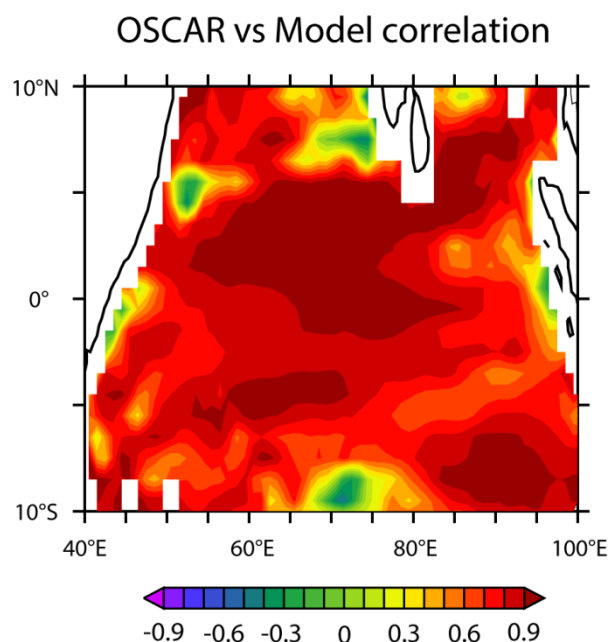


Figure 3.3 Correlation map between the seasonal currents from OSCAR and the model output. These seasonal currents are computed over the common 1993-2007 period.

3.2.3.2 The seasonal circulation- Currents at the depth

The mean seasonal cycle of subsurface currents in the equatorial central and eastern IO from the model output was compared with RAMA moorings and NIO- ADCP (77° E) (Figure 3.4). The figure illustrates that, at 77° E & 80.5° E, the surface jets were generally confined to the upper 60 to 80 m of the water column (Figure 3.4a&b). Model data compared well with both RAMA and NIO moorings exhibiting maximum amplitude of ~0.5 m/s around 60 m depth. Further east at 90° E, there was no surface current maximum in fall and the spring jet was less intense. The model is able to reproduce these seasonal fluctuations of the surface currents. From the figure it was evident that a transient eastward undercurrent was present at depth during late summer/early fall (August-October) and later winter/early spring (January-April). The direction of the zonal flow generally reversed during other seasons.

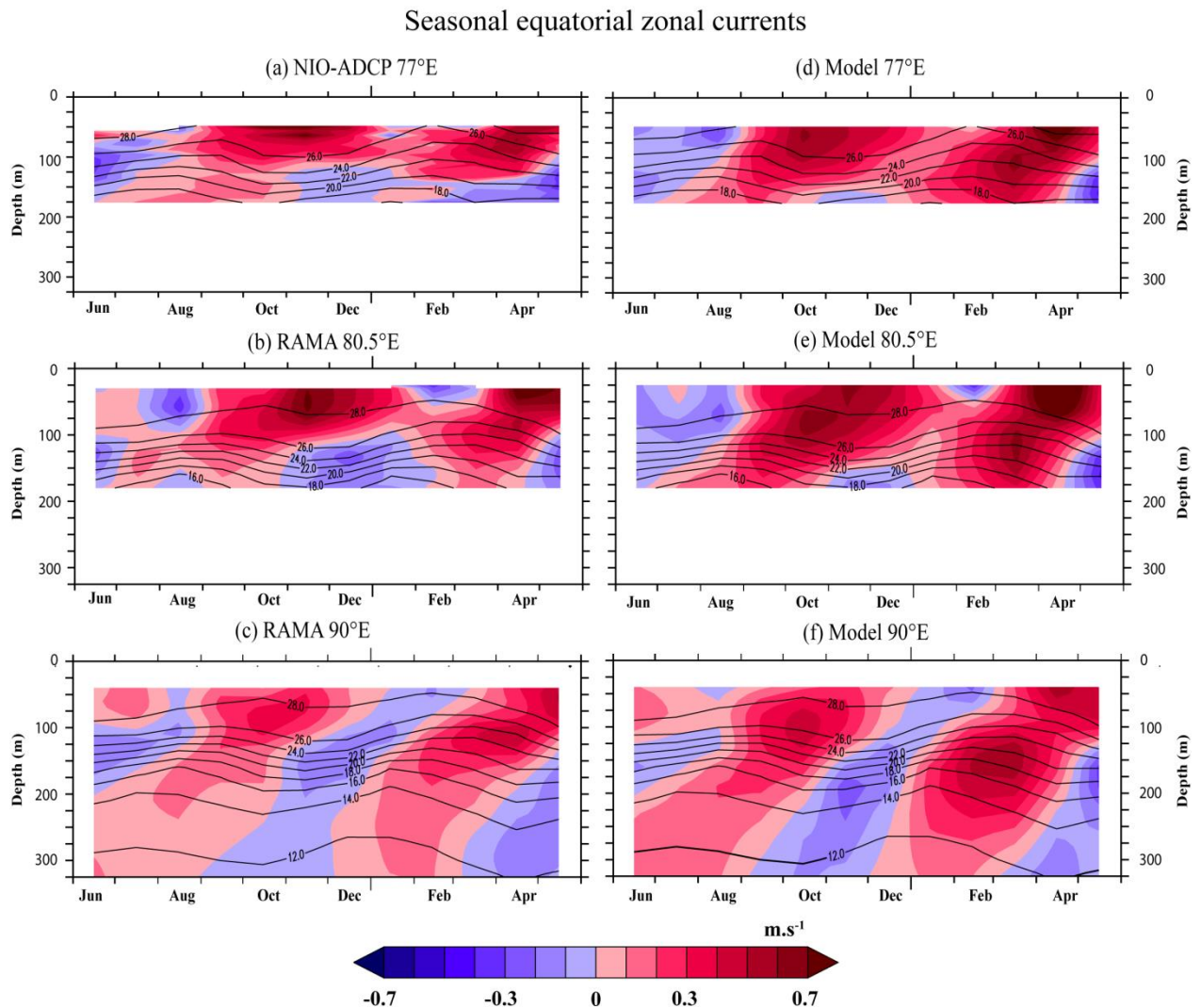


Figure 3.4 Vertical section of seasonal equatorial zonal currents (colour) and temperature (contour) at (left) 77° E, 80.5° E and (right) 90° E from (a) NIO-ADCP, (b & c) RAMA moorings and (d, e & f) model output. Seasonal climatologies are calculated from January 2005 to December 2007 at 77° E, November 2004 to December 2007 at 80.5° E and from November 2000 to December 2007 at 90° E for both datasets. Units are in m/s.

These subsurface currents generally lead the surface signals. The eastward transient undercurrents were even more prominent in the eastern most location (90° E; Figure 3.4c), while they tend to merge with the surface jets in the central IO (77° E, 80° E; Figure 3.4a&b). The model was able to simulate the seasonal occurrence of these seasonal surface jets and undercurrents at 77° E, 80.5° E and 90° E (Figure 3.4d,e&f). However, the model tends to slightly overestimate their maximum amplitude and the depth of their maximum which was deeper by 30m than in observations. The seasonal correlations between model and the observed currents were highly significant within the range from 0.8 to 1 at all depth for both 80.5° E and

90°E (Figure 3.5b&c). However, at 77° E, the seasonal correlations indicated slight deterioration above 70m and below 125m (Figure 3.5a). The model also accurately captured the seasonal thermocline variations at all the three locations (see black contours on Figure 3.4).

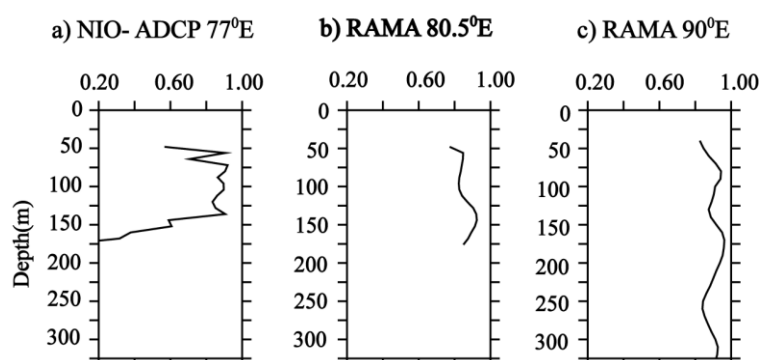


Figure 3.5 Correlation values for vertical section of seasonal equatorial zonal currents at (a) 77° E (NIO-ADCP), (b) 80.5° E (RAMA) and (c) 90° E (RAMA) between moorings and model output. Seasonal climatologies are calculated from January 2005 to December 2007 at 77° E, November 2004 to December 2007 at 80.5° E and from November 2000 to December 2007 at 90° E for both datasets. Units are in m/s.

3.2.3.3 Inter-annual circulation – Surface currents

Figure 3.6 displayed the validation of inter-annual surface current variability in the model by highlighting the inter-annual standard deviation of zonal currents in the equatorial IO for both OSCAR and the model outputs (Figure 3.6a&b) and their corresponding spatial correlations (Figure 3.6c). Both data sets showed maximum inter-annual zonal current variations at the equator between 60° E and 90° E. The maximum amplitude of these equatorial current variations appeared to be larger and slightly shifted eastward in the model as compared to OSCAR current data. Despite these biases, Figure 3.6c revealed that the model was able to capture the phasing very accurately in the interannual variations of surface currents in a broad strip around the equator, with significant correlations generally exceeding 0.7 between 7° N and 7° S. These correlations generally dropped down outside this region, with correlation ranging between 0.4 and 0.7.

3.2.3.4 Inter-annual circulation- currents at depths

For currents at depths, only RAMA buoys data have been used for validating the model as the NIO- ADCP data at 77° E had large data gaps at depths and hence was not considered for

validation. Interannual variations of vertical current profiles along the equator at both 80.5° E and 90° E derived from RAMA moorings and model data were displayed in Figure 3.7.

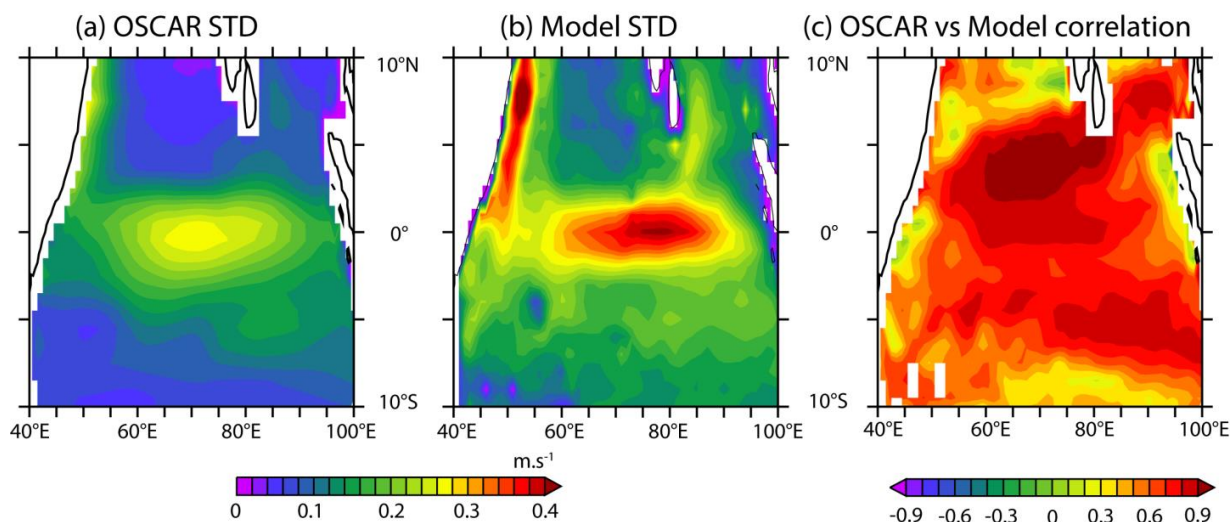


Figure 3.6 Standard deviation maps of interannual zonal surface currents from (a) OSCAR dataset (b) model output. (c) Correlation maps between interannual zonal current anomalies derived from OSCAR and model outputs. Interannual anomalies from both datasets are calculated over the 1993-2007 period.

The surface (Figure 3.6) and subsurface (Figure 3.7) observations exhibited large interannual zonal currents fluctuation especially from central to eastern equatorial Indian Ocean. However, at depth the interannual variations are significant ranging from -0.7 to 0.7 m/s. Interannual currents fluctuations appeared to be slightly weaker and more transient at 90° E (Figure 3.7b). The model was shown to capture very accurately most of these interannual current fluctuations at both locations (contours vs. shading on Figure 3.7). At 80.5° E, the correlation between interannual zonal currents from buoys and model was 0.80 in the first 125m and drops down to 0.60 at 150 m depth (Figure 3.7c). At the easternmost location (90° E), the correlation between model and observations reaches 0.6 from the near surface zone (25 m) to 200 m and then gradually decreases to 0.40 at 250 m depth (Figure 3.7d). These results clearly demonstrate that the model accurately captured the surface and subsurface currents variations at both seasonal and interannual timescales, giving us confidence in using this dataset to describe the interannual variability of the current system and their relationship with IOD and ENSO variations.

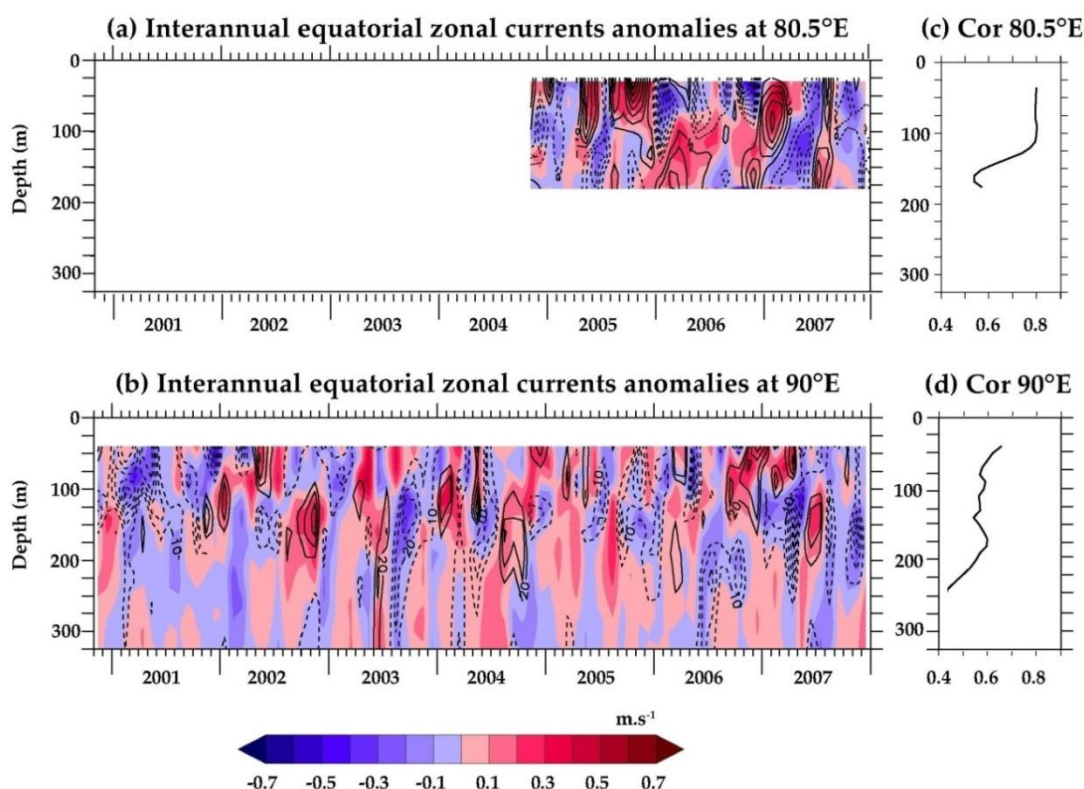


Figure 3.7 Interannual anomalies of equatorial zonal currents at (a) 80.5° E and (b) 90° E from RAMA buoys (shaded) and simulation (contour). Corresponding correlations between modelled and observed interannual anomalies of equatorial zonal currents at (c) 80.5° E and (d) 90° E. Anomalies are calculated from their respective monthly climatology (October 2004 to December 2007 at 80.5° E and November 2000 to December 2007 at 90° E location).

3.3 Changes in inter-annual variability of surface temperature at the equatorial Indian Ocean in different epochs

3.3.1 Model data set

NEMO (Nucleus for European Modelling of the Ocean) model surface temperature from 1960-2007 had been used to study epochal evolution of inter-annual temperature at equatorial Indian Ocean (a more detailed description about the model, forcing mechanism could be seen in first section of this chapter). We have made an attempt to study the patterns of variability of temperature in the inter-annual time scale over the equatorial Indian Ocean in pre and post climate shift era using the same NEMO simulation validated in the previous section. Moreover,

the temperature from this model with similar forcing strategy has been validated from intra-seasonal to inter-annual time scales over the Indian Ocean by Keerthi et al. (2013, 2016).

The inter-annual temperature signals had been calculated by first removing monthly climatology. A three-month running mean was then applied to filter out the seasonal oscillations. In order to study the variability of temperature related to climate shift of 1976-1977, the filtered temperature anomalies were divided into two time period groups called as epochs, from 1960 to 1976 and from 1977 to 2007 respectively. Here after, 1960-76 period is called PRE76 and 1977-07 is called POST76. Our aim was to assess the relationship between Indian Ocean equatorial temperature and climate modes in the Indian Ocean, i.e. the Indian Ocean Dipole (IOD) and El Niño-Southern Oscillation (ENSO) in both epochs. Standard indices had been used to characterize these modes. ENSO was measured as the mean sea surface temperature over the region called Niño3.4 (120° W – 170° W; 5° N – 5° S) over the period December-February. The Indian Ocean Dipole was measured by an index called Dipole Mode Index (DMI) (Saji et al., 1999), which was the difference between the inter annual sea surface temperature anomalies over the Western equatorial Indian Ocean (50° E - 70° E; 10° N - 10° S) and south eastern equatorial Indian Ocean (90° E - 110° E; 10° S - 0°), averaged over the September-November season. These two indices had been calculated using monthly HADISST dataset (Rayner et al., 2003).

3.3.2 Climate indices definition

As we intend to assess the relationship between the variability of Indian Ocean equatorial currents and known climatic modes such as IOD and ENSO. Standard indices have been used to characterize these modes. In the Pacific Ocean, ENSO is classically represented by the mean sea surface temperature (SST) anomalies over the Niño3.4 (120° W - 170° W; 5° N - 5° S) region averaged from December to February. In the Indian Ocean, IOD is represented by the dipole mode index(DMI, Saji et al., 1999), which was computed as the difference between inter-annual SST anomalies in the western(50° E - 70° E;10° N - 10° S) and south-eastern equatorial Indian Ocean(90° E - 110° E; 10° S - 0°) averaged over September to November season. These two indices were computed from the monthly HADISST data set (Rayner et al., 2003). These two indices were strongly correlated (~0.65), confirming the tendency for IOD and ENSO to co-occur (Figure 3.8).

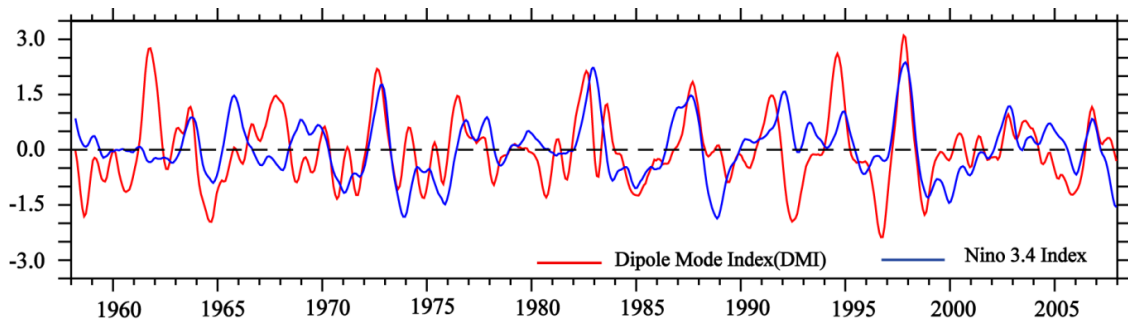


Figure 3.8 Climate indices calculated using HADISST data from 1958 to 2007.

3.3.3 Statistical methods

For getting inter annual signals, first monthly anomalies for both the model and observational datasets were calculated by removing the monthly climatology. A three-month running mean was then applied on these monthly anomalies to filter out the intra seasonal signals.

3.3.3.1 Empirical Orthogonal Function Analysis

Empirical Orthogonal Function (EOF) analysis was used to study possible spatial modes or patterns of variability and how these patterns vary with time. In statistics, EOF analysis was known as Principal Component Analysis (PCA). So, this analysis was sometimes classified as a multivariate statistical technique. However, there was no priori hypothesis based on any kind of probability distribution and hence no statistical test. Also, EOF analysis was not based physical principles. Rather, a field or data matrix was partitioned into mathematically orthogonal (means independent) modes which were interpreted as atmospheric and oceanographic modes or structures. EOFs were found by computing the eigenvalues and eigenvectors of spatially weighted anomaly covariance matrix of data set of particular interest. Each mode in EOF output was explained by percentage of variance from the derived eigenvalues. In atmospheric and oceanographic studies, most of the variance contained in first few modes. There were two factors inhibit the physical interpretation of EOFs: -

1. The orthogonality constraint
2. The derived patterns may be domain dependent.

Even though these shortcomings are there in this analysis, still EOFs are proved to be the most useful tool for identifying patterns from large data sets used in climate studies.

In this study, we have subjected the 3-month smoothed model output of zonal current anomalies to EOF analysis to get the main patterns of variability at the equatorial Indian Ocean during 1960-2007. Both spatial patterns and temporal fields (called as Principal components or PC) have been used to explain the processes in the inter-annual time scale.

3.3.3.2 Partial Regression Analysis

Partial regression analysis has been used extensively to study the relationship between a parameter and the known climate modes (IOD and ENSO) independent of one another. In this study our intent was to study the relationship between the IO equatorial currents and the known climate modes, i.e. IOD and ENSO. Because of strong correlation exists between the indices (~0.65, between IOD and ENSO indices), it was often difficult to separate the signals associated with each of these climate modes using a simple linear regression. Partial regression was hence used to isolate signals purely associated with, either IOD or ENSO. This computation required three linear regressions. As for example, if one wants to calculate the partial regression between time series of currents (Cur_i) and the DMI index(D_i) independently of the ENSO index (E_i), first subtract signals that are linearly related to (E_i) from (Cur_i) and (D_i) and perform a regression between the residuals as given below.

$$Cur_i = a \times E_i + Cur_e \quad (1)$$

$$D_i = b \times E_i + D_e \quad (2)$$

$$Cur_e = c \times D_e + M_{ed} \quad (3)$$

where Cur_e and D_e (in Eqs.1 and 2) are respectively the M_i and D_i residuals independent of ENSO. Equation 3 allows obtaining the partial regression coefficient c by regressing M_e onto D_e , while M_{ed} is the residual independent of both IOD and ENSO signals.

3.3.3.3 Partial Correlation Analysis

We have seen that the IOD and ENSO are strongly correlated each other. So, it was often very difficult to separate out their respective influence using simple correlation analysis. Hence

partial correlation analysis (Yule and Kendall, 1950; Panofsky and Brier, 1958) had been used in such cases. Partial correlation was often explained as finding the correlation between two variables while controlling for the cross correlation between independent variables. This analysis had been used for separating the individual influence of IOD and ENSO in the recent studies (Saji and Yamagata, 2003; Yu et al., 2005; Gnanaseelan et al., 2012). Partial correlation is computed as

$$r_{xy.z} = \frac{r_{xz} - r_{xz} \cdot r_{yz}}{\sqrt{(1 - r_{xz}^2) \cdot (1 - r_{yz}^2)}}$$

For example, if one wants to compute the partial correlation between surface temperature and Indian Ocean Dipole, then

$$r_{temp,dmi.nino} = \frac{r_{temp,dmi} - r_{temp,nino} \cdot r_{dmi,nino}}{\sqrt{(1 - r_{temp,nino}^2) \cdot (1 - r_{dmi,nino}^2)}}$$

Where $r_{temp,dmi.nino}$ is the partial correlation between surface temperature and IOD with ENSO effect is isolated, $r_{temp,dmi}$ is the correlation between surface temperature and IOD index, $r_{temp,nino}$ is the correlation between surface temperature and ENSO index and $r_{dmi,nino}$ is the correlation between IOD and ENSO index.

3.3.3.4 Fisher's r to z transformation for comparing correlations

In order to compare the correlation between climate modes and equatorial Indian Ocean temperature on both epochs, a new statistical test has been used, known as Fisher's r to z transformation. Comparison of correlation values between two groups of data can be done only if the correlations were conducted on same variable with different sample sizes and if both correlations were statistically significant. The way to do this is by using Fisher's r to z transformation. The first step in this analysis was finding the correlation value r between the samples (negative signs are ignored). Then noted down the sample size of the two groups. Now determine the Z scores (Z score is the measure of number of standard deviations below or above

the population mean, a raw score is) corresponding to the r values. Then determine the observed z score by the formula

$$Z_{\text{observed}} = \frac{Z_1 - Z_2}{\sqrt{\left[\left(\frac{1}{N_1} - 3\right) + \left(\frac{1}{N_2} - 3\right)\right]}}$$

Where Z_{observed} is the observed z score, Z_1 value is the z score of correlation of dataset1, Z_2 is the correlation of dataset 2, N_1 is the sample size of dataset1 and N_2 is the sample size of dataset2.

Once the observed Z value has been determined, statistical significance can be assessed by checking to see if the observed value is greater than critical value.

In this study, we had used a widely accepted online statistics analysis tool, ‘Free Statistics Calculators (version 4.0)’ (<https://danielsoper.com/statcalc>) for performing Fisher’s r to z transformation to compare the correlation values between the parameters in PRE76 and POST76 period.

3.4 Variability and trend analysis of hydrographical parameters in the decadal time scale

3.4.1 Trend analysis

Detection, estimation and prediction of trends and their associated statistical and physical significance were important aspects of long-term climate studies. The trend of any parameter/variable can be linear or non-linear. However, generally it is the linear slope of the line fit to the time series. So, simple linear regression is most commonly used method for calculating trends. Linear regression is the basic and simplest form of predictive analysis. These regression estimates were used to explain the relationship between one dependant variable and one or more independent variables. The basic form of linear regression equation with one dependant and one independent variable is defined by the formula

$$Y = C + B \cdot X$$

Where Y is the estimated dependant variable value, C is the constant, B is the regression estimate and X is the independent variable.

3.4.2 Observational data products

The **Hadley Centre Global Sea Ice and Sea Surface Temperature** (HADISST) comprises of global monthly fields of SST as well as sea ice concentration data available from the year 1871 onwards. HADISST uses reduced space optimal interpolation applied to SSTs from the Marine Data Bank (mainly ship tracks) and ICOADS (International Comprehensive Ocean Atmospheric Data Set) through 1981 and a blend of *in situ* and adjusted satellite-derived SSTs for 1982-onwards. HADISST was primarily intended to be used as boundary conditions for atmospheric models. For a detailed description of the dataset and its production process, refer the paper Rayner et al. (2003).

Array of Real time Geostrophic Oceanography (ARGO) is a global array of temperature and salinity profiling floats started in the year 2000 for observing the ocean system. It gives temperature and salinity data from near surface to 1000m depth. They were the sole source of subsurface data. They provide quantitative description of changing state of the upper ocean and the patterns of ocean climate variability from months to decades. The gridded ARGO data products were freely available on Asia Pacific Data Research Center (www.apdrc.soest.hawaii) website. In this work, Argo data for the period 2002-2004 was taken from Indian National Center for Ocean Information systems (INCOIS) data center and for the period 2005-2014 was taken from APDRC. Both data sets were combined to form a longer time series in order to perform validation in the decadal time scale. Even though both data sets were 1x1 degree gridded spatially, values were not available on all grid points, because of the fewer number of floats were operational on 2002- 2004 periods.

3.4.3 Reanalysis/model data products

Ocean Reanalysis/Analysis System4 (ORAS4) used version 3.0 of the Nucleus for European Modelling of the Ocean (NEMO) ocean model in the ORCA¹⁰1 horizontal discretization (Madec, 2008). The ORCA1 configuration has a 1°-horizontal resolution in the extra-tropics and a refined meridional resolution in the tropics with a minimum value of 0.3° directly at the equator. It has 42 vertical levels of which the first 18 correspond to the upper 200 m. The vertical discretization in ORAS4 used partial steps in order to have better representation of the flow over steep topography. The model relaxes weakly (20-year time scale) to climatological salinity and temperature from the World Ocean Atlas 2005 (WOA05) (Antonov et al., 2006). The model assimilates temperature, salinity and along-track satellite derived SSHA. There was no assimilation of velocity observations. The temperature and salinity profiles were obtained from expendable Bathy Thermographs (XBTs), Conductivity-Temperature-Depth (CTD) sensors, TAO/TRITON/PIRATA/RAMA moorings and Autonomous Pinniped Bathythermograph (APBs). The SSHA data were obtained from AVISO. ORAS4 was forced by atmospheric-derived daily surface fluxes of solar radiation, total heat flux, evaporation minus precipitation (E-P), and surface wind stress from ERA40 reanalysis (Uppala et al., 2005), from September 1957 to December 1989, ERA-Interim reanalysis (Dee et al., 2011) from January 1989 to December 2009 and the ECMWF operational archive from January 2010 onward. The heat flux was corrected by a strong relaxation to gridded SST products via a relaxation coefficient of 200 W/m²/ °C. Additionally, the E-P was adjusted globally by constraining the global-model sea-level changes to the changes derived from altimeter data and locally by relaxation to monthly climatology of surface salinity from WOA05. The model data is available for the period 1958-2015. The available outputs from this model are temperature, salinity and ocean current velocity. For present study 1x1 monthly gridded temperature and salinity data from 1960-2014 had been used.

The ECCO (Estimating the Circulation and Climate of the Ocean) Project is a consortium of the Jet Propulsion Laboratory (JPL), The Massachusetts Institute of Technology (MIT) and the Scripps Institution of Oceanography and was funded through grant from the National Oceanographic Partnership Program (NOPP). German contribution of **ECCO** is known

¹⁰ ORCA is a generic name that is used to refer to the tri-polar grids in the NEMO model.

as **GECCO** (Köhl, 2015). The synthesis uses the adjoin method to adjust the initial temperature and salinity in 1948 together with the air temperature, humidity, precipitation, and zonal and meridional wind every 10 days to bring the model into consistency with the data, which derive from the EN3v2 data base AVISO along track SLA, GOCO mean dynamic topography, AMSRE SST, and the WOA09 climatology. The global model was based on the MITgcm model, had 50 levels, and used zonally 1° and meridionally varying to higher resolution. The background atmospheric state was taken from the 6 hourly NCEP/NCAR Reanalysis 1. The data was available from 1948-2014. The gridded ($1^\circ \times 1^\circ$) Monthly mean temperature and salinity data for the period 1950-2014 is used for studying the decadal patterns. Table 3.2 is presented for a quick reference to the data used in this study.

DATA	Variables	Spatial Domain	Period	Type
HADISST	Sea surface temperature	Indian Ocean	1960-2014	In-situ (gridded)
ARGO (from INCOIS)	Temperature(0-1000m)	Indian Ocean	2002-2004	In-situ (gridded)
	Salinity(0-1000m)			
ARGO (from APDRC)	Temperature(0-1000m)	Indian Ocean	2005-2014	In-situ (gridded)
	Salinity(0-1000m)			
ORAS4	Temperature(0-1000m)	Indian Ocean	1958-2014	Reanalysis/Model (gridded,1X1)
	Salinity(0-1000m)			
GECCO2	Temperature(0-1000m)	Indian Ocean	1948-2014	Model (gridded,1X1)
	Salinity(0-1000m)			

Table 3.2 Brief description of observational and model data used in this chapter

3.4.4 Validation of model data – At the surface

Two model data products namely ORAS4 and GECCO2 had been chosen for the validation study by comparing with observed sea surface temperature data from HADISST. Sea surface salinity had not been included in the validation study in the decadal time scale because of two reasons. Primarily the surface salinity in the equatorial Indian Ocean is considered to be a highly variable parameter due to the proximity of high saline Arabian Sea and the low saline Bay of Bengal and their constant interaction at the equatorial zone due to the seasonally reversing wind system. Moreover, none of the observation platforms in the equatorial Indian Ocean

provided accurate and uninterrupted sea surface salinity values in longer time scales. Even the widely accepted ARGO profiles do not give accurate surface salinity due to the inherent technical issues. However, the validation of subsurface salinity was carried out at specified locations based on the availability of continuous time series data.

3.4.4.1 ORAS4 and HADISST data

Surface temperature from ORAS4 simulation and HADISST data had been compared for common time period 1960-2014. Climatological mean had been subtracted from monthly fields of both data sets to enhance the inter-annual signals. Then an 84-month running mean was applied on both data to retain only the decadal oscillations. Three parameters have been studied to understand the level of acceptance of the data. They are standard deviation of the decadal signals in observation and model data, Coefficient of Correlation and Root Mean Square Error between the observation and model data. The pattern of standard deviation displayed in the HADISST was not well represented in the ORAS4 data (Figure 3.9a & b).

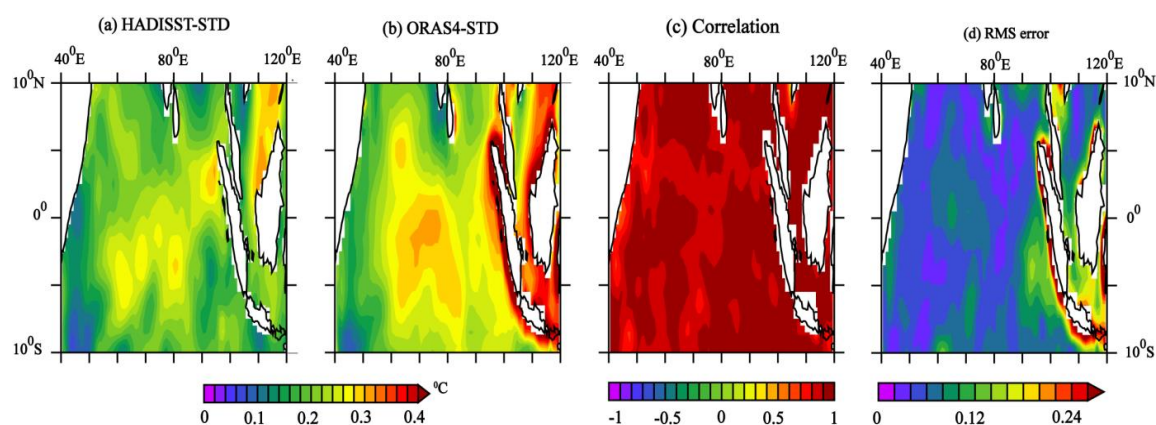


Figure 3.9 Standard deviations from HADISST (a) and ORAS4 (b) data are plotted at the equatorial domain during 1960-2014 periods. Coefficient of correlation (c) and RMS error (d) between model and *in situ* data are plotted during the same period.

Relatively higher patches of standard deviation were seen diagonally from north to south in the observed data (Figure 3.9a) with low values elsewhere in the equatorial domain. Whereas the model predicted high values all along the central and eastern equatorial regions with low values mainly confined to the western boundary (Figure 3.9b). However, the coefficient of correlation map displayed high and relatively low correlation patches spread throughout the equatorial

domain (Figure 3.9c) with insignificant RMS error spread all over the domain except the eastern periphery where slightly high values were observed (Figure 3.9d).

3.4.4.2 GECCO2 and HADISST data

Surface temperature from HADISST data and GECCO2 model simulation had been compared for common time period 1960-2014. Climatological mean had been subtracted from the monthly fields. An 84-month running mean is then applied on both data, to retain only decadal oscillations.

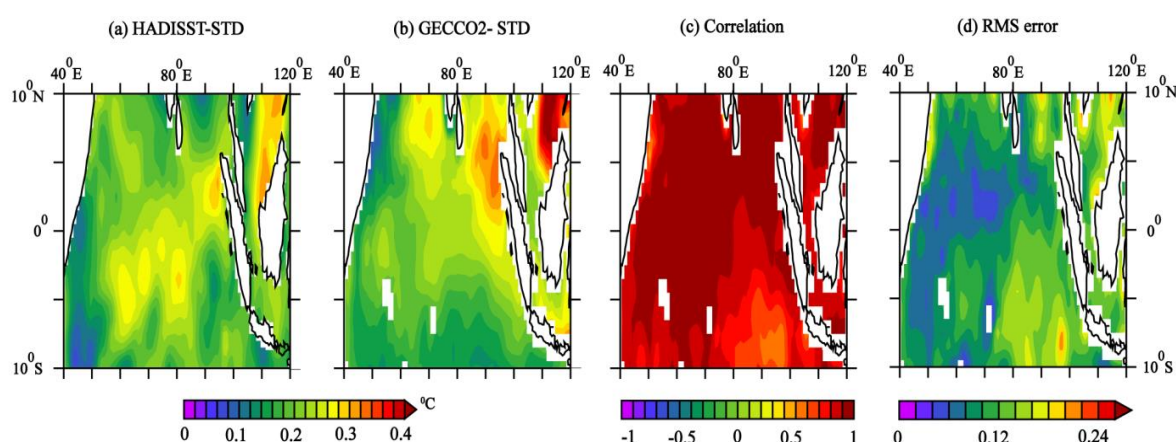


Figure 3.10 Standard deviations from HADISST (a) and GECCO2 (b) data are plotted at the equatorial domain during 1960-2014 periods. Coefficient of correlation (c) and RMS error (d) between model and *in situ* data are plotted during the same period.

GECCO2 model standard deviation was closely following HADISST standard deviation path in the decadal scale except the fact that the low values at the south-eastern Arabian Sea and the Bay of Bengal observed in the HADISST was not replicated by the model. The diagonal patches of higher standard deviation noticed in the HADISST map (Figure 3.10a) was somewhat reproduced in the model with stronger SST variability in the vicinity of northwest Sumatra and the maritime continent (Figure 3.10b). It was interesting to note that the zone of strong SST variability (standard deviation) in the decadal scale shifted to the northern hemisphere in both observation and model (Figure 3.10a&b). The strong coefficient of correlation observed throughout the equatorial domain reemphasized the similarity in the standard deviation maps of observed and model data (Figure 3.10c). The error analysis between the two data sets indicated very less RMS error values in the northern half of the equatorial domain while relatively high

values in the southern half especially the south-eastern region (Figure 3.10d). The relatively less correlation values observed in the south-eastern equatorial domain corroborated with the RMS values. From the above surface temperature validation experiment, it was pretty clear that the GECCO2 values were much closer to the observed values and hence was suitable for analysing the sea surface temperature variability in the decadal scale.

3.4.5 Validation of vertical profiles of temperature from ORAS4 and GECCO2

3.4.5.1 ORAS4 with ARGO data

Vertical temperature profiles from 0m to 300m depth for time period 2002 to 2014 from ARGO data had been used to validate ORAS4 simulation data. As mentioned earlier, four stations (1° S- 62° E; 5° N- 62° E; 7° S- 70° E; 10° S- 100° E) were selected to represent western, central and eastern equatorial Indian Ocean in this validation exercise. Climatological mean was subtracted from monthly fields to generate anomalies to enhance the variability. Normally, the inter-annual variability is limited to 2 to 5 years or 2 to 7 years depending on the length of the time series. Therefore, a 60-month running mean was applied in the present time series to remove the seasonal to inter-annual oscillations and at the same time enhance the decadal signals.

Profiles of coefficient of correlation and the RMS error were plotted in Figure 3.11 to understand the level of acceptance of the model SST at western (1° S; 62° E and 5° N; 62° E), central (7° S; 70° E) and eastern (10° S; 100° S) equatorial Indian Ocean in comparison with the ARGO profiles during the period 2002-2014. There was a substantial decrease in correlation in the subsurface depth between the surface ($R=0.8$) and 80m ($R=0.4$) depth at both 62° E (1° S) and 70° E (7° S) where the lowest value indicated an inverse relationship as high as -0.4 at 50-65m (Figure 3.11 left panel). The RMS error also increased in this depth range with error estimate more or less close to 0.2° C. The decreasing and reversing trend in the coefficient of correlation indicated that the model values were not consistent with the observed data at least at this depth range in the vicinity of the shallow thermocline dome. Beyond that depth the correlation improves and attained the highest value ($R\sim 1$). Since the present study aimed at deriving decadal variability's at the surface and at the depth especially where the equatorial

undercurrent is often detected (80 to 150 m) in the equatorial Indian Ocean as a transient phenomenon, the profiles of correlation and RMS error at surface and at 80-150 m agreed very well with the corresponding Argo profiles at those depth ranges.

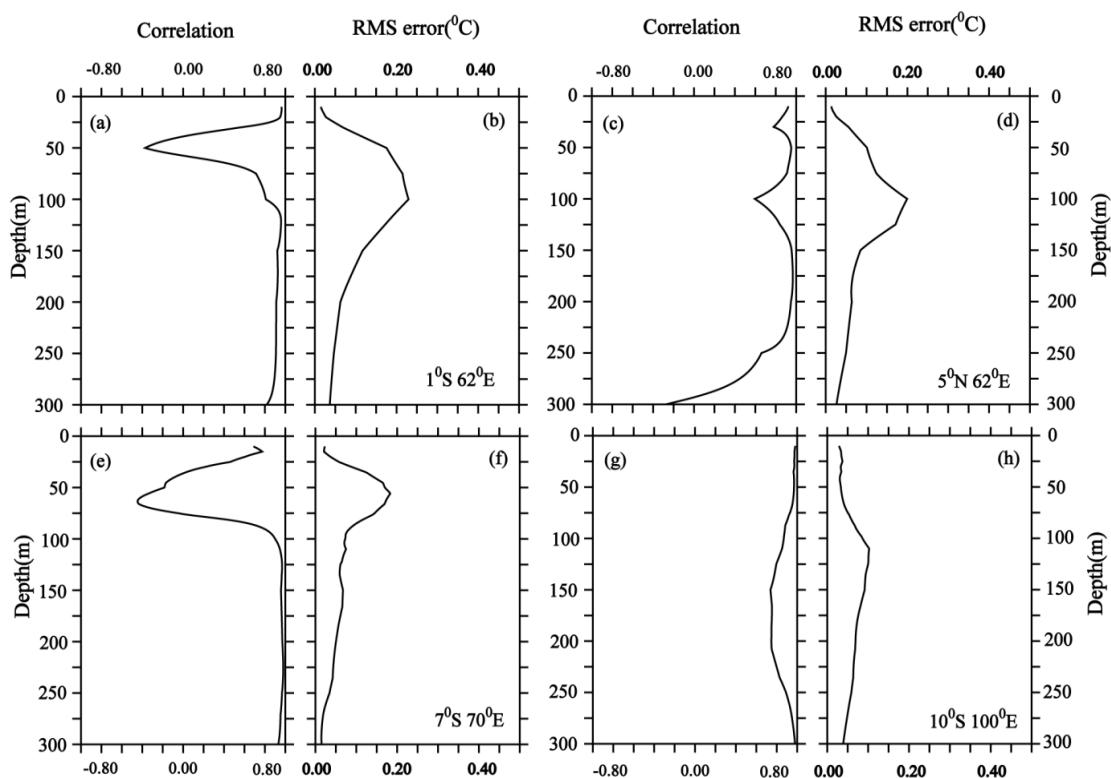


Figure 3.11 Correlation and Root mean square error between ARGO and ORAS4 vertical section of temperature for the period 2002 to 2014 for 1° S- 62° E (a & b), 5° N- 62° E (c & d), 7° S- 70° E (e & f) and 10° S- 100° E (g & h). Monthly temperature anomaly from both data has been subjected to a 60-month running mean smoothing to filter out the seasonal to inter annual oscillations.

Contrary to the above, the validation conducted at north-western and the south-eastern equatorial domain (5° S; 62° E and 10° S; 100° E) invariably indicated better correlation and acceptable RMS error (0.015° C) in the subsurface depths (from 50 to 200 m). The correlation at the surface layer (0-50m) was close to 1 and then dropped to 0.7 in the subsurface depth and remained significant right up to 200m depth thereby establishing the worthiness of the model data to explore the pattern of temperature structure in the decadal time scale. Therefore, it is safe to use the ORAS4 model data with confidence to explore the temperature variability at both the surface (IOD related variability) and at the thermocline depth (EUC related variability) in the decadal time scale.

3.4.5.2 GECCO2 with ARGO data

Validation of GECCO2 simulation data was also attempted by using gridded Argo profiles to examine the authenticity of model data to replace Argo profiles in longer time scales to investigate the variability of subsurface thermal structure in the decadal scale. Similar procedures explained in the previous section were followed in analysing both observational and model data at two designated boxes (7° S; 70° E & 10° S; 100° E) to bring out the decadal variability of temperature in the subsurface layers.

As in the previous case, the correlation between Argo and GECCO2 model temperature profiles deteriorated substantially in the near surface water column (20 to 70 m). However, the correlation remained high and significant ($R=0.8$) at the surface but slightly less compared to the corresponding values of ORAS4-Argo validation results. But the deterioration of correlation noticed at 25 m was not to the extent of exhibiting inverse correlation as observed in ORAS4 validation but remained positive (Figure 3.12a& e) throughout the water column (probably due to the shallow thermocline dome effect¹¹). The mean RMS error between GECCO2 and ARGO (Figure 3.12) observed in the water column was however relatively less compared to the previous *in situ* model data combination (Figure 3.12). However, the validation at 5° N (62° E) and at 10° S (100° E) does not show similar deterioration of correlation in the subsurface, instead indicated significant correlation in the 80 to 150 depth range (Figure 3.12 right panels) with acceptable error estimate. At the surface, at 62° E (5° N) the correlation did indicate a deterioration with minimum RMS error values and the reason for this low correlation values at the surface is yet to be understood.

¹¹ Shallow thermocline dome effect : During boreal winter over southern Indian ocean, northeasterly winds bend northwesterly while crossing the equator southward, and form a weak low-level westerly jet between the equator and 10° S. The cyclonic circulation at the meeting point of these two wind regimes gives an Ekman pumping that is responsible for the formation of the “Seychelles Chagos Thermocline ridge” (SCTR, Hermes and Reason, 2008). Located at 5° S - 10° S band in Indian Ocean, where the thermocline rises close to the surface. This feature is found throughout the year but more pronounced in boreal winter, which is identifiable from the surface wind pattern (McCreary et al., 1993). South of the SCTR, easterly winds drive a southward Ekman transport and north of the SCTR, westerly winds are associated with a northward Ekman transport. The resulting Ekman pumping lifts the thermocline and results in this ridge, extending roughly along the northern edge of the Easterlies (Hermes and Reason, 2008; Yokoi et al., 2008) (Source : TRIO science plan, 2008)

The validation results of both ORAS4 and GECCO2 indicated that the model data are good enough to address the decadal variability at the subsurface depth in the entire equatorial domain of the Indian Ocean. However, both the models failed to predict the subsurface temperature profile in the 20-70m range especially in the shallow thermocline dome in the south-western equatorial zone (7° S; 70° E) in the decadal time scale. The temperature structure predicted by the model at such climate sensitive and dynamic zone could have created the ambiguous values in the decadal time scale. It was therefore decided to investigate the scientific reasoning of this peculiar behaviour of the model at similar hyper dynamic zones in a separate study under future programs. Other than this climate sensitive zone, both the model products appear to corroborate well with the observation and hence user has the option to choose any of

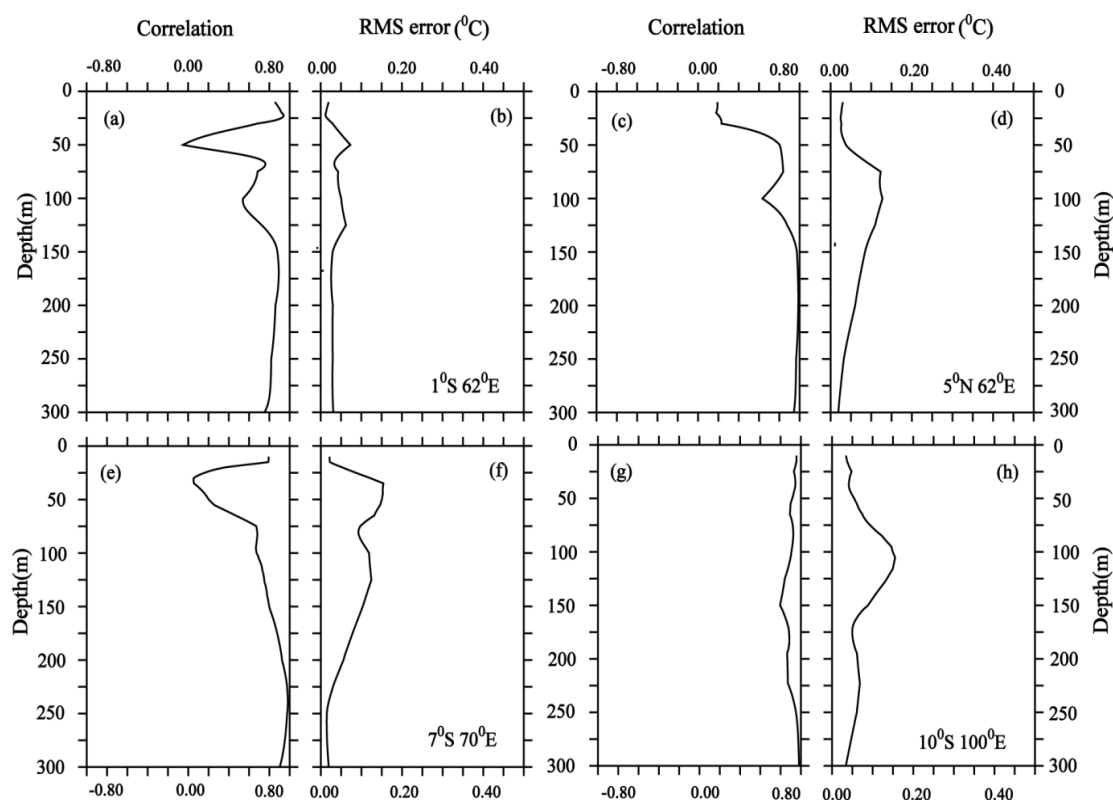


Figure 3.12 Correlation and Root mean square error between ARGO and GECCO2 vertical section of temperature for the period 2002 to 2014 for 1° S- 62° E (a & b), 5° N- 62° E (c & d), 7° S- 70° E (e & f) and 10° S- 100° E (g & h). Monthly temperature anomaly from both data has been subjected to a 60-month running mean smoothing to filter out the seasonal to inter annual oscillations.

these models to address the subsurface processes in the decadal time scale. However, by analysing closely the amplitude of variability's of correlation and error estimate in the surface

300m water column, the GECCO2 had an edge over ORAS4, especially at the 80-150 m depth range, in reproducing temperature values closer to the Argo profiles as the major variability being studied is associated with the transient equatorial under current. If it was read along with the surface standard deviation and correlation maps (Figure 3.12), the GECCO2 simulation will have a better probability in predicting more realistic temperature values at both surface and subsurface levels in the decadal time scale.

3.4.6 Validation of vertical profiles of salinity from ORAS4 and GECCO2

3.4.6.1 ORAS4 with Argo data

The procedures to be followed to prepare the data to analyse the decadal scale variability in the vertical was already explained in the previous section 3.4.5.1. Out of the four locations selected for the validation of model (ORAS4) derived subsurface salinity, at three locations the correlations close to the surface were very high ($R \sim 1$) with Argo values ($1^\circ \text{ S}; 62^\circ \text{ E}$, $5^\circ \text{ N}; 62^\circ \text{ E}$, $10^\circ \text{ S}; 100^\circ \text{ E}$) and for subsurface (80-150m) the correlations were in the range of 0.4 to 0.9 (still significant) at west ($1^\circ \text{ S}; 62^\circ \text{ E}$), central ($7^\circ \text{ S}; 70^\circ \text{ E}$) and east ($10^\circ \text{ S}; 100^\circ \text{ E}$) (Figure 3.13).

The correlations between ORAS4 and Argo profiles in the western longitude (62° E) behave quite differently at 1° S and at 5° N (Figure 3.13 top panels). At south (1° S) the correlation was very high right from the surface to 300m except some weakening at the intermediate depth (80-150m) with low RMS error fluctuating from 0.01 to 0.02 PSU (Figure 3.13a & b). Surprisingly, the correlation profile at north (5° N) decreased from 0.8 at the surface to a negative correlation of -0.4 at 150m depth with corresponding fluctuations in the RMS values (Figure 3.13c & d). But at the central equatorial region ($7^\circ \text{ S}; 70^\circ \text{ E}$) the ORAS4- Argo correlation profile showed an inverse relationship at the surface and it improved with depth to attain the highest correlation of $R > 0.8$ at 50 depth and remains the same throughout the depth (Figure 3.13e). The RMS error profile also fluctuated with the correlation values though the variation was insignificant below 50 m (Figure 3.13f). The abnormal near surface correlation values could be related to the proximity of the climatically sensitive shallow thermocline dome. But the situation changes at the eastern equatorial box where the correlation between the model and Argo derived salinities shot up to the maximum and then decreased gradually to still

significant value 0.4 at 150 m (Figure 3.13g). Correlation deteriorated further to become negative at 180m. The RMS error at the surface appeared to be insignificant as the correlation attained the highest value (Figure 3.13h).

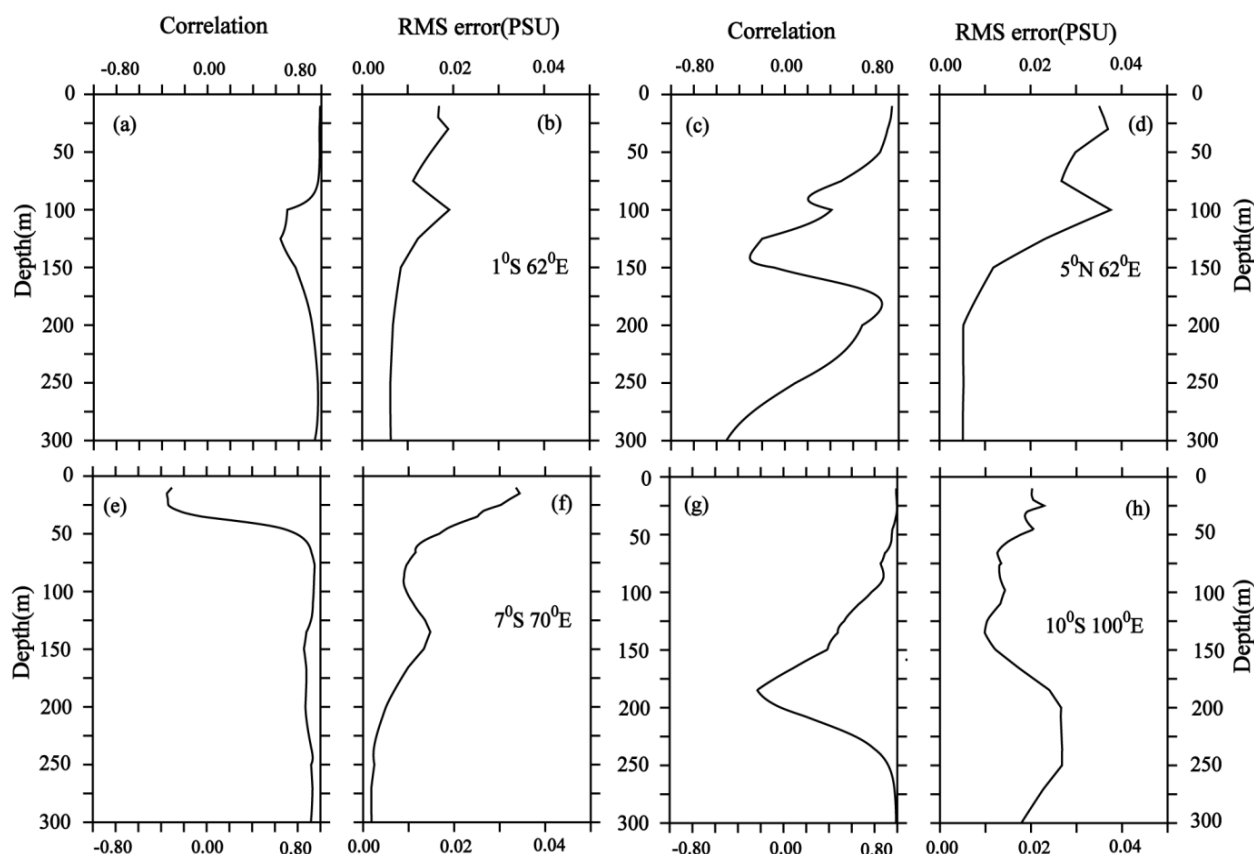


Figure 3.13 Correlation and Root mean square error between ARGO and ORAS4 vertical section of salinity for the period 2002 to 2014 for 1° S-62° E (a & b), 5° N-62° E (c & d), 7° S-70° E (e & f) and 10° S-100° E (g & h). Monthly salinity anomaly from both data has been subjected to a 60-month running mean smoothing to filter out the seasonal to inter annual oscillations.

3.4.6.2 GECCO2 with Argo data

The details of data analysis to bring out the decadal signals were explained in the earlier sections. The influence of climatically sensitive shallow thermocline dome was amply clear in the profiles of the correlation statistics between GECCO2 and Argo. The vertical profiles of coefficient of correlation and RMS error estimate between GECCO2 and Argo at the western equatorial Ocean (1° S; 62° E) resembled the ORAS4-Argo comparison. The correlation seemed to be excellent (above 0.8) between GECCO2 and Argo throughout the water column with

insignificant fluctuations in the error estimate (Figure 3.14a&b). However, the correlation began to degrade from 80 m to zero at 120 m and then further degraded to an inverse correlation close to 150m depth with error estimate fluctuating between 0.01 and 0.02(Figure 3.14c&d). The sharp increase in the negative correlation values at the surface with very high error estimate definitely indicated the model failure in predicting the salinity values (Figure 3.14e&f). The correlation remained to be very poor up to the depth of 100 m and then recover back to significant levels beyond 150m. Conversely, at the south-eastern box the correlation was close to one in the surface 50m layer but deteriorated further to reach to the level of ‘no correlation’ between 100 and 150 (Figure 3.14g). There was a mismatch in the RMS error profile with the correlation curve indicating minimum error coinciding with ambiguous correlation values and vice versa (Figure 3.14h).

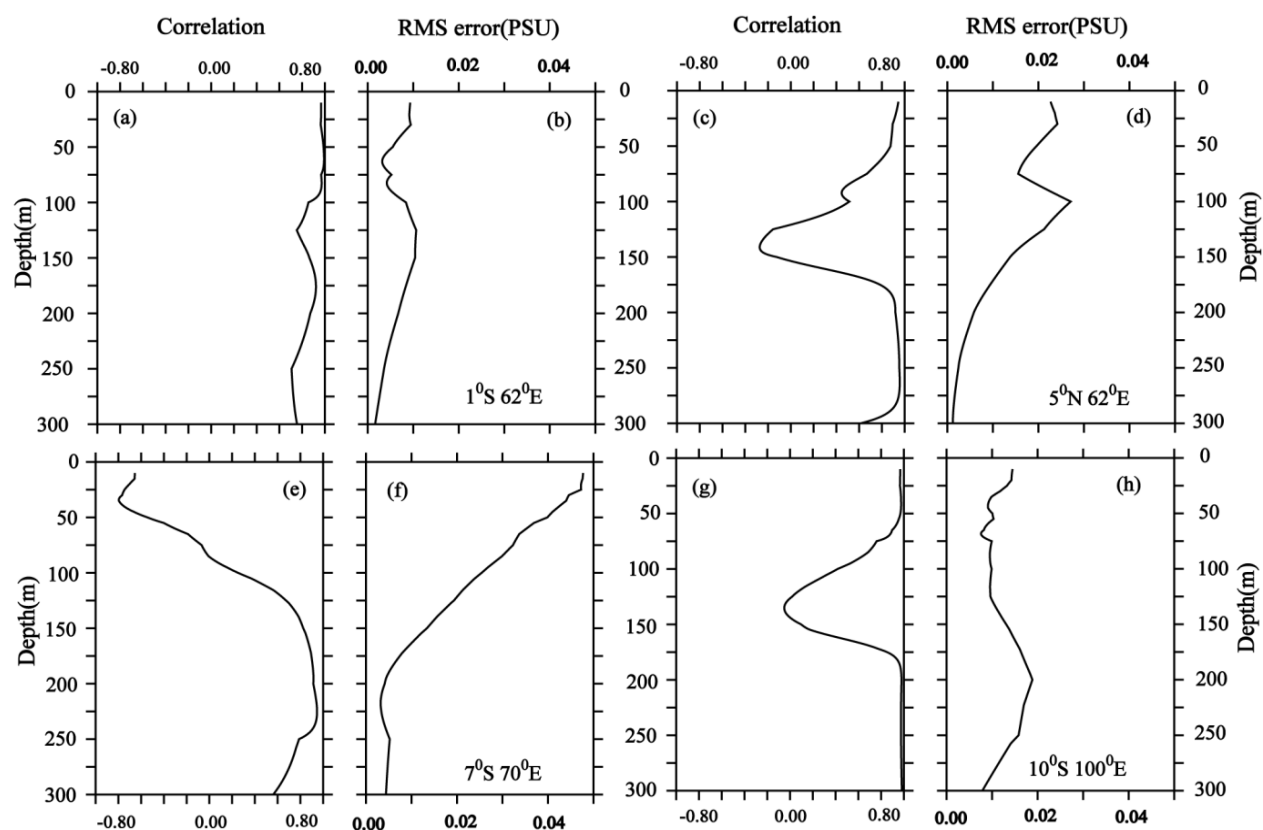


Figure 3.14 Correlation and Root mean square error between ARGO and GECCO2 vertical section of salinity for the period 2002 to 2014 for 1° S-62° E (a & b), 5° N-62° E (c & d), 7° S-70°E (e & f) and 10° S-100° E (g & h). Monthly salinity anomaly from both data has been subjected to a 60-month running mean smoothing to filter out the seasonal to inter annual oscillations.

From the validation exercises, it had been observed that both the models did not produce promising results in predicting the *in situ* values at both surface and subsurface especially at 5° N; 62° E and 7° S; 70° E. However, three out of four cases (locations) the model predictions (both models) were more or less accurate in predicting the surface salinity values. The ORAS4 model predicted quite satisfactorily the subsurface salinity values (80-150m) in three cases out of four while the GECCO2 model could predict only one out of four cases indicating the slight edge of ORAS4 over GECCO2 in predicting subsurface salinity values. Therefore, it can be concluded that the ORAS4 simulation was performing better than GECCO2 simulation in predicting both near surface and subsurface (80-150 m) salinity values in the decadal time scale.

3.5 Limitations in the validation experiment in analysing decadal trends/variability especially at the subsurface depth.

In this section of the thesis, we have made an effort to validate some of the widely used reanalysis/model data products in the decadal time scale by using amalgamated observational data product for surface hydrography and Argo data for vertical profiles to identify the most suitable reanalysis/model data for drawing inferences on the decadal variability/trends of surface and subsurface parameters at the equatorial Indian Ocean bounded by 10° N and 10° S; 40° E and 120° E. Decadal variability of both surface and subsurface hydrographical parameters, derived from two widely used models, have been validated using observed values (Argo data profile) in the equatorial domain (10° N to 10° S and 40° E to 120° E) during a specific common time window. Main challenge here is to identify the closest available Argo profile falls in the model grid as the targeted Argo data profile not necessarily follow a vertical downward path. Therefore, lot of efforts have been put in to identify four matching profiles in the entire equatorial domain to validate these two model products. Two of them falls in the western equatorial region (1° S- 65° E and 5° N- 65° E), one in the central equatorial zone (7° S; 70° E) and the fourth point in eastern equatorial region (10° S; 100° E). But the validation results in the decadal time scale indicated erratic performances of the models at some depths (near surface depths at most of the cases) for both temperature and salinity especially at the south-central equatorial region where a peculiar feature of a shallow thermocline dome persists throughout the year. The erratic performance of the model is consistently observed at these dynamically active regions perhaps due to enhanced air-sea interaction processes. It is surprising that the correlation at these depths decreases to zero

and at times even exhibits negative correlation. Although the longer duration model/reanalysis data has advantages over limited period and region-specific observational data in addressing decadal trends, it lacks accuracy especially in the equatorial domain. The gridded format of the model output at times makes the comparison with *in situ* (also gridded) unrealistic as both the parameters are spatially averaged product. Moreover, the filtering technique further smoothen the variability making the comparison more complicated and hence perform poorly in the validation exercise. The ambiguity observed in the validation results at 20- 80m depths are to be studied in detail with more precise data and hence included the future program.

General description of the inter-annual current variations at the equatorial Indian Ocean

4.1 An Overview

As we have seen in chapter 2, the inter-annual current variability at the equatorial Indian Ocean was largely influenced by the inter-annual climate mode such as ENSO and IOD. El Niño-Southern Oscillation (ENSO) is recognized as a powerful climate phenomenon that impact the global climate in inter-annual time scale ever since the coupled nature of oceanic El Niño and atmospheric Southern Oscillation was established (Bjerknes, 1966, 1969; Neelin et al., 1998). Since then substantial efforts had been employed to understand and predict the occurrence, evolution, physical properties and links to other climate systems (Rasmusson and Carpenter, 1982; Suarez and Schopf, 1988; Webster and Yang, 1992; Ashok et al., 2007; Huang et al., 2017). As the global climate undergoes drastic changes, the response of ENSO and its influence and feedback on the worldwide climate also exhibit significant variabilities (Ashok et al., 2007; Weng et al., 2007; Yuan and Yang, 2012; Yang and Jiang, 2014). The ENSO influenced variabilities over Indian Ocean were statistically valid in explaining several past droughts in India but the relationship appeared to be weakening over the Indian sub-continent in a warming environment. For example, the strong ENSO in 1997 failed to cause drought in India. The investigation on to this abnormal teleconnection led to the discovery of similar seesaw variability of the ocean-atmosphere system in the Indian Ocean in inter-annual time scale which often referred to as Indian Ocean Dipole (Saji et al., 1999; Webster et al., 1999). Since then there had been several studies to understand the influence of these two climate modes on the monsoon rainfall over the Indian sub-continent. In this study we made an attempt to understand the nature of variability these two climate events exert on the equatorial Indian Ocean and delineate their respective role on the equatorial current in the Indian Ocean.

4.2 Brief description of the data and method

The model configuration used in this thesis is an IO sub domain of the global 0.25° resolution (i.e. cell size ~ 25 km) coupled ocean/sea-ice configuration developed as part of the DRAKKAR project (Brodeau et al., 2010) based on NEMO framework. This regional configuration extends from 26.75° E to 142.25° E and from 33.2° S to 30.3° N. The western boundary of the domain is defined by the African continent. The model was forced from 1958 to 2007 with the DFS3 dataset detailed in Brodeau et al. (2010). This model accurately simulates equatorial dynamics and basin wide structures of currents and temperature in the tropics. This model was forced with a similar forcing strategy to successfully reproduce the variability over the Indian Ocean at a wide range of timescales (Akhil et al., 2014, 2016; Vialard et al., 2013). Moreover, our validation studies demonstrated that the model accurately captured the surface and subsurface current variations at both seasonal and inter-annual time scales. A seven-year threshold is used in this thesis for defining the lowest frequency component to address the inter-annual variability. The results are also robust by using a five-year cut-off to define the inter-annual frequency. It has also been found to get robust results by simply computing the inter-annual anomalies by removing the long-term mean seasonal cycle.

4.3 Inter-annual current variability at the Equatorial Indian Ocean

An empirical orthogonal function (EOF) analysis was performed to the data set to draw the general features of the inter-annual variability of both surface and subsurface currents in the IO. The EOF analysis was performed separately for surface currents and subsurface currents in the 10° N to 10° S band at the equator (Figure 4.1 & 4.2 for EOF1 and EOF2, respectively). The first two EOF modes of these surface and subsurface EOF analyses represented 23% and 47% of the variance in the horizontal and vertical fields, respectively. The main characteristics of the principal components (PCs) associated with the EOF analysis was displayed in Figure 4.1 (left panels). One of the striking results was that the principal components of first EOFs of surface and subsurface current anomalies were strongly correlated (0.95; Figure 4.1a), emphasizing that the surface and subsurface current variations denoted by these first EOFs were related to the same mode of current variability. The monthly standard deviation plots (representative of PC1

amplitudes) indicated that this mode of inter-annual zonal current variability was largely representative of the fall season (Figure 4.1b).

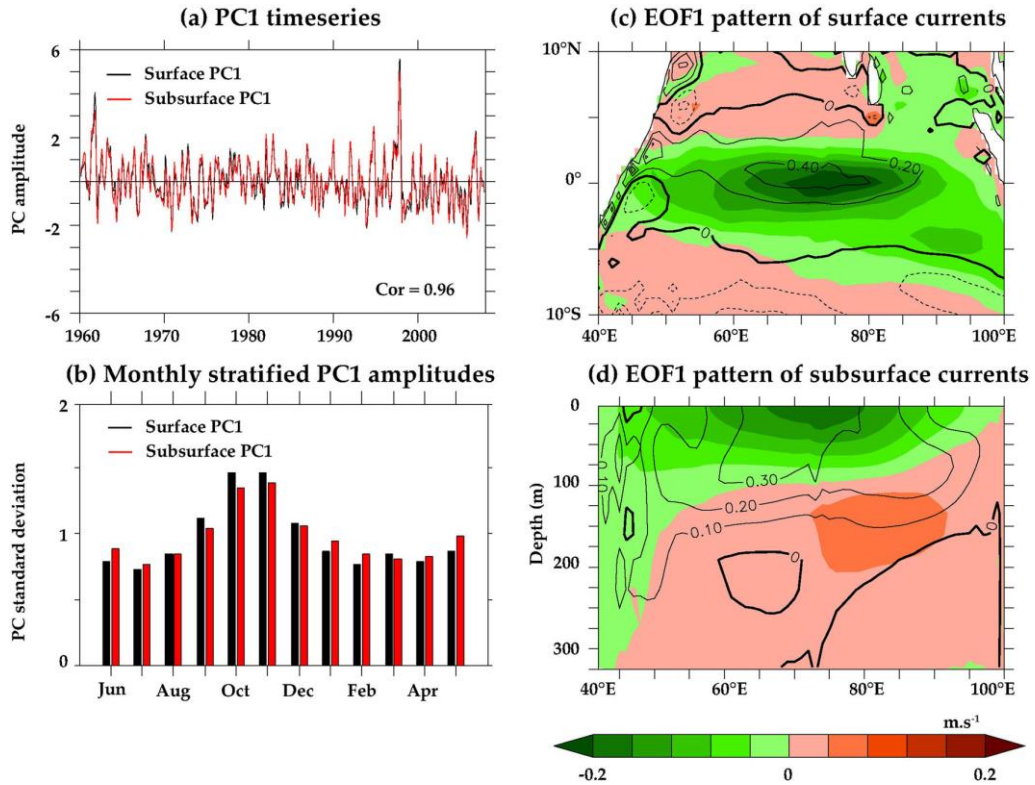


Figure 4.1 (a) Time series (PCs) of surface and subsurface EOFs and (b) monthly standard deviation of normalized principal components of the first EOF of inter-annual surface zonal current anomalies (black) and equatorial vertical section of inter-annual zonal current anomalies (red) from the model over the 1960–2007 period. The correlation between the two principal components is indicated in (a). Corresponding first EOF pattern of (c) surface zonal current anomalies and (d) equatorial vertical sections of zonal current anomalies are in right panel. Climatological fall currents (September–November) are overlaid in (c) and (d).

The principal components of these two EOFs exhibited maximum amplitude in October–November (~ 1.4) and weaker variability in spring (~ 0.7). Recompiling a similar EOF analysis restricted to the fall season indeed resulted in similar EOFs patterns (not shown). The spatial patterns associated with these first EOFs of surface and subsurface currents were displayed in the right panel of Figure 4.1. As depicted by the first EOF of current vertical section, this mode of variability exhibited a current dipole along the vertical at the equator (Figure 4.1d), with a weak anomalous eastward flow located at depth (100–200 m), maximum around 150 m located in the central eastern equatorial IO between longitudes 70° E and 90° E, and a strong anomalous westward flow confined to the first 80 m and maximum between 65° E and 80° E. Similar way,

the first EOF of surface currents showed that the surface anomalous westward flow was maximum at the equator and confined to the narrow meridional band of 3° N - 5° S, with maximum amplitude located right at the equator between 65° E and 85° E (shading Figure 4.1c), coinciding with the location of climatological fall Wyrтки Jet (contours on Figure 4.1c). This mode was hence representing the inter-annual variability of the fall Wyrтки jet and the slight intensification of the associated eastward subsurface currents when the fall Wyrтки jet weakens (contours on Figure 4.1d).

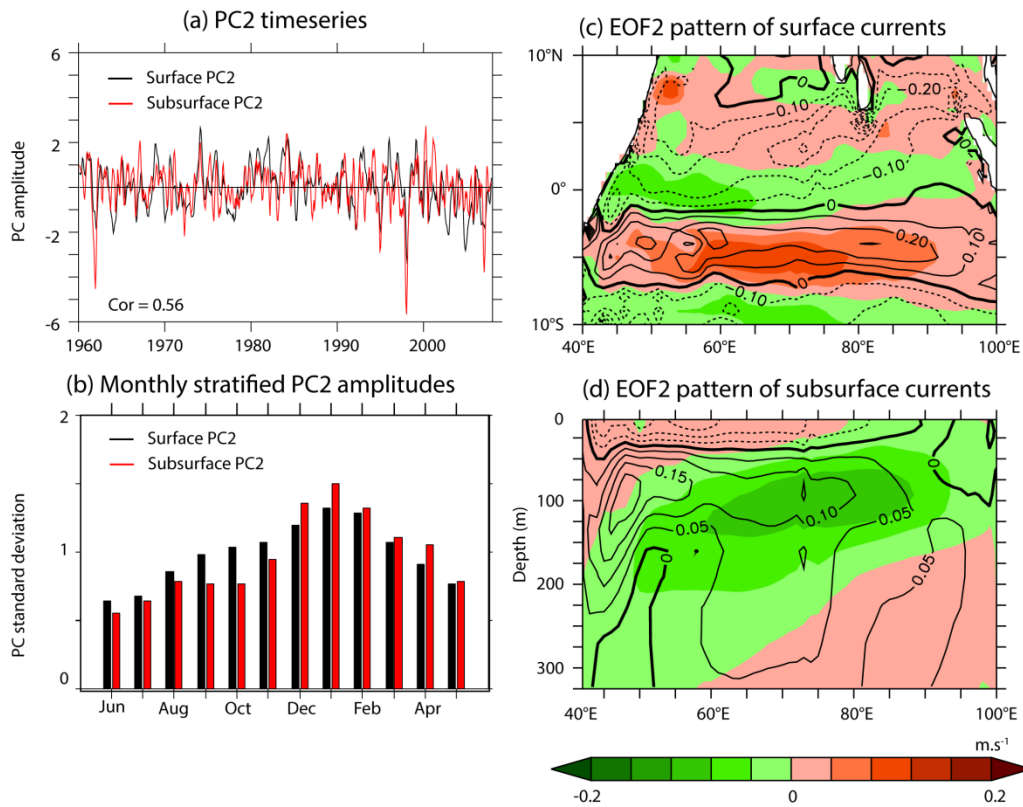


Figure 4.2 (a) Time series (PCs) of surface and subsurface EOFs and (b) monthly standard deviation of normalized principal components of the second EOF of inter-annual surface zonal current anomalies (black) and equatorial vertical section of inter-annual zonal current anomalies (red) from the model over the 1960–2007 period. Corresponding second EOF pattern of (c) surface zonal current anomalies and (d) equatorial vertical sections of zonal current anomalies are in right panel. Climatological winter currents (December–February) are overlaid in (c) and (d).

Figure 4.2 was the replication of same analysis as Figure 4.1 but for the second EOF mode. The closeness factors 7% and 15% for the horizontal and vertical fields respectively indicated the second mode capturing weaker percentage of the inter-annual zonal current

variance. The principal components of the second EOFs of the surface and subsurface currents were related to each other with lesser coefficient of correlation (0.56) compared to the first two EOFs (Figure 4.2a), they also depicted a similar mode of zonal current variations. As explained in Figure 4.2b, this mode of current variability was hugely representative of the inter-annual zonal current during the spring season where their PCs exhibiting a maximum amplitude in December-February (~ 1.3) and far weaker variability's in summer and fall (< 1.0). Associated surface EOF spatial pattern indicated weak zonal current variations at the equator with an anomalous eastward flow largely confined to the western boundary of the basin (Figure 4.2c). Organized large-scale current variations appeared south of 2° S as an anomalous westward flow with a maximum observed between 60° E and 70° E. As these 2nd EOF modes of surface and subsurface currents captured weaker percentage of the inter-annual zonal current variance (7 and 15 % respectively) compared to the first mode, both surface and subsurface patterns exhibited weak current anomalies in the upper ocean but larger variations at depth (Figure 4.2d). The subsurface eastward flow had an up-sloping pattern from the western to the eastern part of the basin, with maximum current located between 150 and 75 m depth. The contours in Figure 4.2d indicated that these subsurface current anomalies occurred at the climatological depth of the winter undercurrent and the pattern was representative of the inter-annual modulation of the intensity of the winter undercurrent.

The lead-lag correlation between the first and second PCs of both surface and sub-surface fields was displayed in Figure 4.3. The first mode of zonal current for both surface (Figure 4.3a) and subsurface sections (Figure 4.3b) led the second mode by 3-4 months with significant correlations of 0.5 and 0.7 respectively. This was a clear indication of the inter-relationship between the Wyrтки jet reduction (EOF1 in Figure 3.2) in fall followed by the winter EUC intensification one season later in winter (EOF2 in Figure 4.2). In order to have a preliminary understanding of wind and climate forcing patterns related to the EOFs of subsurface zonal currents, both SST and surface wind stress anomalies were regressed onto the PCs of first two EOF modes of subsurface zonal currents at the equatorial IO (Figure 4.4a&b).

The first mode represented the fall Wyrтки jet variability and the second mode represented the inter-annual modulation of the intensity of the winter undercurrent. The anomalous near-

equatorial westward surface currents as shown in the first EOF mode of surface current (Figure 4.1c) were appeared to be associated with strong easterly wind anomalies in the equatorial region (Figure 4.4a). In other words, the surface current variations depicted by this mode were a direct response to the equatorial wind forcing. This had been re-established in a lead-lag correlation between the first PCs of surface zonal current and zonal wind stress wherein a maximum correlation of 0.8 has been obtained between the two PCs with currents leading the wind by one month (figures not shown). Similar current reversal earlier than winds had been demonstrated by Nagura and McPhaden (2010a) and explained it as the consequence of reflected Rossby waves radiating from the eastern boundary. It had been highlighted that the sea surface temperature signal associated with these equatorial easterly wind anomalies were characterized by cooling along the west coast of Sumatra and warming in the western IO, indicative of the reminiscence of an IOD signature (Figure 4.4a). Repeating similar regression analysis with the second principal component (PC2) of the subsurface current revealed same SST pattern indicating that the subsurface EOF2 also prescribed the reminiscence of IOD signature (Figure 4.4b) suggesting that the dominant mode of current variations was to some extent driven by the IOD-associated wind forcing.

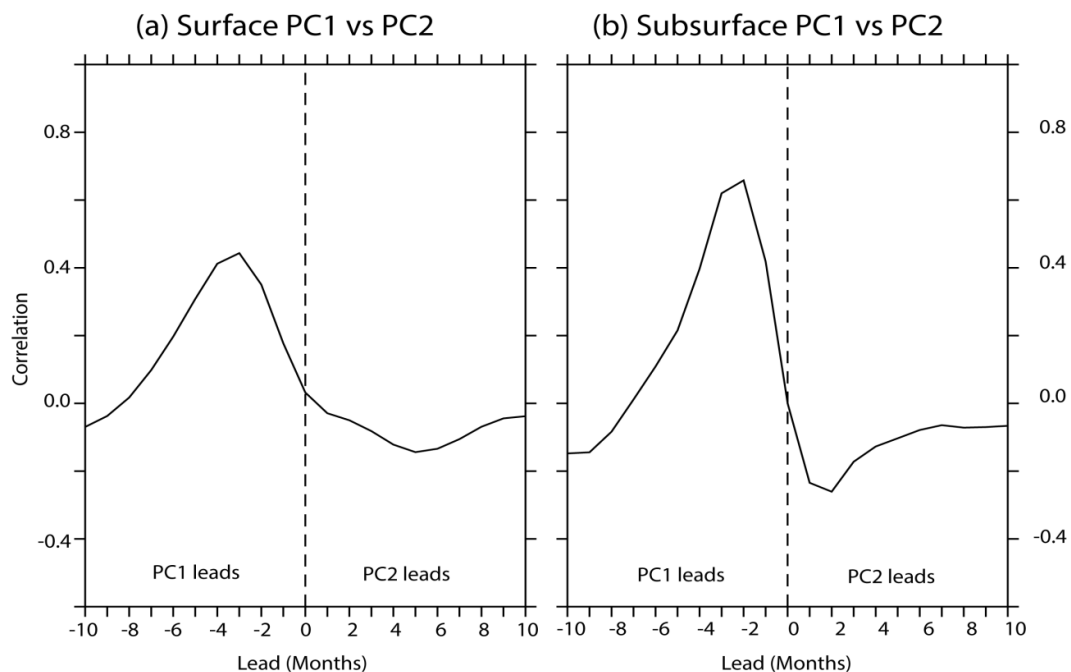


Figure 4.3 Lag correlation of the principal components of EOF1 and EOF2 of (a) surface and (b) equatorial vertical section of inter-annual zonal current anomalies.

A simple lag correlation analysis of the subsurface PC1 and PC2 onto ENSO and IOD indices further established the relationship between these two modes of current variations with these climate modes (Figure 4.4c). The IOD exhibited maximum correlation with PC1 in fall inter-monsoon (~ 0.7). This highlighted the mode of variability peaking in fall exercising strong control on the inter-annual variability of the fall Wyrтки jet. Correlations during preceding summer (~ 0.4) and the following winter (~ -0.4) were also relatively significant indicating the influence of IOD on the equatorial surface current variations during its onset and demise phases. The influence of IOD was evident even in the subsurface current inter-annual variations as depicted in Figure 4.4d. However, compared to its instantaneous control onto surface currents, the response of the subsurface current to IOD was delayed by one season after the IOD peak with a maximum correlation between IOD and PC2 in winter (~ 0.7).

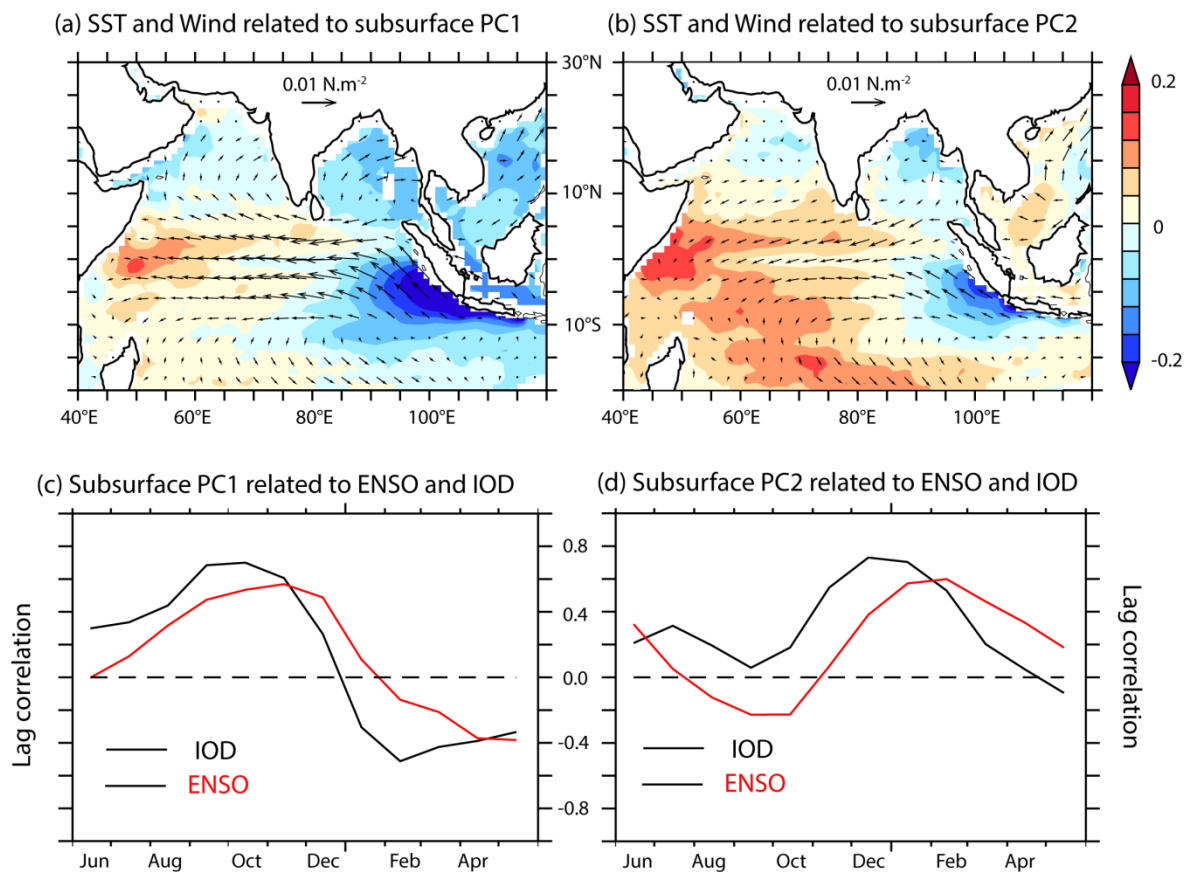


Figure 4.4 Sea surface temperature (shaded) and wind stress anomalies (vectors) regressed onto of the principal components of (a) EOF1 and (b) EOF2 of the equatorial vertical section of inter-annual zonal current anomalies. Simple lag-correlation of (c) PC1 and (d) PC2 of equatorial vertical section of inter-annual zonal current anomalies onto IOD (black lines) and ENSO (red lines) indices over the 1960–2007 periods.

It was also evident that the influence of ENSO on the surface (PC1) and subsurface (PC2) on the surface (PC1) and subsurface (PC2) inter-annual current variability was significant with coefficient of correlation touches 0.6 (Figure 4.4c& d). However, the influence of ENSO onto the surface and subsurface current variability was comparatively weaker (~ 0.6) as compared to IOD but delayed again by one season. Same time the ENSO related influence on the surface currents was maximum in late fall/early winter (Figure 4.4c) and on the subsurface current in late winter/early spring (Figure 4.4d)

Mechanisms responsible for the inter-annual variability of the Indian Ocean equatorial current system.

5.1 An overview of the equatorial dynamics

It had been observed that the role of IOD in modifying the inter-annual variability of subsurface current was indisputably higher compared to ENSO in the equatorial Indian Ocean. It was also a known fact that the mechanisms generating IOD events were not well understood thereby limiting the predicting skills to less accurate numerical models (Luo et al., 2007). But its relevance was all the more important as it had climatic impacts not only limited to the surrounding areas but its influence extended far to East Asia and South America as well (Cai et al., 2011, 2013; Ashok et al., 2001; Behera et al., 2005; Saji and Yamagata, 2003). It was indeed difficult to investigate the inter-annual variability of zonal flow in the equatorial thermocline due to lack of long-term current measurements in the Indian Ocean. Nevertheless, by using limited current time series data during IOD neutral year (2003) and during positive IOD (2006) year, Iskandar et al. (2009) suggested development of stronger thermocline flow during positive IOD event and attributed it to the anomalous equatorial easterlies.

In recent past the equatorial currents and thermocline depth variabilities had been attributed to the dynamics of equatorial waves especially Kelvin and first meridional mode of baroclinic Rossby waves (Zhang et al., 2014). Their results were consistent with the dynamics of these waves that tend to modify the amplitude and periodicity of local thermocline in response to wind forcing. They had evidence to suggest that the zonal flow at the equatorial thermocline was consistently fed by the equator-ward flows of the shallow meridional cross-equatorial overturning circulations of the eastern tropical IO. Similar to the dynamics of coastal and equatorial upwelling (Ekman divergence), the associated wind stress curl modifies the off-equatorial thermocline through Ekman pumping (downwelling). Hence it was suggested that the combined influence of both the equatorial wind and off-equatorial wind stress curl determine the thermocline structure in the eastern equatorial Indian Ocean. Therefore, the westward

propagation of off- equatorial thermocline anomalies were attributed to the dynamics of Rossby wave (Trenary and Han, 2012).

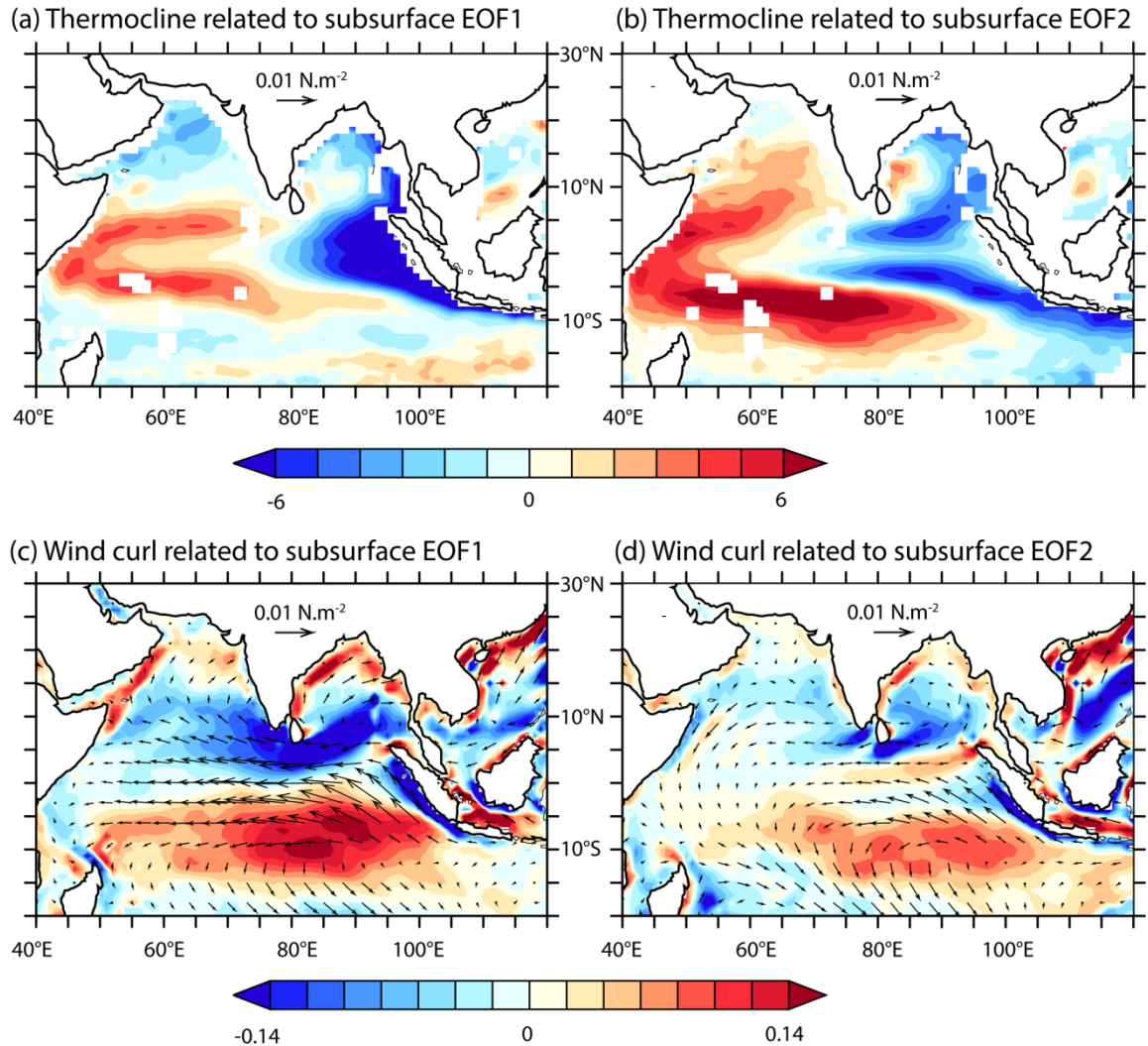


Figure 5.1 20 °C isotherm depth anomalies regressed onto the principal components of (a) EOF1 and (b) EOF2 of inter-annual equatorial subsurface zonal current analysis. Figures (c) and (d) same as (a) and (b) but for wind stress curl (shading) and wind stress (vectors) anomalies.

5.2 Mechanisms responsible for the subsurface current variability.

In order to substantiate the equatorial thermocline dynamics, as suggested by the above authors, the thermocline anomalies (approximated by the 20 °C isotherm) (upper panel), wind stress curl and wind stress vectors (lower panel) were regressed onto the principal components of EOF1 and EOF2 of the inter-annual equatorial subsurface zonal currents were displayed in Figure

5.1. The equatorial thermocline anomalies in both EOFs displayed a zonal dipole pattern, with negative and positive thermocline anomalies in the eastern and western equatorial Indian Ocean respectively (Figure 5.1a& b). The trans-equatorial subsurface thermocline depth variations by means of the thermal dipole drive a zonal pressure gradient along the equatorial region as a direct response to the surface equatorial wind anomalies through equatorial wave propagation. In addition to this zonal equatorial response, the equatorial subsurface current variations in the meridional plane were also associated with strong thermocline anomalies. This is more evident at south of the equator where the thermocline deepening extends from 10° S in the central Indian Ocean towards west. The meridional slopes of the regressed thermocline configuration in both hemispheres were consistent with the signatures of westward propagating Rossby waves (Rao and Behera, 2005; Yu et al., 2005), with wave signals propagating slower as it moves away from the equator. As explained earlier by Zhang et al. 2014, the meridional structure of deeper thermocline in the west and shallower thermocline in the east drives a converging geostrophic flow towards the equator which was often considered as a limb of shallow meridional overturning cell feeding the zonal flow along the equator. This often contributed to the equatorial zonal current variability at depth.

Wind stress (vector) and wind stress curl (shade) regressed onto the first two PCs of the vertical EOFs in Figure 5.1c, d displayed patterns more or less similar to the thermocline. The strong off-equatorial wind stress curl signals ($\sim 10^{\circ}$ S) appeared to contribute to the thermocline deepening signals through Ekman pumping. Our results were in agreement with the views of Zhang et al. (2014). They were of the opinion that the inter-annual variability of zonal currents within the equatorial thermocline was driven by the cross equatorial thermocline slope maintained by both equatorial wind anomalies and off-equatorial wind stress curl anomalies and fed by shallow meridional overturning cells supported by the off-equatorial thermocline patterns. The thermocline and wind patterns in Figure 5.1 showed the reminiscent of signature of both IOD and ENSO (Yu et al., 2005).

To put in nutshell, the analyses in this section demonstrated that the inter-annual variability of the equatorial currents in the Indian Ocean was described by two modes. The first mode represented the maximum variability in fall and was explained by the reduction of the fall

Wyrтки jet associated with intensification at deeper level. Similarly, an intensification of fall Wyrтки jet at the surface was associated with a reduction of strength at depth. The second mode appeared to be peaking in winter and largely explained the inter-annual variability of the winter EUC with a weaker surface expression. These two modes could be explained by a combination of both equatorial and off-equatorial wind variations. It had been shown that the second mode tend to lag the first by 4-5 months. These two modes were related to the combined influence of co-occurring ENSO and IOD events. However, as already acknowledged in the literature (e.g. Annamalai et al., 2003; Izumo et al., 2013), IOD and ENSO events showed a strong tendency to co-occur, the ENSO and IOD indices examined here indeed exhibiting a 0.65 correlation. This co-variability did not allow at this stage to disentangle the respective influence of IOD and ENSO on the variations of the equatorial current system. This was the objective of the following section.

5.3 Respective influence of IOD and ENSO on equatorial current variations.

Before attempting to separate out the influence of IOD and ENSO on equatorial current inter-annual variations, first summarize the simple regression analysis of the inter-annual variability of equatorial currents and zonal winds in the central equatorial Indian Ocean between 65° E and 85° E onto ENSO and IOD indices where maximum current variations were seen for both EOF analysis (Figure 4.1 & 4.2). As expected from the tendency from ENSO and IOD events to co-occur, this simple regression displayed similar regression currents and wind patterns onto these two indices (compare left and right panels of Figure 5.2). Against the climatological trend seen in the overlaid positive surface current contours (indicating eastward current), the combined influence of these two modes resulted from a strong westward current anomaly in the surface layers during the fall season indicating reduction of fall Wyrтки jet followed by an increase in eastward current in the subsurface depth from September to March with maximum seen in December (Figure 5.2a&c). It was interesting to note the early stages of subsurface intensification of the late summer/early fall EUC that appeared to coincide with the diminishing stages of the climatological undercurrent. The maximum intensification of EUC in December occurs when the climatological current reached to a point of disappearance (see shaded currents and overlaid climatological current contours in Figure 5.2a&c). It was evident from both panels (Figure

5.2b&d) that the co-occurrence of IOD and ENSO were associated with an easterly wind anomaly from August to February that caused the reduction of fall Wyrтки jet and intensification of subsurface current 2 months later. That is the time it takes for the zonal pressure gradient to equilibrate to the wind forcing through equatorial wave propagation (Chen et al., 2015).

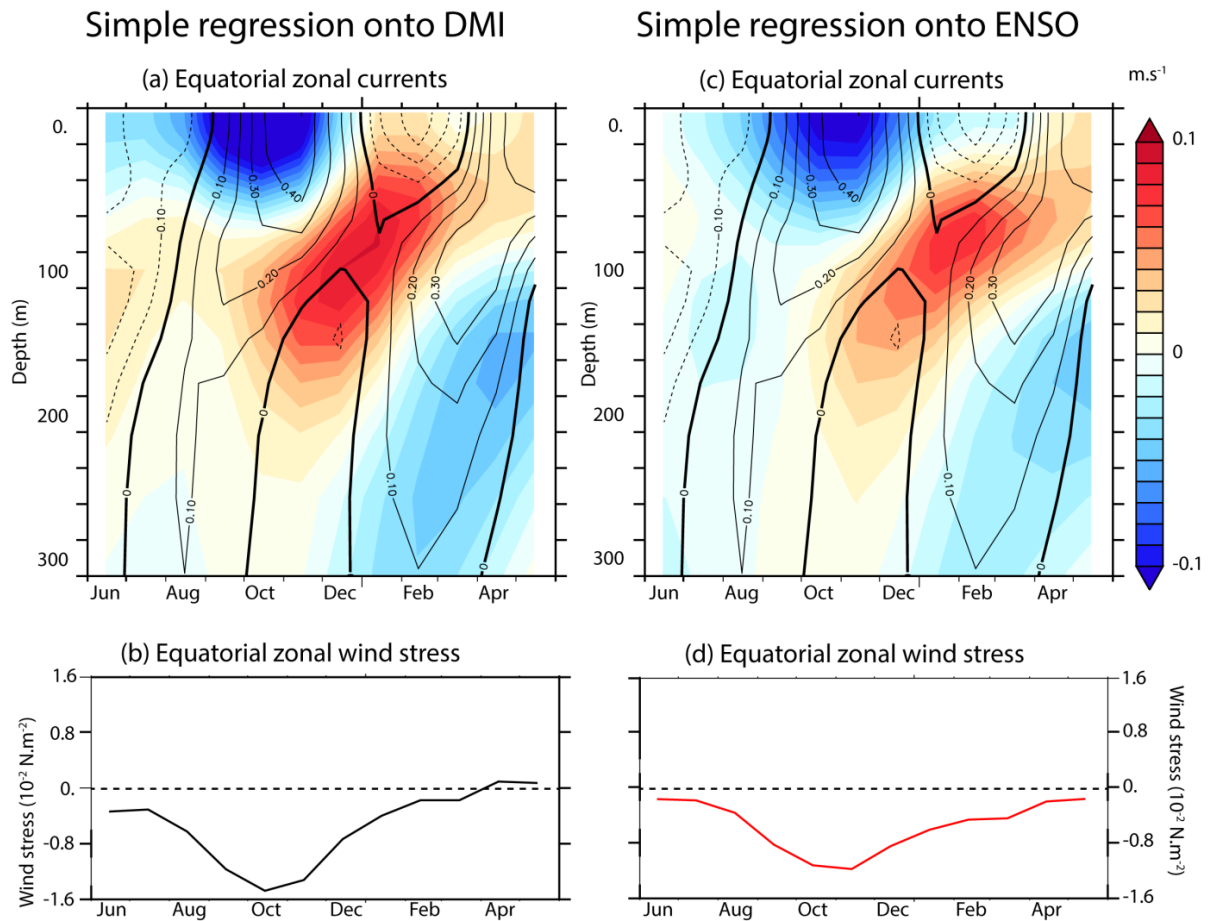


Figure 5.2 (a)–(d) Simple regression of (top) vertical section of zonal currents and (bottom) equatorial zonal winds averaged over the [2°N–2° S; 65° E– 85° E] region onto (left) DMI index and (right) ENSO index over the 1960–2007 period. Corresponding vertical sections of climatological zonal currents are overlaid in (a) and (c).

First, we separated out the influence of ENSO and IOD from the forcing parameters like wind and thermocline to understand the dynamics that might in turn tend to influence the current structure. Figure 5.3 separated out the respective control of IOD and ENSO onto the wind and thermocline inter-annual variability in fall, winter and spring by performing a partial regression analysis to extract the influence of IOD- independent ENSO and the influence of ENSO- independent IOD.

During boreal fall, maximum wind response to positive IOD events occurred and was characterized by strong easterly anomalies in the equatorial region. A positive wind stress curl signal was also observed in the south eastern IO centered around 8° S (Figure 5.3a). The thermocline shoaling in the eastern equatorial IO in fall driven by the prevailing equatorial easterlies through the generation of an equatorial upwelling Kelvin wave that reflected into a westward propagating upwelling Rossby wave, as illustrated by the two negative thermocline

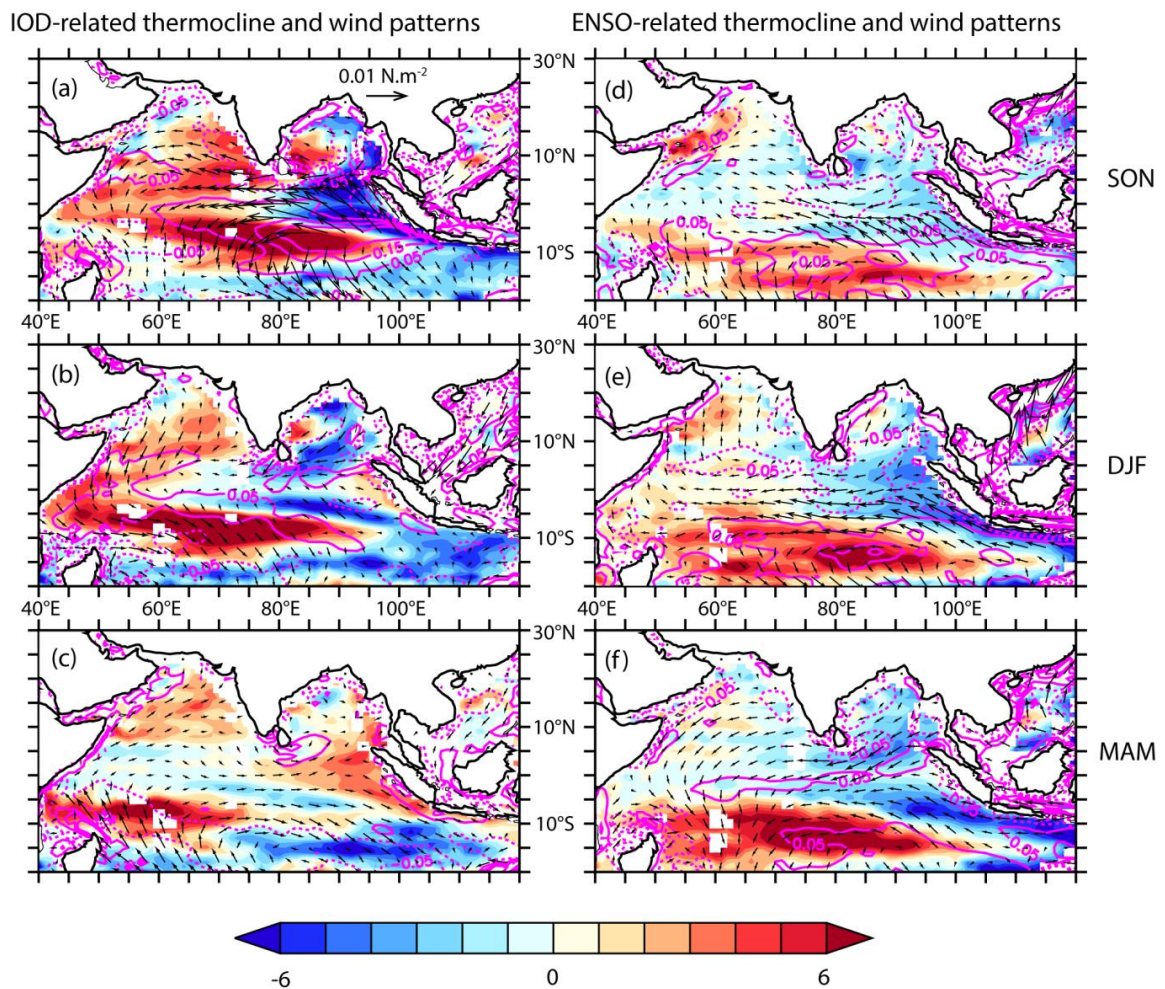


Figure 5.3 a–f Partial regression of 20 °C isotherm depth anomalies (colour), wind stress curl (contour) and wind stress (vector) onto (left) DMI index with the influence of ENSO index removed and (right) ENSO index with the influence of the DMI index removed over the 1960–2007 period for (top) fall (SON), (middle) winter (DJF) and (bottom) spring (MAM). Wind curl contour are in 10^{-7} N m^{-3} .

anomalies on either side of the equator in the eastern IO (Figure 5.3a). The strong positive wind stress curl signal in the south-central Indian Ocean drives off-equatorial convergence due to

Ekman pumping, resulting in deeper than normal thermocline in the central Indian Ocean in fall. The wind signals weaken considerably after the demise of IOD (Figure 5.3b&c). However, the off-equatorial positive thermocline anomalies exhibited westward propagating signal maximum roughly along 8° S in the southern IO from fall until the following spring (Figure 5.3a-c) as a result of westward Rossby wave propagation. These positive thermocline anomalies reach the western boundary in late winter.

The wind and thermocline patterns during an IOD independent ENSO event differ much from that of IOD related patterns (Figure 5.3d- f). It was evident that the IOD related wind signals dissipated during winter when ENSO wind signal gathered maximum strength in winter one season after the mature phase of IOD (Klein et al., 1999; Xie et al., 2009). Similar to IOD, ENSO drives anomalous equatorial easterly winds that persist from fall to spring but with weaker amplitude than that of the IOD. In response to these easterly wind anomalies the thermocline shoals at the eastern equatorial IO during winter (Figure 5.3e) while deepening of thermocline developed in the southern IO in response to Ekman pumping signal peaking in winter. These positive (deep) thermocline anomalies propagated westward during spring season (Figure 5.3f) in consistent with Rossby wave signal. But the propagation was weaker (as it moves away from the equator) and cantered further south (around 12° S) compared to corresponding IOD signals, consistent with the findings of Rao and Behera (2005) and Yu et al. (2005). These signals hardly reach the western boundary towards the end of spring due to their slower propagation speed (Figure 5.3f). The present study hence revealed a weaker and delayed influence of ENSO on tropical thermocline variations compared to that of IOD.

As we have already analyzed the influence of ENSO- independent IOD and IOD- independent ENSO on the thermocline and wind structure (Figure 5.3), the same technique had been employed to separate out the respective influence of ENSO and IOD on the equatorial current system by displaying Figure 5.4a& d an analysis similar to Figure 5.2a& c but performing partial regression analysis to extract the influence of IOD- independent ENSO and the influence of ENSO- independent IOD. This analysis provided a clear picture of the respective influence of these two modes on the equatorial current system. Figure 5.4a indicated that IOD events were responsible for the surface Wyrтки jet reduction in fall along with the subsurface zonal current

intensification from June to December. These zonal current signals associated with the IOD were consistent with the IOD- related equatorial wind forcing independent of ENSO (Figure 5.4b).

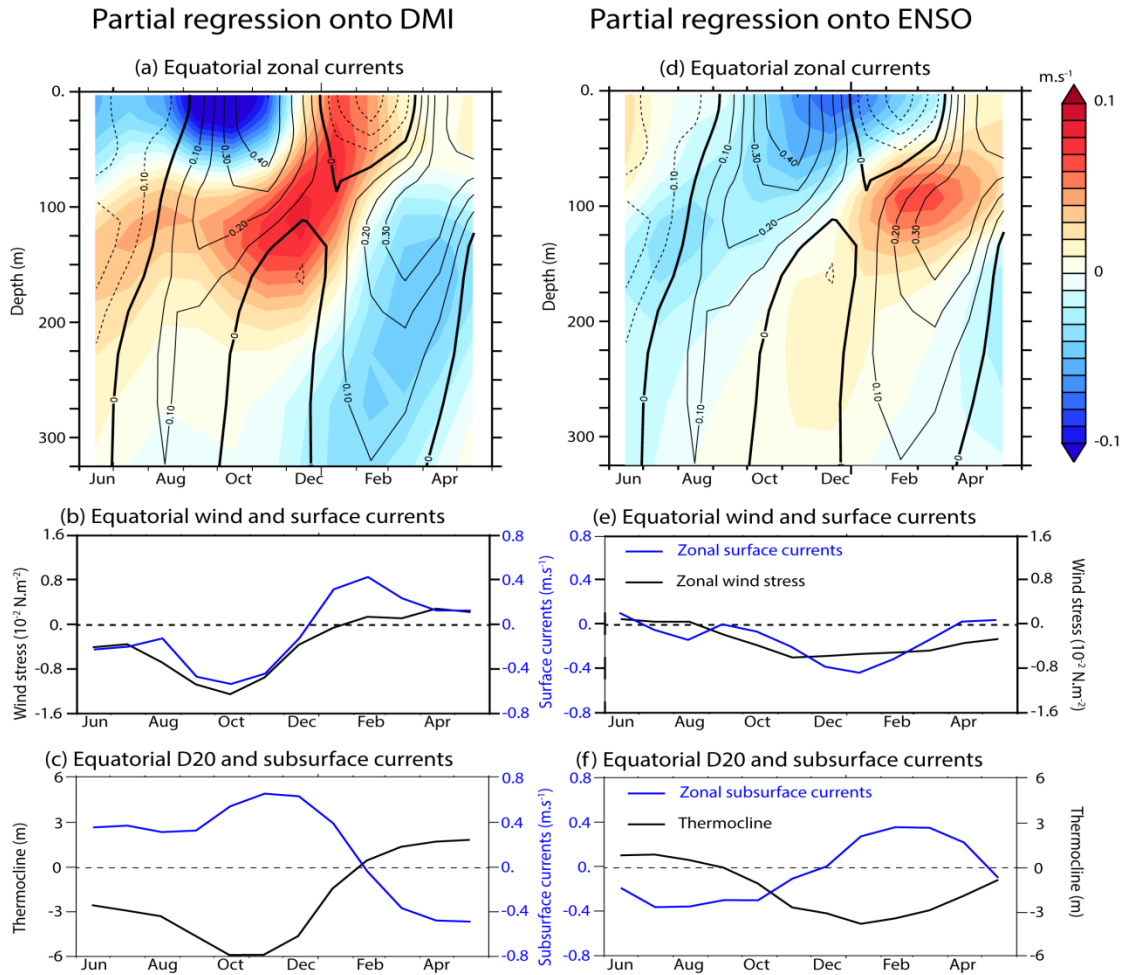


Figure 5.4 (a)– (f) Partial regression of (top) vertical section of zonal currents, (middle) equatorial zonal winds (black) and zonal surface currents averaged over the [2° N–2° S; 65° E–85° E] region (blue), (bottom) zonal subsurface currents averaged over the [2° N–2° S; 65° E–85° E; 80–180 m] region (blue) and equatorial thermocline averaged over the [5° N–5° S; 80° E–100° E] region (black) onto (left) DMI index with the influence of ENSO index removed and (right) ENSO index with the influence of the DMI index removed over the 1960–2007 period. Corresponding vertical sections of climatological zonal currents are overlaid in (a) and (d).

As already discussed from Figure 5.3a– c and consistently with the IOD tendency to peak in fall, maximum equatorial easterly anomalies associated with the IOD were found to occur during that season. As clearly shown on Figure 5.4b, these easterly wind anomalies were in phase and directly force the fall Wyrтки jet reduction in fall. These easterly wind anomalies also induced

maximum shoaling of the eastern equatorial thermocline in late fall, with a 1-month delay typical of Kelvin wave propagation (Figure 5.4c). The subsurface current variations largely mirror the thermocline anomalies, as a direct response to the related change in zonal pressure gradient (Figure 5.4c). Indeed, the thermocline shoaling in late fall resulted in an eastward subsurface current anomalies maximum at ~120 m depth (Figure 5.4a), maximum 1 month after the maximum thermocline deepening (Figure 5.4c). As a result, and in line with Chen et al. (2015), this analysis therefore, revealed that the maximum subsurface current intensification occurred 2 months after the maximum surface easterly wind signal.

The thermocline deepening and related westward subsurface current anomalies from February onwards (Figure 5.4c) were likely to be the result of a down welling Kelvin wave resulting from the western boundary reflection of the off equatorial Rossby waves south of the equator in winter discussed on Figure 5.3a– c, rather than a direct response to the equatorial wind forcing which was weak after the IOD demise (Figure 5.4b). Finally, the eastward surface current anomalies in January after the IOD demise (Figure 5.4a,b) were likely to result from the combined effect of the eastward subsurface current in early winter and reflected Rossby wave signal at the eastern boundary, rather than a direct response to the surface wind forcing (Figure 5.4b).

As already suggested from Figure 4.4c, d, Figure 5.4d revealed that the impact of ENSO on the equatorial currents was delayed compared to that of the IOD. ENSO related zonal current signature was weak in fall. ENSO signature initiates in winter as a westward surface current anomaly maximum in December that tends to accelerate the demise of the fall Wyrtki jet. ENSO was also responsible for the subsurface current intensification located around 100 m depth 2 to 3 months later (i.e. from January to April). This intensification occurred at the time of the winter EUC (see climatological currents overlaid as contours on Figure 5.3b, d), indicating that ENSO forcing acted to intensify the winter EUC. Once again, these ENSO-related zonal current signatures were consistent with the surface wind forcing induced by the remote influence of ENSO. In line with analysis performed in Figure 5.3, Figure 5.4e demonstrated that the maximum surface wind signature of ENSO on the IO occurs later than that of the IOD (Figure 5.4b), with maximum equatorial easterly wind anomalies spanning from November to March.

The maximum amplitude of these anomalies was twice weaker than that of the IOD but last longer. This delayed ENSO signature over the IO extending after the peak of ENSO (i.e. in November) had already been documented and attributed to local air–sea interactions over the Indian Ocean (e.g. Xie et al., 2009). These wind anomalies directly force the westward surface current anomalies seen from November to March (Figure 5.4e). These ENSO- related easterly wind anomalies also induced maximum shoaling of the eastern equatorial thermocline in winter, which drove the EUC intensification in late winter/early spring (Figure 5.4f) as a direct response to the related change in zonal pressure gradient. Finally, as compared to those related to the IOD, the off-equatorial Rossby wave signals south of the equator related to ENSO (see Figure 5.3) were unlikely to play a role on the equatorial thermocline and related subsurface current variations in winter and spring because they were generated at higher latitudes (12° S compared to 8° S in the case of IOD) and hence exhibited a weaker propagation speed that did not allow them to reach the western boundary until late spring.

This section hence demonstrated that the first mode of current variability depicted by EOF1 (see Figure 4.1) was largely driven by IOD wind variations rather than ENSO. Indeed, PC1 averaged in fall exhibited a strong correlation with the IOD index for both surface and vertical currents, while the correlations of PC1 with ENSO index were weaker (Figure 4.4c, d). Similarly, the strong subsurface current intensification in winter depicted by EOF2 was more controlled by the IOD, although ENSO also significantly contributed to this variability. While ENSO had undoubtedly a weaker and delayed influence on the equatorial current system as compared to the IOD, ENSO forcing drives the inter-annual variability of the winter EUC more than the IOD because of its delayed influence on the inter-annual wind variability as compared to IOD (Figure 5.3 and 5.4).

Changes in inter-annual variability of temperature at the equatorial Indian Ocean in different epochs

6.1 An overview

Earlier studies have shown that El Niño-Southern Oscillation (ENSO) are the dominant mode in tropical climate variability exerting great influence on climate system around the globe. The fluctuations in precipitation and associated heat flux release during ENSO affect the global atmospheric circulation through wave dynamics (Hoskins and Karoly, 1981; Shukla and Wallace, 1983; Sardesmukh and Hoskins, 1985; Trenberth et al., 1998; Su et al., 2001). Compared to large changes in sea surface temperature (SST) in equatorial Pacific Ocean during ENSO, the inter-annual SST anomalies in the Indian Ocean are modest. This inter-annual SST variability in the Indian Ocean is mainly influenced by El Niño, along with atmospheric teleconnections associated with Southern Oscillation (Bjerknes, 1969). There have been several studies comparing SSTs of Atlantic and Indian Ocean with that of Pacific Ocean at various geographic locations and reported a lag in SST between Pacific and other two major Ocean such as Atlantic and Indian Ocean. This suggested that the warming seen in other Oceans remote to Pacific is related to forcing from Pacific. As the Atlantic and Indian Ocean does not have any direct connection with the Pacific, the remote access might probably be due to the atmospheric bridge mechanism proposed by Lao and Nath (1996). The atmospheric circulations from tropical Pacific remotely influence the SSTs of other two tropical Oceans through an atmospheric bridge. There were warming events occurring at the Pacific Ocean and similar warming episodes were evident in Indian Ocean also (Chambers et al., 1999).

The first mode of inter-annual Tropical Indian Ocean variability was associated with the Indian Ocean Basin Mode (IOBM) as described by Klein et al. (1999), Guo et al. (2018) and Sun et al. (2019), while the second mode was that of IOD (Saji et al., 1999; Saji& Yamagata, 2003; Webster et al., 1999). The IOBM is a mode of basin scale warming/cooling in the Tropical Indian

Ocean associated with ENSO which often occur during spring and summer following a winter El Niño. This basin scale warming of Tropical Indian Ocean had important influence on the summer climate over Asia.

6.2 Climate Shift Era

The North Pacific regions experienced a dramatic shift in the climate in 1976 that exhibited anomalous increase in winter and spring temperatures and at the same time showed a decelerated summer and autumn temperatures when compared to the previous twenty-five years. The persistence of such anomalous conditions was studied by Trenberth (1990) and their oceanic and atmospheric dynamics were studied in detail by Miller et al. (1994). This warming had far long implications on global climate system. Since such observations, the period between 1976 and 1977 is known as climate shift period. As the climate shift originated at the tropical Pacific, many characteristics of El Niño changed (Nitta and Yamada, 1989), including the frequency, intensity and propagation direction (Wang, 1995; Wallace et al., 1998; Kinter et al., 2002, 2004). El Niño events become stronger after the climate shift era (1976 to 1977). Also, after 1980's, the ENSO period has been increased to about 4/5 year. Relationship between ENSO and Indian Ocean Dipole (IOD) was also changed after the climate shift. Another striking difference between the two epochs is only few positive IOD events are co-occurred with ENSO before the climate shift. But after the climate shift the number of co-occurring events increased along with the intensity of the events.

6.3 Brief description of Data and Methodology

NEMO (Nucleus for European Modelling of the Ocean) model surface temperature from 1960-2007 has been used to study epochal evolution of inter-annual temperature at equatorial Indian Ocean (a more detailed description about the model, forcing mechanism can be seen in chapter 2). An attempt has been made here to study the features of inter-annual time scale variability of temperature over equatorial Indian Ocean in pre- and post- climate shift era. The temperature from this model with similar forcing strategy has been validated from intra- seasonal to inter-annual time scales over the Indian Ocean by Keerthi et al. (2013, 2016).

Inter-annual temperature signals have been calculated by removing monthly climatology. A three-month running mean was then applied to filter out the seasonal oscillations. In order to study the variability of temperature related to climate shift of 1976-1977, the filtered temperature anomalies were divided into two time period groups called as epochs, from 1960 to 1976 and from 1977 to 2007 respectively. Here after, 1960- 76 period is called PRE76 and 1977- 07 is called POST76. Our aim was to assess the relationship between Indian Ocean equatorial temperature and climate modes in the Indian Ocean i.e. the Indian Ocean Dipole (IOD) and El Niño-Southern Oscillation (ENSO) in both epochs. Standard indices have been used to characterize these modes. ENSO is measured as the mean sea surface temperature over the region called Niño3.4 (120° W – 170° W; 5° N – 5° S) over the period December – February. The Indian Ocean Dipole was measured by an index called Dipole Mode Index (DMI) (Saji et al., 1999), which is the difference between the inter-annual sea surface temperature anomalies over the south-eastern equatorial Indian Ocean (50° E-70° E; 10° N – 10° S) and Western equatorial Indian Ocean (90° E – 110° E; 10° S – 0°), averaged over the September- November season. These two indices have been calculated using monthly HADISST dataset (Rayner et al., 2003).

IOD and ENSO were strongly correlated each other during the second epoch (post 1977). So, it was often very difficult to separate out their respective influence using simple linear regression. Hence partial correlation analysis (Yule and Kendall, 1950; Panofsky and Brier, 1958) had been used in such cases. Partial correlation was often explained as finding the correlation between two variables while controlling for the cross correlation between independent variables. This analysis had been used for separating the individual influence of IOD and ENSO in the recent studies (Saji and Yamagata, 2003; Yu et al., 2005; Gnanaseelan et al., 2012). Partial correlation is computed as

$$r_{xy.z} = \frac{r_{xz} - r_{xz} \cdot r_{yz}}{\sqrt{(1 - r_{xz}^2) \cdot (1 - r_{yz}^2)}}$$

For example, if one wants to compute the partial correlation between surface temperature and Indian Ocean Dipole, then

$$r_{\text{temp,dmi.nino}} = \frac{r_{\text{temp,dmi}} - r_{\text{temp,nino}} \cdot r_{\text{dmi,nino}}}{\sqrt{(1 - r_{\text{temp,nino}}^2) \cdot (1 - r_{\text{dmi,nino}}^2)}}$$

Where $r_{\text{temp,dmi.nino}}$ is the partial correlation between surface temperature and IOD with ENSO effect is isolated, $r_{\text{temp,dmi}}$ is the correlation between surface temperature and IOD index, $r_{\text{temp,nino}}$ is the correlation between surface temperature and ENSO index and $r_{\text{dmi,nino}}$ is the correlation between IOD and ENSO index.

In order to compare the correlation between climate modes and equatorial Indian Ocean temperature on both epochs, a new statistical test was used, known as Fisher's r to z transformation. Comparison of correlation values between two groups of data could be done only if the correlations were conducted on same variable with different sample sizes and if both correlations were statistically significant. The way to do is this by using Fisher's r to z transformation. The first step in this analysis was finding the correlation value r between the samples (negative signs are ignored). Then note down the sample size of the two groups. Now determine the Z scores (Z score is the measure of number of standard deviations below or above the population mean) corresponding to the r values. Then determine the observed Z score by the formula

$$Z_{\text{observed}} = \frac{Z_1 - Z_2}{\sqrt{[\left(\frac{1}{N_1} - 3\right) + \left(\frac{1}{N_2} - 3\right)]}}$$

Once the observed Z value has been determined, statistical significance can be assessed by checking to see if the observed value was greater than the critical value.

In this study, a widely accepted online statistics analysis tool, 'Free Statistics Calculators (version 4.0)' [<https://danielsoper.com/statcalc>] has been used for performing Fisher's r to z

transformation to compare the correlation values between the parameters in PRE76 and POST76 period.

6.4 Main patterns of Inter-annual temperature variations on PRE76 and POST76 epochs

The first mode of sea surface temperature and subsurface temperature for the tropical Indian Ocean variability for the PRE76 and POST76 were displayed in Figure 6.1 (a-d) and their respective surface and subsurface temporal components (principal components) were plotted in Figure 6.1e&f. The correlations between the surface and subsurface variability during PRE- and POST- 76 periods were 0.72 and 0.5 respectively. The surface mode explains 31% of the SST variability during PRE76 while it has increased to 49% during POST76 suggesting a strengthening of this mode after 1976. Further, the correlation between surface and subsurface mode reduced from 0.72 to 0.50 from PRE76 to POST76 indicating that the SST and subsurface variability relationship had decreased. This mode has higher amplitude in the western equatorial Indian Ocean compared to the eastern equatorial Indian Ocean during both PRE76 and POST76. However, there is substantial increase in the amplitude of this mode from PRE76 to POST76. Sun et al. (2019) had reported that this warming is of the order of 0.35 °C during summer.

The first mode of inter-annual SST variability is obviously associated with Indian Ocean Basin Mode (IOBM) forced by ENSO in the Pacific (Klein et al., 1999; Yang et al., 2007; Chowdhary and Gnanaseelan, 2007; Guo et al., 2018; Sun et al., 2019). The studies of Sun et al. (2019) has indicated substantial warming of western Indian Ocean during summer post late 70s suggesting that the features of IOBM shifted towards Arabian Sea, while there is no considerable change in IOBM in the eastern tropical Indian Ocean between PRE76 to POST76.

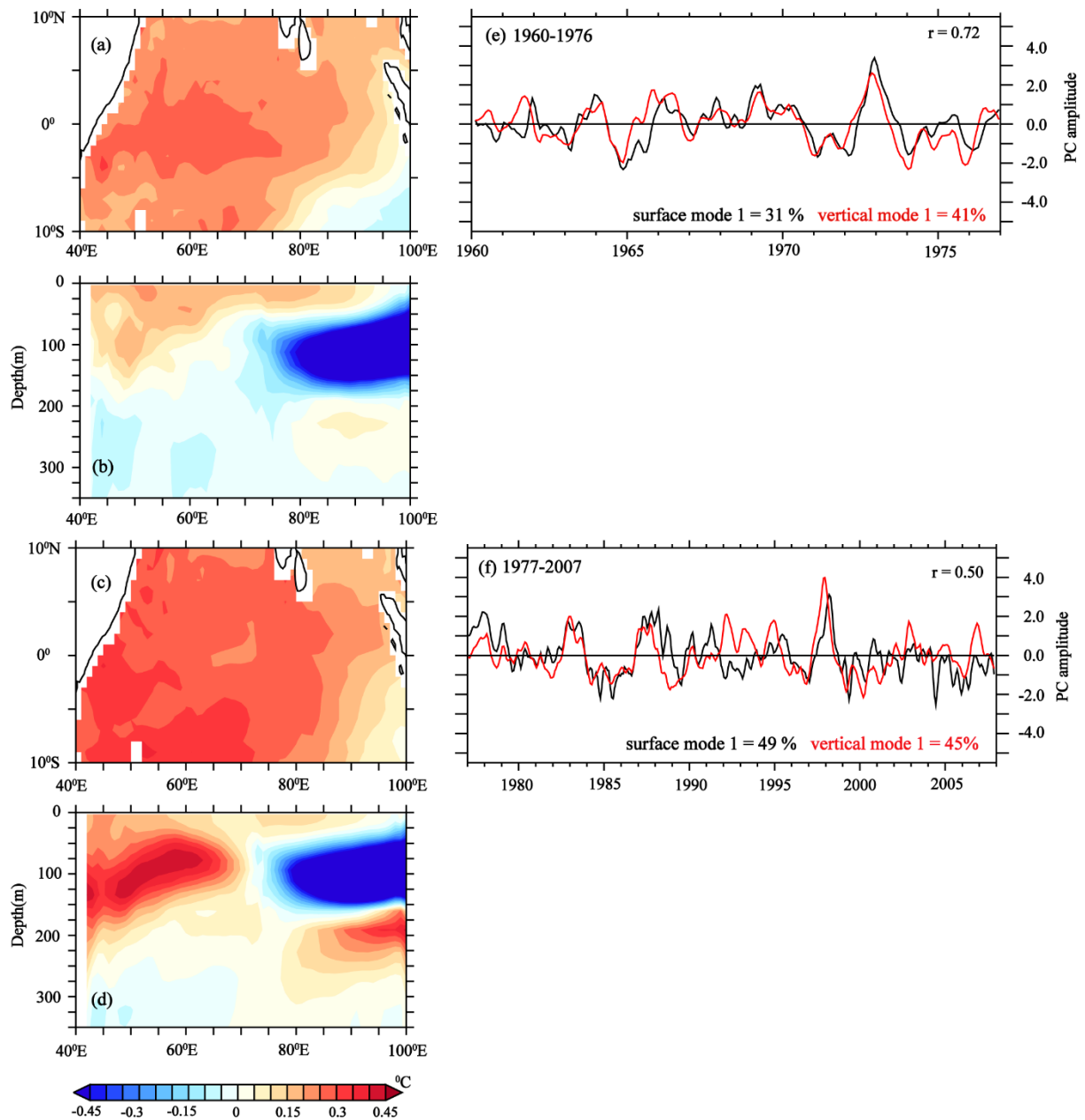


Figure 6.1 First mode of EOF patterns for surface (a- PRE76 period & c-POST76 period) and vertical fields (b- PRE76 period & d-POST76 period) and corresponding time series of normalized principal components (e- PRE76 period & f-POST76 period; Black line is surface and red line is vertical field). 1960-1976 periods are called PRE76 and 1977-2007 periods are called POST76. Correlation between the surface and vertical fields are written inside the figure.

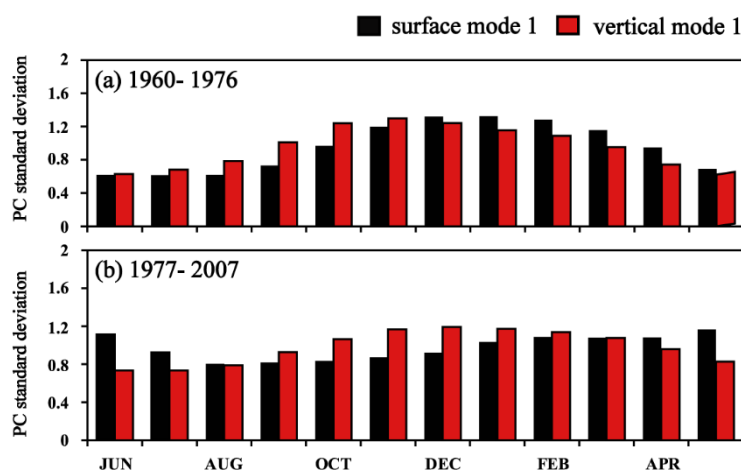


Figure 6.2 Monthly standard deviation of normalized principal components of surface and vertical modes of first EOF of inter-annual temperature anomaly for 1960-1976(a) and 1977-2007(b).

The monthly standard deviation of normalised principal components of surface mode of first EOF for PRE76 and POST76 show substantial changes during both epochs. The maximum warming due to this mode was in winter during PRE76 (Figure 6.2a) which shifted to spring and summer in POST76 era (Figure 6.2b) with maximum amplitudes during May-June and even beyond. The reason for this shift is yet to be understood. Sun et al. (2019) reported that the summer time warming of north western Indian Ocean after late 70s has significant effect on the Asian summer climate. They have shown that the enhanced convection over Arabian Sea due to this warming may stimulate a Kelvin Wave featuring easterly low level wind anomalies over Arabian Sea, India and eastern Tropical Indian Ocean producing divergence and subsidence in planetary boundary layer of Bay of Bengal, Southern China, South China Sea and Indo-china causing regional weather and climate changes.

The vertical mode of IOBM (Figure 6.1b& d) also shows significant variability from PRE76 to POST76. The maximum variability in the vertical is noticed at 70-150 meter depth during both epochs. However, there is a well-developed dipole mode in the vertical at these depths in POST76 era (Figure 6.1d), which was less prominent during PRE76 (Figure 6.1b). This indicates substantial variations in subsurface temperature associated with IOBM from PRE76 to POST76 and the vertical variations are more pronounced than surface variations. The reason for such a dipole mode in the vertical in the IOBM only POST76 needs further investigation. The subsurface expression of IOBM explains 41% percent of vertical temperature variability during

PRE76 which increased to 45% POST76 (Figure 6.1e& f). In brief, the subsurface expression of the IOBM has a nominal increase (4%) from PRE76 to POST76 while the change is substantial at the surface (18%) which could be the reason for weakening the correlation between the surface and subsurface PCs along with the development of subsurface dipole POST76. The effect of IOBM is more pronounced at the surface during spring and summer during POST76 while in the vertical it peaked during winter and spring (Figure 6.2b). This indicates the subsurface variations of IOBM is noticed at least a couple of months ahead of the surface manifestations. The primary PCs of both surface and subsurface temperature fields were then correlated with ENSO and IOD indices during PRE76 and POST76 eras. The correlations were significant with values 0.6 (0.4) during PRE76 (POST76) period for surface temperature field while the corresponding values at subsurface depth were 0.8 and 0.72 for PRE and POST76 periods respectively. The correlations between PC1 and the IOD indices were relatively weak and hence figures are not presented.

Figure 6.3 displays the same analysis as Figure 6.1, but for the second mode of EOF. These second modes have a weaker percentage of variance i.e. 28 and 20 for surface and vertical fields of PRE76 (Figure 6.3e) period and 13 and 16 for POST76 period (Figure 6.3f) respectively indicating a lesser variance of SST due to the second mode. Although the correlation values between surface and vertical EOFs are not so high in these second modes, yet they are related to each other in both epochs. Their respective PC's are correlated to each other with 0.62% for PRE76 which reduced to 0.40% for POST76 period (Figure 6.3e& f). This reveals that they also represent the same mode of variability on both periods. The east-west shift in polarity at both surface and subsurface is a manifestation of the temperature pattern associated with the Indian Ocean Dipole (IOD). Therefore, the second mode of variability of the EOF is associated with IOD (Saji et al., 1999; Webster et al., 1999, Saji and Yamagata, 2003). As the first mode is associated with the ENSO induced IOBM, the less pronounced IOD pattern in the second EOF mode indicated the co-occurring of these two inter-annual climate modes (Annamalai et al., 2003; Luo et al., 2010; Izumo et al., 2010, 2013). In the vertical the amplitude of the IOD seems to have slightly weakened from PRE76 to POST76. Moreover, the vertical mode has maximum amplitude in the thermocline compared to surface layers.

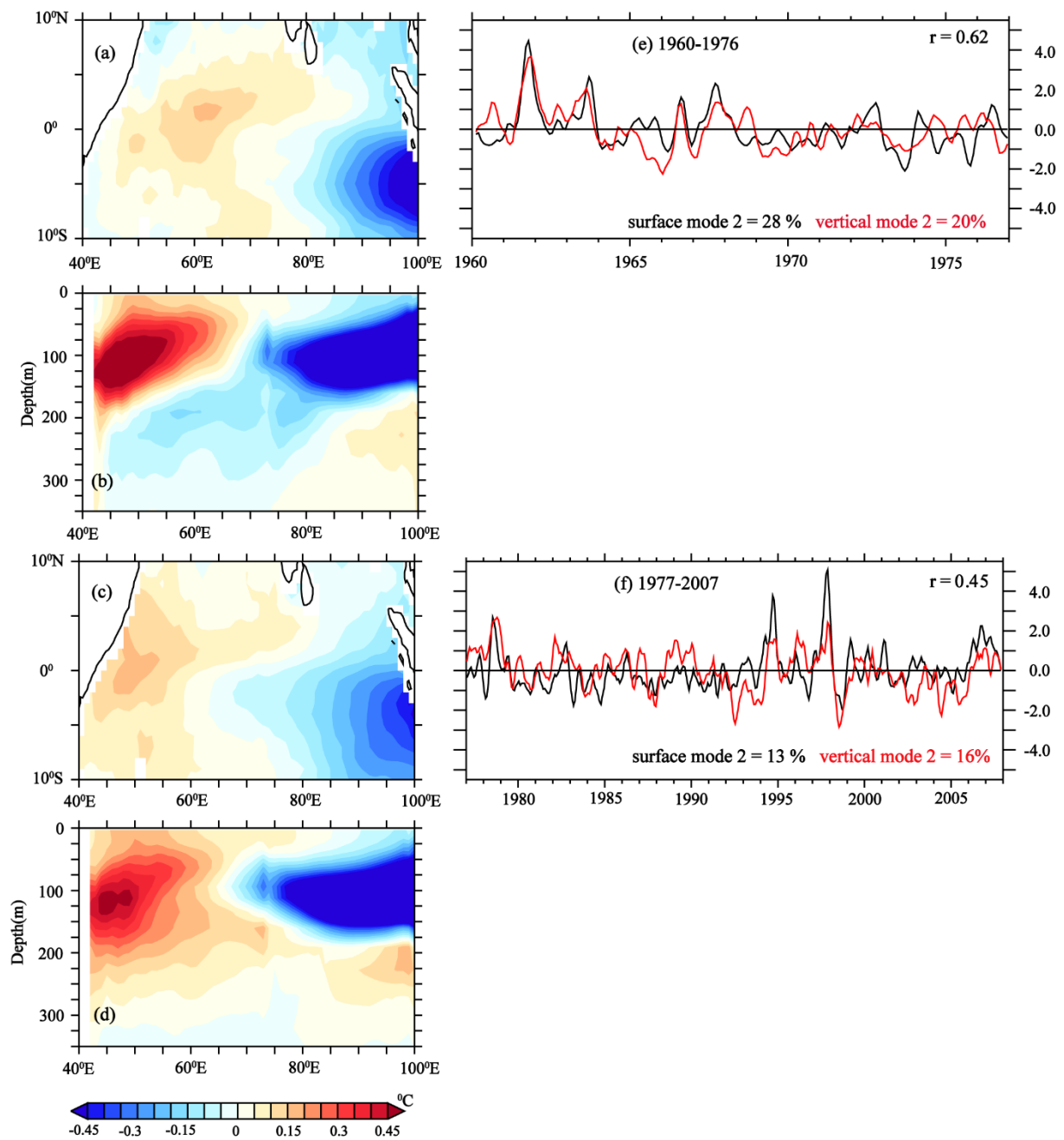


Figure 6.3 Second mode of EOF patterns for surface (a- PRE76 period & c-POST76 period) and vertical fields (b- PRE76 period & d-POST76 period) and corresponding time series of normalized principal components (e- PRE76 period & f-POST76 period; Black line is surface and red line is vertical field). 1960-1976 periods are called PRE76 and 1977-2007 periods are called POST76. Correlation between the surface and vertical fields are written inside the figure.

The standard deviation of normalized principal components of surface and vertical modes of second EOF of inter annual temperature anomaly for PRE76 and POST76 are displayed in

Figure 6.4. The standard deviation of the PCs of PRE76 suggest the surface temperature variability peak in September- November, indicative of a full- fledged IOD, while at subsurface the peak spreads from August to December (Figure 6.4a) one month ahead of surface peaking. However, during POST76 period the surface temperature amplitude does not change much from PRE76, but the peaking of subsurface amplitude is noticed in June- August period, one to two months prior to the surface peaking (Figure 6.4b).

The stratified IOD amplitude (Figure 6.4) reveals that the secondary mode of variability is largely representative of inter-annual variability of temperature during fall season (October- November) in both epochs. The IOD amplitude is maximum in September- November (~1.6 for PRE76 and POST76 period). Also there exists high correlation with IOD index and second mode of EOF (PC2) in both epochs than with ENSO index (figures not shown). The correlation between IOD index and PC2 during PRE76 period is 0.7 and 0.8 for POST76, while the correlation value between PC2 and ENSO index is comparatively low (0.17 for PRE76 and 0.3

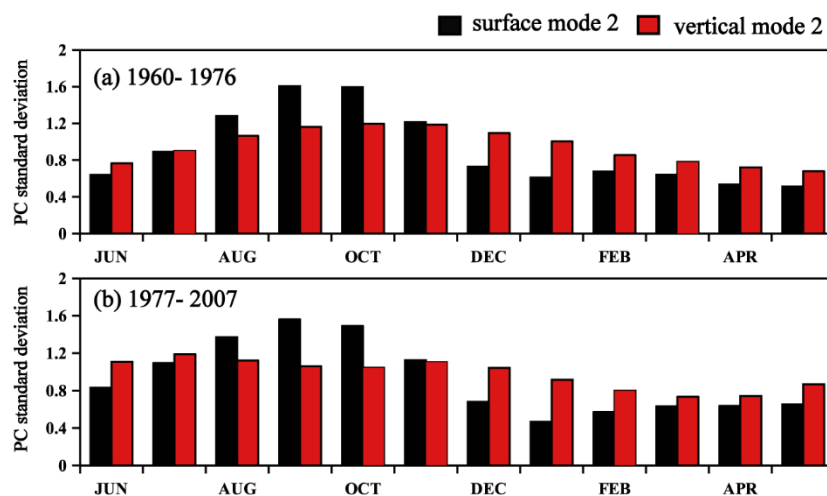


Figure 6.4 Monthly standard deviation of normalized principal components of surface and vertical modes of second EOF of inter annual temperature anomaly for 1960-1976(a) and 1977-2007(b).

for POST76) further highlighting the fact that this mode of variability in both epochs is representative of Indian Ocean Dipole related inter-annual variability of temperature at the equatorial IO. Similarly, the primary mode of variability's in the surface temperature pattern in both epochs was representative of ENSO related variability in the inter-annual time scale.

Lead-lag correlations between PCs representing surface and vertical fields for both PRE76 and POST76 periods are displayed in Figure 6.5. It has been noticed from Figure 6.5a that subsurface temperature field is leading surface by about 2-3 months with significant correlation of ~ 0.8 and ~ 0.6 during PRE76 and POST76 periods respectively. This indicates that during PRE76 period, winter surface temperature variations represented by EOF1 is generally followed one season later by fall subsurface variability. It means a delayed influence of IOD is seen at the winter surface temperature field during PRE76 period.

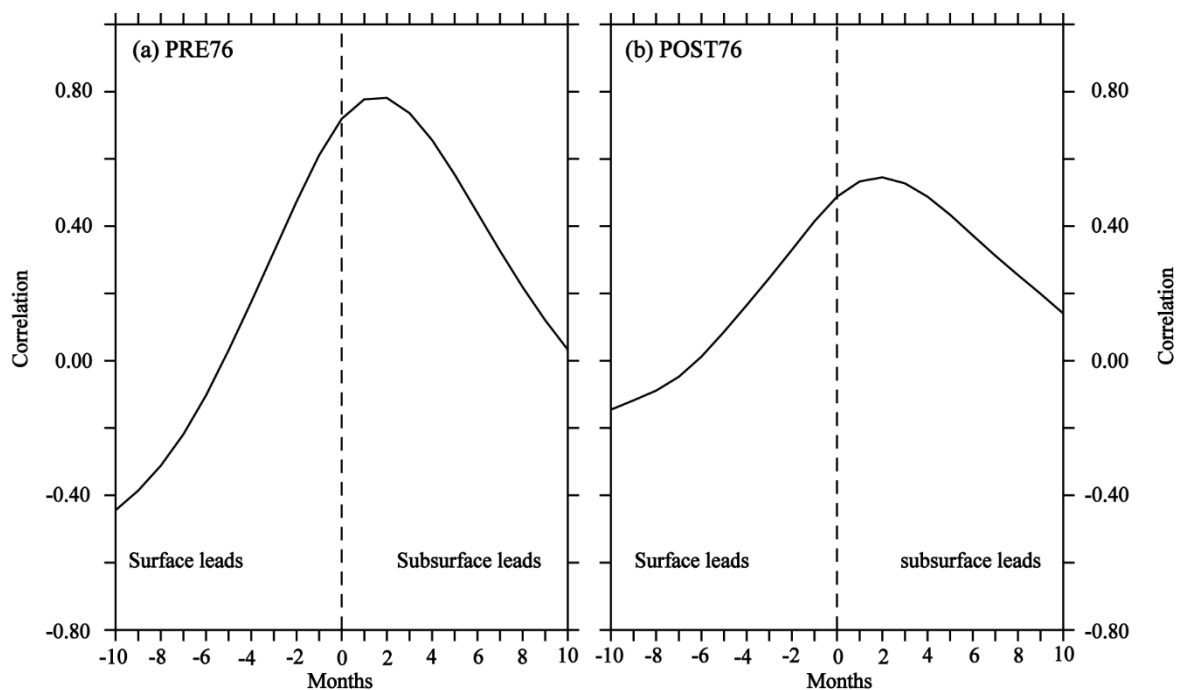


Figure 6.5 Lead-lag correlation between surface and vertical fields of first EOF for PRE76 (a) and POST76 (b) period

During POST76 period, it has been noticed from Figure 6.5b that the subsurface temperature field is again leading the surface field by 5 months (January- May) with significant but relatively weaker correlations varying from 0.4- 0.6 spread over a longer period. It means that the subsurface variability leads the surface variability influenced by delayed ENSO peaking in late winter and spring. In other words, during POST76 period, the spring surface temperature variability forced by delayed ENSO is followed by one season after winter subsurface temperature variations. The winter subsurface temperature variability could be due to the delayed influence of fall IOD prior to the winter season as highlighted in the PRE76 period.

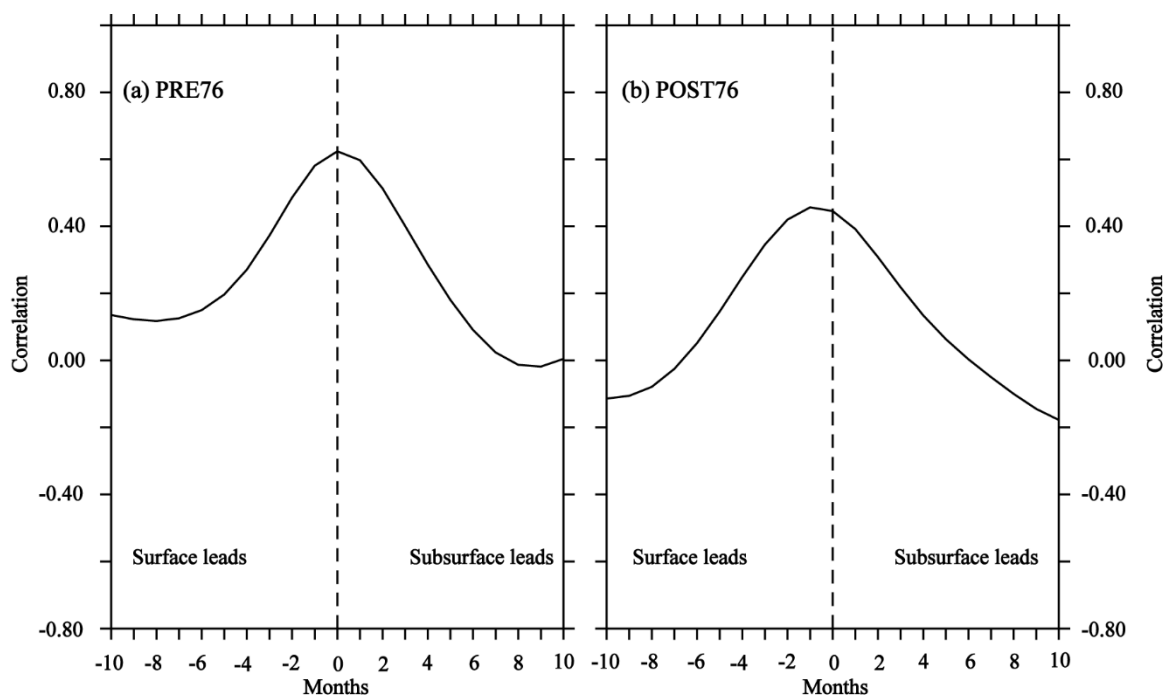


Figure 6.6 Lead-lag correlation between surface and vertical fields of second EOF for PRE76 (a) and POST76 (b) period

The lead lag correlation between surface and subsurface fields of second EOF mode for PRE76 and POST76 period are illustrated in Figure 6. In PRE76 period, surface and vertical fields of EOFs were in phase (Figure 6.6a) with significant correlation of ~ 0.6 . It is yet to be ascertained the dynamics behind the PRE76 surface- subsurface relationship. The POST76 surface temperature field was leading the vertical by about one month with significant correlation of ~ 0.5 . The surface manifestation in POST76 could be due to the easterly wind forcing in fall-winter monsoon that take about one month to build the pressure gradient that trigger deepening of thermocline at the west and shoaling eastward. In general, IOD was the dominant factor in modifying the surface and subsurface temperatures during both epochs.

However, as already stated in the literature (Annamalai et al., 2003; Izumo et al., 2013), IOD and ENSO events showed strong tendency to co-occur. During PRE76 the IOD and ENSO were having a weak correlation of ~ 0.25 and in POST76 period this correlation increased to 0.45. The combined influence of IOD and ENSO on IO temperature is summarized in Figure 6.7 (a, b,

c&d), that shows a simple regression analysis of temperature and zonal winds in the IO onto ENSO and IOD indices for both epochs.

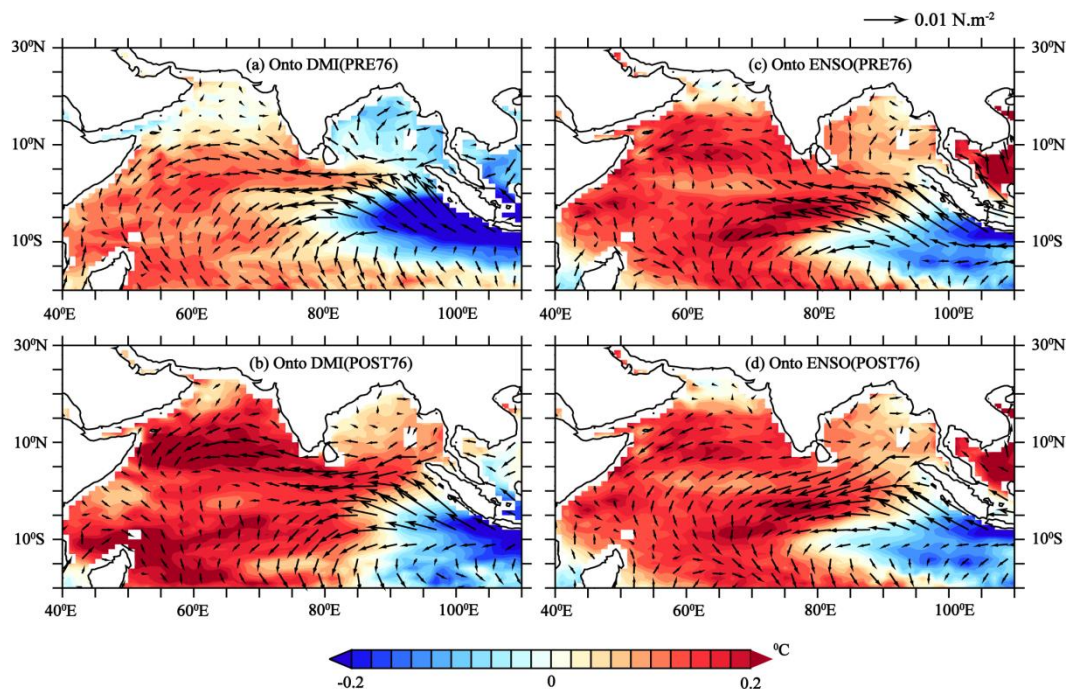


Figure 6.7 Simple regression analysis performed between Indian Ocean surface temperature (shaded) onto IOD and ENSO indices for PRE76 (a & c) and POST76 (b & d) period. Vectors are windstress anomalies.

These figures of simple regression with both indices show a similar pattern for PRE76 (Figure 6.7, top panel) and POST76 (Figure 6.7, bottom panel), but a visible difference in the amplitude of influence of indices. Even though these patterns were more or less similar to each other, it didn't separate the individual influence of IOD/ENSO on IO temperature system. To better ascertain the relationship between two modes of equatorial temperature variations with both IOD and ENSO climate modes, partial correlation analysis of surface PC1 and PC2 onto IOD and ENSO indices was performed for both epochs. Figure 6.8 displays partial correlation analysis of surface PC1 and PC2 onto ENSO and IOD indices. Figure 6.8a indicated that during PRE76, ENSO was having maximum correlation with PC1 in winter ($r \sim 0.9$), suggesting that this mode of variability peaking in winter exerts maximum control on inter-annual variability of warming in winter season. Significant correlations were also evident in spring ($r \sim 0.8$) further demonstrating that ENSO during its demise phase also influences the equatorial temperature variations. As shown on Figure 6.8a, IOD also influences the temperature variations at the equatorial Indian

Ocean. However, compared to ENSO, their control onto temperature is not strong. Figure 6.8c displayed the partial correlation analysis between the indices and the surface PC1 for POST76 period and revealed that ENSO was having maximum correlation with surface PC1 during spring

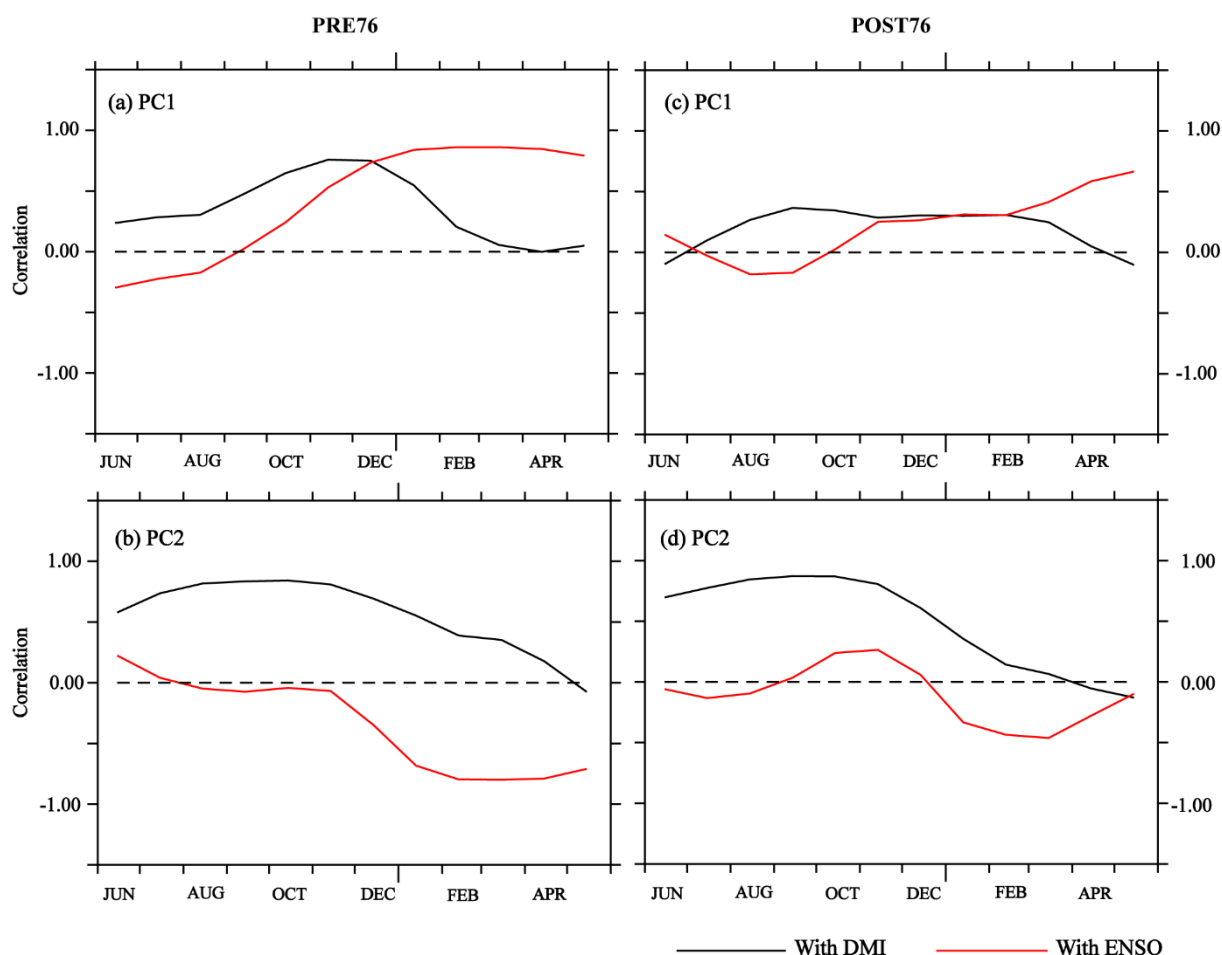


Figure 6.8 Partial correlation analysis performed between the first (PC1) and second (PC2) EOFs of equatorial Indian Ocean surface temperature onto IOD and ENSO indices for PRE76 (a & b) and POST76 (c & d) period. Red line is ENSO and black line is IOD.

($r = \sim 0.6$), highlighting that this variability was exerting maximum control over equatorial temperature during spring season. Further, ENSO in its demise phase strongly influenced the inter-annual variability of equatorial temperature. A second highest correlation was seen between ENSO index and PC1 during winter season ($r = \sim 0.4$). IOD was also having maximum correlation with PC1 during this season ($r = \sim 0.35$). So, both climate modes were controlling the inter-annual variability of equatorial Indian Ocean temperature in the winter season. This result also suggested

that after the regime shift (POST76), the strength of ENSO was getting reduced by its co-occurrence with IOD.

Figure (6.8b& d) displayed the partial correlation analysis of surface PC2 onto ENSO and IOD for PRE76 and POST76 period, describes that during PRE76 and POST76 IOD was having maximum correlation with PC2 in fall season ($r = \sim 0.8$ PRE76 and $r = \sim 0.9$ POST76), indicating that in both epochs this mode of variability peaking in fall exerts maximum control over the inter-annual variability of equatorial IO temperature in fall season. Significant correlations were also found on summer season ($r = \sim 0.7$ PRE76 and $r = \sim 0.7$ POST76) further demonstrating that IOD in its onset phase also influences equatorial temperature system. Further, the value of maximum correlation had been increased from ~ 0.8 to ~ 0.9 in POST76 period. ENSO index and surface PC2 are not significantly correlated in both epochs. Therefore, these facts point that IOD induced inter annual variability in fall warming at the equatorial IO is getting strong after the climate shift. At the same time ENSO does not have much influence on this variability in both epochs.

To summarize this section, before the climate shift of 1976-1977, ENSO was controlling the inter-annual variability of basin wide winter warming. But after the climate shift, ENSO on its demise phase had strong influence over equatorial IO warming. So, they exhibited the delayed influence of ENSO after the climate shift. Results further revealed that after the climate shift, delayed influence of IOD also had influence over the basin-wide winter warming. The second mode of variability, that is the inter-annual variability of fall warming on both epochs were mainly controlled by Indian Ocean Dipole and this influence was getting stronger after the climate shift.

Variability and trend analysis of hydrographic parameters in the decadal time scale

7.1 Introduction

It has been observed that the global oceans were heating up and they contribute more than 90% of the warming seen on the earth by emission of greenhouse gases due to anthropogenic changes. Owing to the rapid advancement of technology, long-term real-time surface and subsurface data collection and dissemination are now possible. Long duration hydrological observations on-board several platforms carried out at the upper strata of the tropical Indian Ocean brought out substantial variability in the inter-annual time scales, in general, and decadal variability at isolated regions of the tropical Indian Ocean. From 1960 onwards, Indian Ocean was exhibiting a warming trend at the surface and subsurface depth. It had been observed in recent studies that the warming trend and decadal variability of Indian Ocean sea surface temperature could have huge impact on climate both within the Indian Ocean rim countries and in other regions of the globe through atmospheric teleconnection (Han et al., 2014). While satellite data has the potential to investigate long term trends on surface hydrographical parameters on a global scale, region specific *in situ* data described the variability at both surface and subsurface depths on relatively shorter time scale. The scarcity of observational data on longer time scales (decadal to epochal) in both space and time could be overcome by relying on properly validated model data products as shown by the recent published articles (E.g.: Han et al., 2014). By infusing satellite and other *in situ* data products into the few promising Global General Circulation models, the researchers kept generating more refined long-term data products to address the decadal and epochal trends with better accuracy. In spite of these efforts, the various model data products failed to generate results with some uniformity. One of the reasons for this ambiguous performance might be the lack of long term *in situ* data in both space and time to incorporate in the Global Circulation Models.

7.2 The data sets used in the decadal trend/variability analysis.

It has been observed that several model simulations were used to address the decadal trends of temperature and salinity in the surface water column in the global oceans. Out of that, few model simulations were successfully used in the recent past to explain the variabilities within the tropical Indian Ocean in a longer time scale. In the present thesis, two such model simulations; ORAS4 (Ocean Reanalysis/Analysis System4) and GECCO (German contribution of the Estimating the Circulation and Climate of the Ocean) were selected to address the decadal variability at both surface and subsurface depths after undertaking a validation experiment by comparing with *in situ* products namely HADISST (Hadley Centre Global Sea Ice and Sea Surface Temperature) for surface and ARGO (Array of Real time Geostrophic Oceanography) for subsurface depths. The details of the validation experiments were given under Data and Methods (Chapter 3; Section 3.4).

7.2.1 Decadal variability of Temperature at the equatorial Indian Ocean

Although the validation experiment indicated the efficiency of both ORAS4 and GECCO2 simulations in predicting temperature at surface and subsurface depth, the GECCO2 simulation had been chosen for two reasons. Under this simulation, the surface and subsurface temperatures were available from the year 1950 thereby getting one more decadal cycle in comparison with the ORAS4 simulation which starts only from 1960 onwards. Secondly, the GECCO2 simulation had predicted more refined values of subsurface temperatures compared to the ORAS4 simulation. The first stage of data processing was the detrending of the time series SST data as SST is often taken as a proxy for understanding the dynamics of Indian Ocean Dipole. Subsequently the climatological mean was subtracted from monthly fields to amplify the variabilities. An eight-year Lanczos lowpass filter was then applied on the data to remove seasonal to inter annual oscillations so as to retain only the decadal variabilities. The data was then subjected to the Empirical Orthogonal Function Analysis (EOF). The same process of data analysis was repeated for the subsurface temperature structure to highlight the prominent variability in the decadal scale by subjecting the vertical temperature structure to the EOF analysis.

EOF analyses are often used to study possible spatial patterns of climate variability and how they change with time. Here the data was decomposed to generate mutually orthogonal space-time patterns where the data variance was concentrated. Such orthogonal patterns were derived by computing the eigenvectors of a spatially weighted anomaly of covariance matrix, and the corresponding eigen values provided a measure of the percent variance explained by each pattern. In the present scenario, the leading modes of EOF analysis of both surface and vertical temperature structure displayed variances of 46% and 50% respectively and hence were strong enough to explain the temporal evolution of both spatial pattern and vertical structure of SST at the equatorial Indian Ocean.

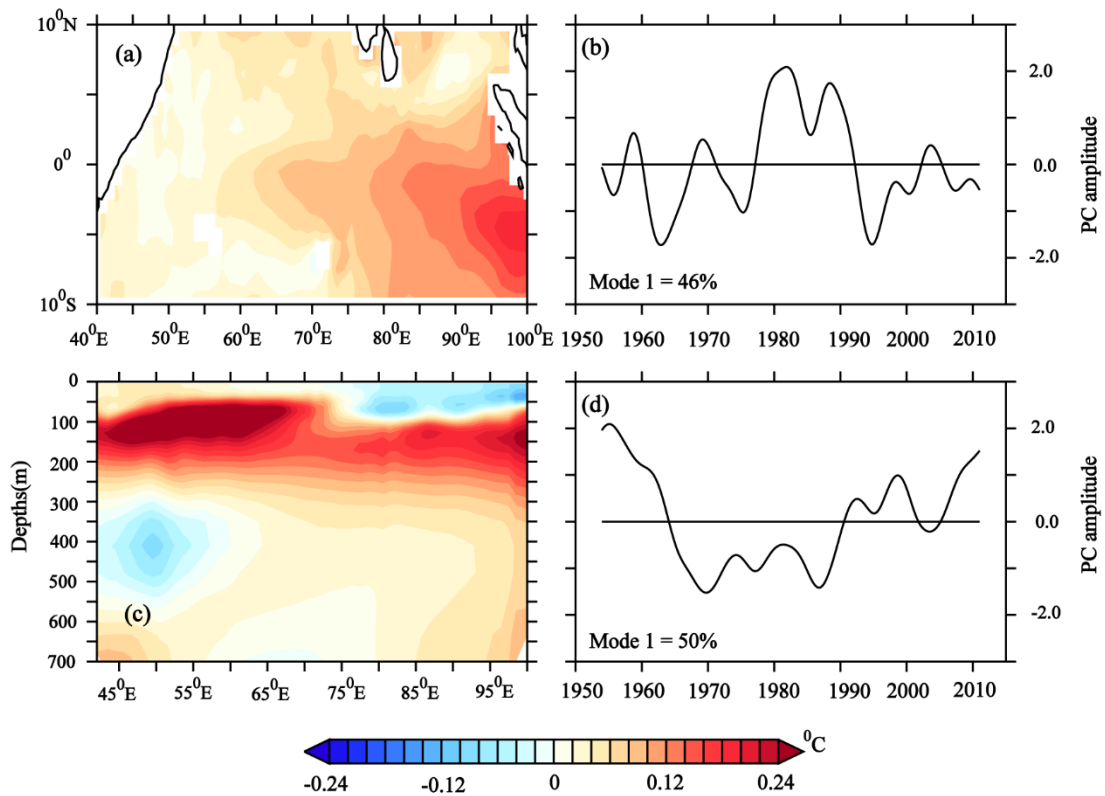


Figure 7.1 EOF analysis performed on surface temperature (a & b) and temperature at depths (c & d) from GECCO2 data for the period 1950-2014. The spatial (EOF) and temporal (Principal Component) patterns were displayed in left and right panels respectively. The temperature at depths was averaged between 10° N and 10° S before submitting to EOF analysis.

Although the spatial structure of SST resembled the traces of basin scale warming in the decadal scale, a closer look revealed strong pattern of variability close to the south-eastern equatorial region that weakened westward (Figure 7.1a). The temporal patterns (PC) of the surface variability determine the evolution of the spatial pattern as and when the polarity and amplitude of the PC vary with time in decadal scale (Figure 7.1b). During the first few decades, the average state of the surface temperature pattern resembled the positive dipole structure at the equatorial IO with cooler than normal temperature occupies at the south-eastern zone of the equator while warmer than normal water at the western equatorial IO. Then from 1980 to 1995, the mean mode of variability was just the opposite with warmer water at the east and cooler water in the west depicting the dynamics associated with negative IOD winds often found to drive the inter-monsoonal Wyrтки Jet (Wyrтки, 1973). The situation changed again in 1995 witnessing resurgence of the dipole pattern at the surface thermal field in the decadal time scale (Figure 7.1a& b). The leading mode of the vertical temperature structure also indicated anomalous warming at the western half of the surface layer and cooling at the east. The warmer thermocline at the west appeared to shoal towards east leaving upwelled cooler water at the surface in response to the steady easterlies reminding the mature state of IOD (Figure 7.1c). This typical IOD pattern observed in the subsurface layer was the mean pattern of variability in the decadal scale (Figure 7.1c) and it appeared to evolve from positive to negative IOD pattern by the end of 1970 and again reappeared in late 1990 (Figure 7.1d). Therefore, both these surface and vertical EOF modes establish the fact that IOD was the prominent mode of variability prevalent in the decadal time scale at least in the temperature field. Moreover, the leading PCs of both surface temperature and temperature at depths had significant correlations of 0.60 and 0.89 respectively with the PC of IOD wind within the equatorial domain (10° S - 10° N & 40° E- 110° E) (Figures are not shown). In another experiment the western equatorial Pacific wind (5° N- 5° S & 130° E- 80° W) also indicated fairly good correlation ($r=0.45$) with the surface and subsurface temperature fields in the equatorial IO in decadal time scale (Figure not shown). So, on decadal scale, both IOD and equatorial Pacific winds have respective roles in modifying the dynamics of the equatorial IO. Therefore, it has been construed from the above results that the wind dynamics largely modify the inter-ocean water exchange through the Indonesian through Flow in the decadal time scale.

7.2.2 Decadal variability of Salinity at the equatorial Indian Ocean

In the validation experiment it had been observed that the near surface and subsurface (80-150 m average salinity) salinity derived from ORAS4 simulation at selected locations (due to lack of continuous matching *in situ* model data combinations elsewhere) indicated fairly good correlation with the Argo salinity profiles compared to the GECCO2 model simulation. Therefore, the gridded ORAS4 data at the equatorial domain (40° E – 100° E & 10° N – 10° S) had been used to analyse both surface and vertical salinity variability in the decadal time scale. The same data processing techniques used in the previous section for temperature had been followed to highlight the decadal signals of salinity. The data were then decomposed to spatial and temporal patterns by subjecting them to the EOF analysis and the results were reproduced in Figure 7.2.

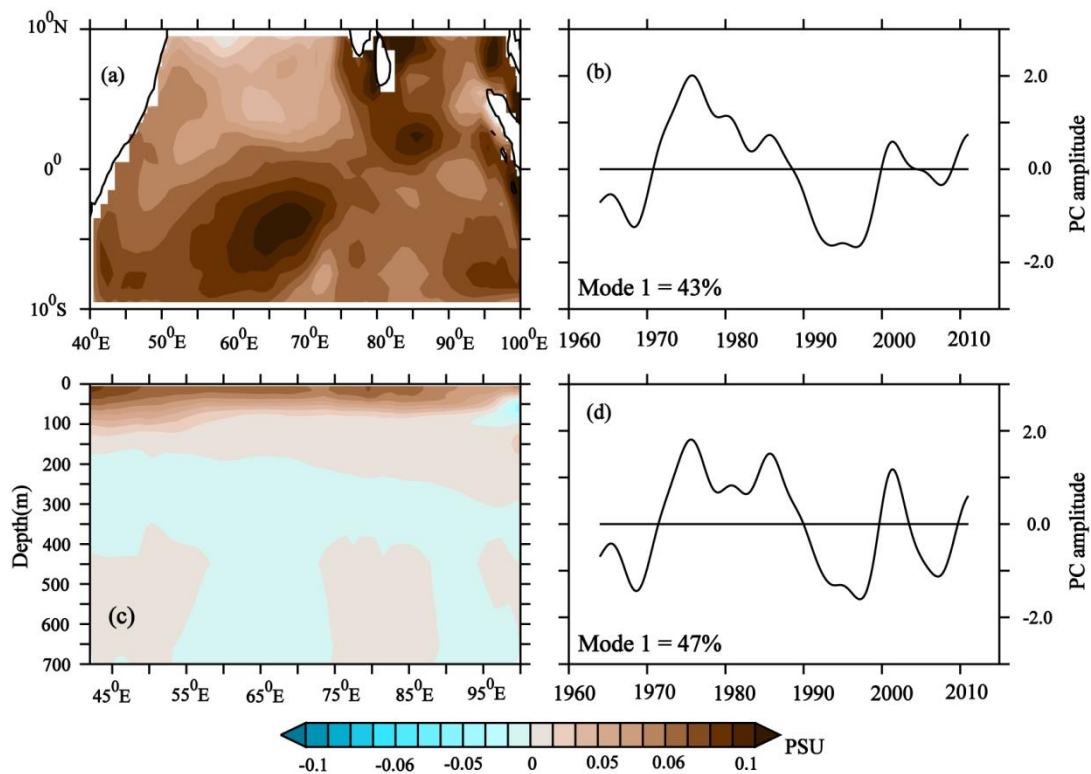


Figure 7.2 Empirical orthogonal function patterns for surface salinity (a&b) and vertical section of salinity(c&d) from ORAS4 model data. The spatial (EOF) and temporal (Principal Component) patterns are displayed in left and right panels respectively. The salinity at depths are averaged between 10° N and 10° S before submitting to EOF analysis.

As explained in the previous case, the eigenvalues corresponding to the eigenvectors of a spatially weighted anomaly of covariance matrix provided a measure of the percent variance explained by each pattern. In the case of salinity, the leading modes of EOF analysis of both surface and vertical salinity structure displayed variance of 43% and 47% respectively and hence in technical terms strong enough to explain the temporal evolution of spatial patterns both horizontally and vertically at the equatorial Indian Ocean in the decadal time scale. Salinity structure was equally important as temperature to explain the dynamics of ocean circulation. In addition to controlling physical properties, variations of temperature and salinity in space and time are well known water mass tracers that can be used to map the ocean circulation. The widely used term 'density' has a close link to temperature and salinity other than pressure; often combinely called an equation of state.

The right panels of Figure 7.2 displayed the main characteristics of the principle components (PC) associated with these surface and vertical EOF modes. First striking observation was that the PCs of first EOFs of surface and subsurface salinity anomalies in the decadal time scales were strongly correlated ($r=0.9$; right panels of Figure 7.2) indicating that the surface and subsurface variabilities depicted by these first EOFs were related to same mode of variability in the decadal time scale. The left panels of Figure 7.2 displayed the spatial patterns associated with the surface and subsurface PCs. The northern and southern half of the equatorial domain exhibited a peculiar salinity structure where positive anomalies concentrate on eastern half in the northern hemisphere while it reversed in the southern hemisphere of the equatorial domain. The clustering of positive anomalies around the shallow thermocline dome at the south-central equatorial domain (60° E- 70° E & $0 - 10^{\circ}$ S) largely distorted the patterns in both spatial and vertical fields as it was considered as the environmentally sensitive and oceanographically dynamic region. In general, the polarity of PCs in both spatial and vertical fields reversed in the second half (post-1990) of the decadal scale. During the post-1990 (1990-2000) period, relatively low saline water occupies the eastern equatorial region compared to the west indicating the influence of easterlies (positive IOD) that bring low saline water to the eastern equatorial Indian Ocean from western Pacific and Bay of Bengal during the post-1990 period and relatively saline water at the eastern equatorial ocean during 1970-1990 period by the prevailing westerlies (descending branch of Walker cell develop at the west) that often drives an eastward Wyrтки jet

(negative IOD). The weak fluctuations seen in the PCs of post 2000 period, however, indicated increasing frequency of both positive and negative IODs of moderate strength. The occurrence of El Niño became more frequent in Pacific due to the abnormal warming of oceans especially post 1990 years (Chowdery and Gnanaseelan, 2007; Roxy et al., 2014). It had also been noticed that the frequency of occurrence of IOD at the equatorial Indian Ocean had increased many folds ever since its discovery in 1999 (Saji et al., 1999) and its link with El Niño and the warming climate cannot be ruled out (Ihara et al., 2008; Du and Xi, 2008; Hoerling et al., 2004).

As the strong correlation between the PCs ($r = 0.90$) of horizontal and vertical field indicated both EOFs were related to the same mode of variability, the contours of positive anomaly that appeared to shoal eastward could be associated with the subsurface manifestation of the surface IOD pattern (Figure 7.2c). The continuous stretch of positive anomaly of subsurface salinity all the way from west to east appeared to be the result of meridional averaging of salinity from 10° N to 10° S that distorted the signals of east-west salinity gradient close to the equator. Therefore, the surface (spatial) and subsurface (vertical) manifestation of zonal current was the mean pattern of variability in the decadal time scale and that evolved into positive and negative phases (of IOD) according to the fluctuations in the temporal scale (PCs).

7.2.3 Linear trend analysis of temperature and salinity in decadal time scale at the equatorial Indian Ocean

7.2.3.1 Linear trends in temperature at the surface

The basin scale surface warming of the Indian Ocean had been a reality (Du and Xie, 2008; Hoerling et al., 2004) and appeared to be pacing faster than Pacific Ocean over the past 60 years (William and Funk, 2011). The surface warming of the eastern equatorial Indian Ocean (EEIO) in decadal time scale spreads to the central equatorial ocean as a large warm pool capable of modifying the Hadley Cell circulation (Gnanaseelan and Roxy et al., 2007) thereby altering the surface wind pattern (Yamagata et al., 2002). Similar ocean and atmosphere conditions implied that a Bjerknes-type (Bjerknes, 1969) feedback mechanism was responsible for the IOD evolution in the decadal time scale (Yamagata et al., 2002). The zonal Walker circulation was another process that may link the IOD events in the Indian Ocean with ENSO events in the

Pacific. It had been shown by Yamagata et al. (2002) that the atmospheric bridge between the two Ocean basins was evident when all IOD events that include the co-occurring ENSO events were considered. The impact of IOD, as expected from the practice of ENSO, was not limited only to the equatorial Indian Ocean. By modulating the atmospheric circulation, IOD influences the world climate (Saji and Yamagata, 2003). The trend analysis explained the extend which the eastern and western equatorial Indian Ocean was warming as Ihara et al. (2008) had already reported the warming of these two important zones in the decadal scale.

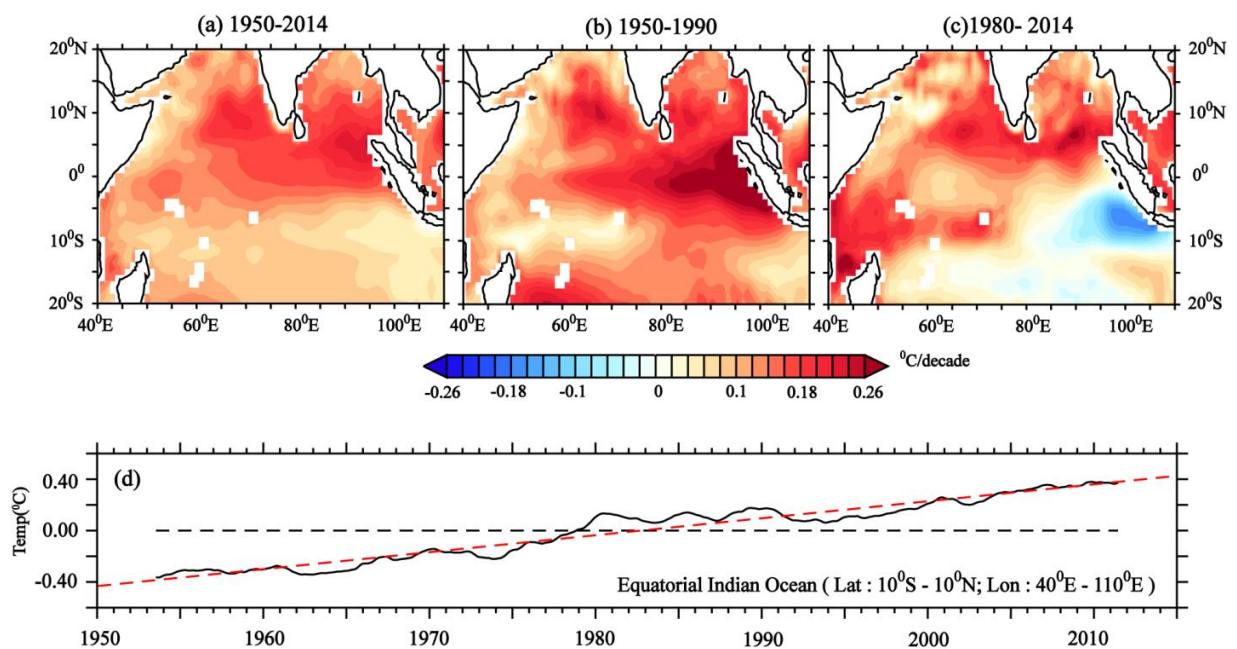


Figure 7.3 Spatial distribution of the slopes of linear trend of surface temperature anomaly determined grid-wise in decadal time scale over the tropical Indian Ocean using GECCO2 model data for the period 1950 – 2014 (a), 1950-1990 (b) and 1980- 2014 (c). The linear trend of monthly mean temperature anomaly computed within the equatorial box bounded by 10° N-10° S latitude and 40° E-110° E longitude for the period 1950-2014 (d). 7year running mean is applied in all cases to remove seasonal and inter annual oscillations to highlight the decadal signals.

The monthly temperature anomalies (from GECCO2 model) at each latitude-longitude grid, after removing the seasonal and inter-annual oscillations by applying a seven year running mean to highlight the decadal signals, during 1950-2014 period were used to compute the slope of the linear trend in order to construct spatial trend map of the tropical Indian Ocean (Figure 7.3a). As the warming accelerated in post 1980 period, two more such maps were created to represent the periods 1950-1990 and 1980-2014 and displayed all in Figure 7.3 a- c (upper panel). The linear trend of the mean temperature anomaly in the equatorial box (10° S-10° N; 40° E-110°

E) during the period 1950- 2014 was displayed in Figure 7.3d that indicated a warming trend of $0.12\text{ }^{\circ}\text{C}/\text{decade}$ which was higher than Pacific ($0.08\text{ }^{\circ}\text{C}/\text{decade}$) (Figure 5 of Han et al., 2014). The observation of Hoerling et al. (2012) suggested that the tropical Indian Ocean was warming faster than the tropical Pacific and Atlantic since 1950s with an accelerated warming during post 1970 period. It appeared (from the Figure 7.3a) that the equatorial domain of the tropical Indian Ocean exhibited accelerated warming trend of eastern half of the zone ($0.18\text{-}0.24\text{ }^{\circ}\text{C}/\text{decade}$) compared to the west ($0.06\text{-}0.12\text{ }^{\circ}\text{C}/\text{decade}$) during 1950-2014 period in the decadal time scale. However, the eastern equatorial warming trend intensified between 1950 and 1990 ($>0.24\text{ }^{\circ}\text{C}/\text{decade}$) but the eastern equatorial ocean witnessed accelerated cooling ($\sim\text{-}0.18\text{ }^{\circ}\text{C}/\text{decade}$) in the 1980-2014 period especially in the south-eastern equatorial Ocean aligned with the upwelled water usually associated with the equatorial easterlies that often drives the positive Indian Ocean dipole (IOD) (Figure 7.3b& c). It was to be noted from the earlier Figure (Figure 7.1 top panel) that the dominant pattern of the equatorial ocean since 1990 was the positive IOD in the decadal time scale where the south-eastern equatorial ocean was encompassed by cool upwelled water by the prevailing easterly winds. The Indian ocean warming trend might have contributed to the increased frequency of IOD as the tropical Indian Ocean experienced accelerated warming since 1970 (Hoerling et al., 2012).

7.2.3.2 Linear trends in temperature at depths

In addition to the discussion pertaining to the trend analysis of SST at the tropical Indian Ocean, an effort had been made to analyse the subsurface temperature trends at the equatorial Indian Ocean domain although most of the trend analysis seldom venture into subsurface levels. Monthly temperature anomalies were calculated at each longitude-depth grid for the period 1950-2014. The zonal vertical section of temperature anomaly was then prepared by averaging temperatures meridionally from 10° S to 10° N . A seven year running mean was applied subsequently to remove seasonal and inter-annual oscillations to project the decadal signals. This data was then subjected to linear trend analysis. The zonal vertical section of slopes of the linear trend in the decadal scale was displayed in Figure 7.4a. The surface warming, as seen in the previous section, appeared to be restricted to only surface 50m depth at the west and gradually spreading downward to 100m at the east in the decadal scale with signs of accelerated warming ($0.18\text{ }^{\circ}\text{C}/\text{decade}$) east of 70° E . On the other hand, the subsurface layer (80-150 m) appeared to

be cooling in the decadal scale with accelerated cooling ($-0.18\text{ }^{\circ}\text{C}/\text{decade}$) at the western equatorial IO. The trend calculated in the 80-150 m layer representing the entire equatorial box ($10^{\circ}\text{ S}-10^{\circ}\text{ N}; 40^{\circ}\text{ E}-110^{\circ}\text{ E}$) indicated the cooling was only minimal ($0.054\text{ }^{\circ}\text{C}/\text{decade}$) (Figure 7.4b) probably due to the zonal averaging of the slopes.

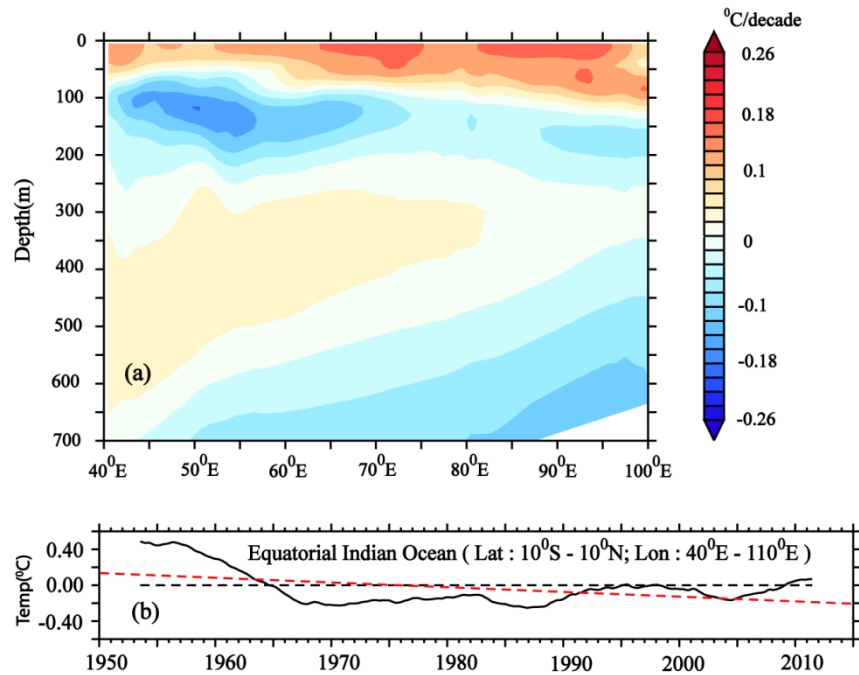


Figure 7.4 Vertical distribution of the slopes of linear trend of temperature anomaly in decadal time scale along the equatorial Indian Ocean by averaging the meridional values using GECCO2 model data for the period 1950 – 2014 (a). The linear trend of monthly mean temperature anomaly (80-150 m) computed within the equatorial box bounded by $10^{\circ}\text{ S}-10^{\circ}\text{ N}$ latitude and $40^{\circ}\text{ E}-110^{\circ}\text{ E}$ longitude for the period 1950-2014 (b). Seven year running mean is applied to remove seasonal and inter annual oscillations to highlight the decadal signals.

Through a hierarchy of OGCM experiments, several studies (Han et al., 2010; Schwarzkopf and Boning, 2011; Trenary and Han, 2013) had shown the complexity of the zonal mean vertical temperature structure (upper 700m) in the tropical IO with strong temperature variations within the thermocline layer in the decadal time scale. Although they considered the wind stress forcing over the Indian Ocean was primarily responsible for variations at the thermocline, the contribution of ITF after 1990 was phenomenal. Several previous studies had highlighted this complexity in the decadal scale by showing near surface warming followed by upper-thermocline cooling in the tropics and weaker warming beneath (Barnett et al., 2005;

Pierce et al., 2006; Bindoff et al., 2007). These findings corroborate well with our results of the vertical temperature structure in the decadal time scale. To be precise, our study showed that the cooling was prevalent within the thermocline (between 80 and 150 m) probably because our research domain was restricted to the equatorial ocean whereas the previous studies dealt with the entire tropical Indian Ocean. Moreover, the accelerated western thermocline cooling noticed in our study was probably associated with the global conveyor belt that shoaled in the vicinity of the western equatorial IO bringing cooler water from the deep in the decadal time scale.

7.2.3.3 Linear trends in salinity at the surface

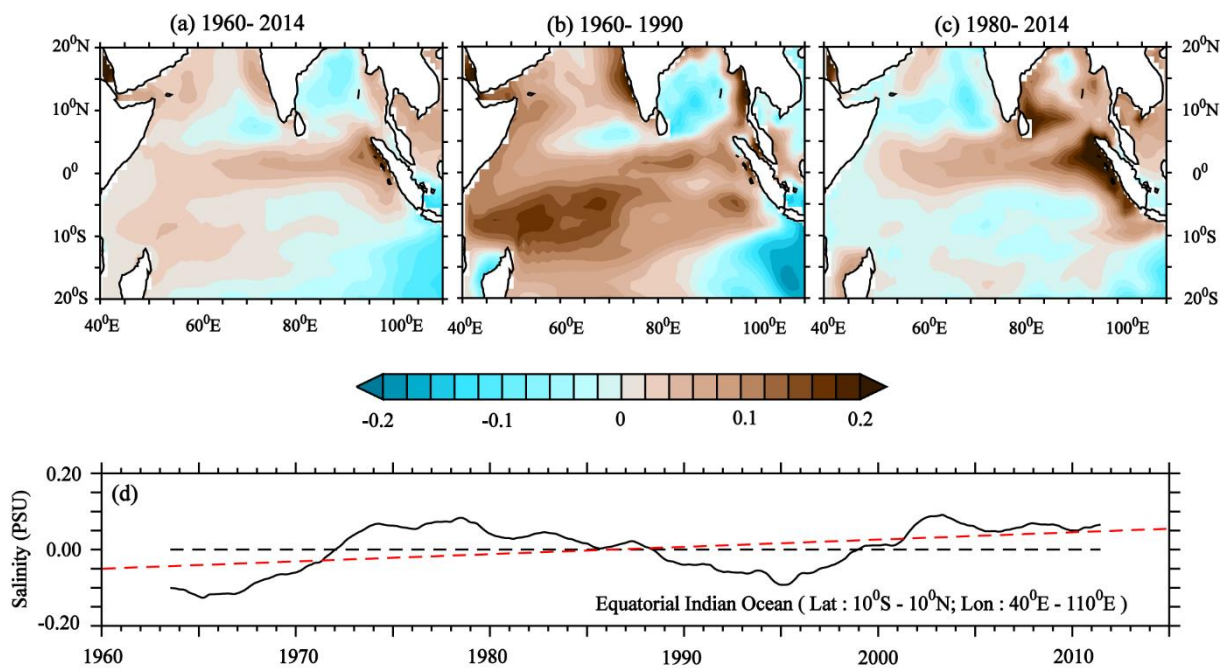


Figure 7.5 Spatial distribution of the slopes of linear trend of surface salinity anomaly determined grid-wise in decadal time scale over the tropical Indian Ocean using ORAS4 model data for the period 1960 – 2014 (a), 1960-1990 (b) and 1980-2014 (c). The linear trend of monthly mean salinity anomaly computed within the equatorial box bounded by 10° N-10° S latitude and 40° E-110° E longitude for the period 1960-2014 (d). Seven year running mean is applied in all cases to remove seasonal and inter annual oscillations to highlight the decadal signals.

Based on the validation result, more precise ORAS4 simulated salinity data had been used to analyse the linear salinity trends at both horizontal (tropical ocean) and vertical (equatorial ocean) salinity fields. The details of data analysis were same as in the case of temperature provided in the previous section. A warming trend of the Indian Ocean was noticed since 1950s

from the upper ocean heat content studies (Levitus et al., 2009; Xue et al., 2012) which got accelerated in 1970s (Hoerling et al., 2012). Observational studies indicated that globally sea surface salinity (SSS) had increased over the past few decades in regions where evaporation exceeds precipitation and decreased in regions where precipitation exceeds evaporation (Roemmich and Gilson, 2009; von Schuckmann et al., 2009; Hosoda et al., 2009; Durack and Wijffels, 2010; Helm et al., 2010). Therefore, the spatial salinity trends were examined at 3 time-windows viz; 1960-2014, 1960-1990 and 1980-2014 to accommodate decades falling in moderate and accelerated warming time zones (Figure 7.5 top panel). However, the SSS exhibited a decreasing trend in the equatorial Indian Ocean, Bay of Bengal (BoB) and Southern Ocean and an increasing trend in subtropical south Indian Ocean and Arabian Sea (AS) (Durack and Wijffels, 2010). These results were in consistent with the notion that saltier regions get saltier and fresher regions get fresher under global warming scenario.

The spatial trend in SSS during 1960-2014 period, on an average, indicated a positive slope all along the equator with slightly steeper ones occupying the eastern equatorial ocean (Figure 7.5a) although the mean linear trend in SSS within the larger equatorial box (10° S- 10° N; 40° E- 110° E) indicated a nominal positive trend of 0.018 PSU/ decade (Figure 7.5b). The slope tends to become negative indicating freshening on either side of the equator. The linear trend analysis from 1960 to 2014 indicated that the AS (BoB), on an average, exhibited a positive (negative) trend of 0.03 (-0.04) PSU/ decade. The contrast was much more severe during the moderate warming period of 1960-1990 with steeper slopes indicating that the surface water of AS and the equatorial waters become more and more saltier (0.18 PSU/ decade) and accelerated freshening (-0.16 PSU/ decade) in southern AS and BoB under the notion of increasing (decreasing) salinity when evaporation (precipitation) exceeds precipitation (evaporation) in the warming climate (Figure 7.5b). However, the results were surprisingly different during the accelerated warming period of 1980-2014 where the trend reversed in AS and BoB (7.5c). In this accelerated warming scenario, AS become more fresher (or less saline) and BoB tend to become saltier with some freshening in the centre in the decadal time scale. There was a distinct difference between eastern and western equatorial oceans where eastern equatorial zone was saltier than the western counterpart. It became difficult to explain these trends of surface salinity during 1980-2014 period based on the conventional knowledge of the dynamics of the north

Indian Ocean in the decadal time scale especially when the conclusions were purely based on the not-so-perfect data from model simulations.

7.2.3.4 Linear trends in salinity at depths

In line with the trend analysed in the vertical temperature field, an attempt had been made to analyse the SSS trend in the surface seven hundred meter water column right across the equator by following the data analysis explained in the previous section to project the variabilities in the decadal scale (Figure 7.6a). The linear trend of average salinity anomaly at the subsurface

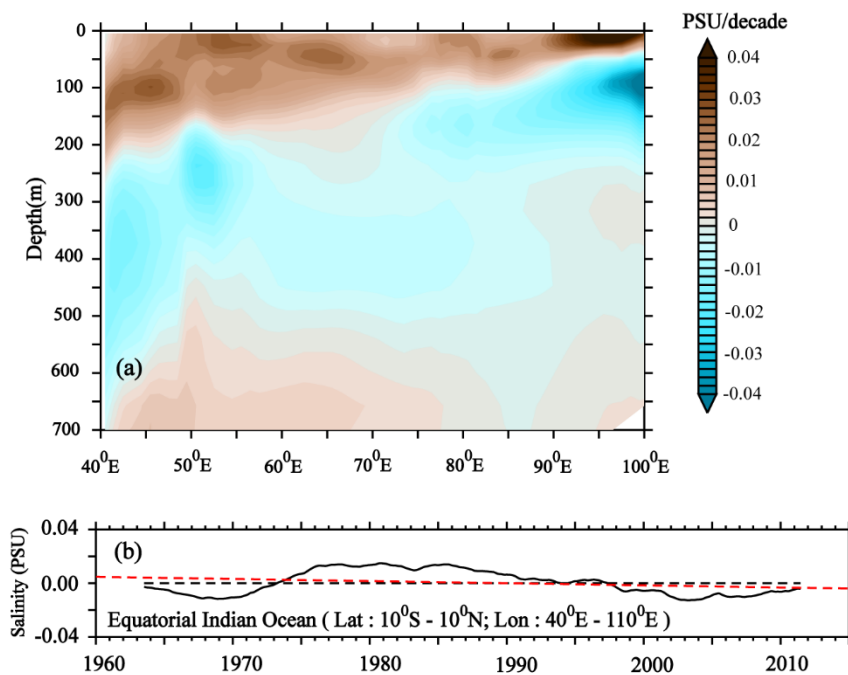


Figure 7.6 Vertical distribution of the slopes of linear trend of salinity anomaly in decadal time scale along the equatorial Indian Ocean by averaging the meridional values using ORAS4 model data for the period 1960 – 2014 (a). The linear trend of monthly mean salinity anomaly (80-150 m) computed within the equatorial box bounded by 10° S-10° N latitude and 40° E-110° E longitude for the period 1950-2014 (b). Seven year running mean is applied to remove seasonal and inter annual oscillations to highlight the decadal signals.

layer (80-150 m) within the thermocline enclosed by larger equatorial box (10° S-10° N; 40° E-110° E) was displayed in Figure 7.6b. The insignificant zonal trend in the decadal scale was the result of averaging the contrasting east-west salinity gradient in the subsurface thermocline (80-150 m layer). The presence of positive and negative slopes occupying western and eastern half of the equatorial ocean within the thermocline exhibited subduction and advection of salinity

anomalies in the decadal time scale (Figure 7.6a). Subduction of positive anomalies in the west and advection of negative anomalies in the east appeared to be linked to the dynamics associated with the surface easterlies that often generated eastward pressure gradient at the thermocline. The zonal spreading of the positive anomalies could be related to the shoaling of thermocline towards east and the presence of negative anomalies close to Sumatra coast could be attributed to the process of upwelling.

Similar freshening at higher latitudes extending downward and equator ward to intermediate depths, primarily through subductions and advection of salinity anomalies in the thermocline in the Indian Ocean in the decadal time scale was reported earlier (Wong et al., 1999; Bindoff and McDougall, 2000; McDonagh et al., 2005; Bindoff et al., 2007; Böning et al., 2008; Roemmich and Gilson, 2009; Durack and Wijffels, 2010).

The SSS trend analysis at both surface and subsurface equatorial Indian Ocean indirectly hinted the dynamics associated with the Indian Ocean Dipole often observed more frequently in a warming climate prevalent in the decadal time scale. However, the linear trend analysis in this time scale indicated eastern equatorial surface water become more saline while the subsurface water tends to become fresher. But the situation was reversed at a lesser rate in the western half of the equatorial Indian Ocean.

Summary and Conclusions

8.1 Summary

In recent years, the dynamics of equatorial Indian Ocean circulation attracted the interest of global scientific community ever since the discovery of Indian Ocean Dipole (IOD), an inter-annual phenomenon associated with the coupled ocean-atmosphere system effecting regional and global climate variability (Saji et al., 1999; Webster et al., 1999). As ENSO on Pacific, the IOD effects on rainfall and atmospheric temperatures caused significant socio-economic impacts, such as on agriculture, wildfires and spread of insects and waterborne diseases affecting particularly the Indian Ocean rim countries (Saji et al., 1999; Hashizume et al., 2013). While, several attempts have been made to understand the variability of zonal surface currents in the Indian Ocean, only a few recent studies had discussed the variability of the subsurface currents (Reppin et al., 1999; Swapna and Krishnan, 2008; Iskandar et al., 2009; Zhang et al., 2014).

The observed surface current record derived from satellite data (i.e. OSCAR; Bonjean and Lagerloef, 2002) was too short (~ 20 years) to confidently differentiate the relative contributions of IOD and ENSO to inter-annual variability because of the strong tendency of these two modes to co-occur. The even shorter observed equatorial current measurements at depth from ADCP data further prevented a thorough description of the inter-annual subsurface current variations in the IO. In this study, we use a ~ 50 -year-long simulation from an eddy permitting ($1/4^\circ$) ocean general circulation model forced with realistic inter-annual air-sea fluxes over the 1958–2007 period to describe the main modes of inter-annual variability of surface and subsurface equatorial zonal currents in the IO and to separate out the respective contribution of ENSO and IOD on these inter-annual fluctuations. We first demonstrate that this model simulation accurately captured the surface and subsurface zonal current variations in the equatorial IO region at both seasonal and inter-annual timescales, including the variability of the Wyrтки jets derived from

satellite data from 1993 and the variability of the seasonally occurring EUCs observed from ADCP from the early 2000.

To provide a general description of the inter-annual variability of the equatorial current system in the IO, we first performed an EOF analysis of both surface and subsurface zonal current inter-annual anomalies in the equatorial IO. This analysis revealed two main modes of equatorial current variability. The dominant mode exhibited maximum variability in fall and largely described the variability of the fall Wyrтки jet intensity. The second mode was maximum in winter and largely described the inter-annual variability of the subsurface currents in winter, with a weaker surface expression. This winter subsurface current variations depicted by the second mode generally follow the fall Wyrтки jet variability depicted by the first mode by 4 to 5 months.

The surface current variability appeared to be directly forced by inter-annual variations of the equatorial zonal winds. These inter-annual zonal current anomalies at the equator tends to lead the zonal wind stress anomalies by 1 month, which had been interpreted by Nagura and McPhaden (2010a) as a response to the reflected Rossby waves radiating from the eastern boundary. In line with Chen et al. (2015), these equatorial zonal wind variations are further shown to induce anomalous tilt of the equatorial thermocline one season ahead through equatorial wave adjustment that further induce zonal pressure gradient changes and subsurface current variations. In line with Zhang et al. (2014), our analysis also showed that thermocline depth anomalies south of equator further contributed to zonal current variations in the equatorial thermocline through meridional geostrophic flows between the off equatorial and the equatorial region within the shallow meridional overturning cells. These off-equatorial thermocline signals were driven by a combination of both equatorial Rossby waves induced by equatorial wind signals and off-equatorial Rossby waves induced by off-equatorial wind curl signals.

The SST, wind and thermocline patterns related to these EOF analyses of the equatorial system were reminiscent of the signature of the combined influence of ENSO and IOD over the IO. However, the strong tendency for IOD and ENSO to co-occur did not allow separating their respective influence. To reach that goal, we further performed partial regression analysis of the

equatorial zonal currents that allowed separating ENSO and IOD influence. Our analysis clearly demonstrated that the IOD was largely responsible for the inter-annual modulation of fall Wyrki jet intensity by modulating the equatorial wind intensity during that season. The IOD was also responsible for strong subsurface current variations a couple of months later (around December) induced by the delayed effect of the IOD wind signal onto the equatorial thermocline and related zonal pressure gradient. The equatorial current system response to ENSO was weaker and delayed compared to that of the IOD. The remote and delayed impact of ENSO in the IO induces equatorial wind variations in winter that modulate the surface current intensity and the intensity of the EUC that seasonally develop during late winter/early spring.

There are two main modes of variability's in equatorial Indian Ocean temperature pattern in the inter-annual time scale. The primary mode is the IOBM associated with ENSO and the secondary mode is associated with IOD. The IOBM was a single mode with more loading in the western Indian Ocean particularly the Arabian Sea. The IOBM strengthened from PRE76 to POST76 (Sun et al., 2019) and explain variability of 31% during PRE76 to 49% during POST76. During PRE76 the ENSO related warming occurred during winter while its peak shifted to spring and summer with increased intensity in POST76. This caused significant climate changes over Asia. Moreover, the vertical mode due to IOBM also showed a strong dipole in the thermocline region POST76, while during PRE76 an opposite mode seen only in the eastern Indian Ocean. The correlation between surface and subsurface modes reduced significantly from PRE76 to POST76. The subsurface signals were manifested at least a month ahead of surface manifestations of IOBM.

The second mode with the Indian Ocean Dipole (IOD) accounted for 28% of SST variability during PRE76 which reduced to 13% POST76 due to the influence of IOD. The positive IOD and ENSO occurred concurrently after the climate shift, whereas such relationship was weak during PRE76. The IOD signals were strongest during September-November during both epochs. The IOD signals were strongest in the thermocline region during both epochs. The correlation between surface and subsurface IOD signals weakened from PRE76 to POST76. The subsurface IOD signals also manifested ahead of surface signal during both epochs.

Using Fisher's transformation (a detailed description is given in the chapter Data and Methods) comparing the correlation analysis between the first/second EOFs and indices revealed that ENSO had strong influence on the equatorial temperature system ($r = 0.8$ for PRE76 and $r = 0.6$ for POST76). As stated in earlier section, before the climate shift the correlation between ENSO index and IOD index was weak and after the climate shift they became stronger. The co-occurring events of ENSO and IOD were less before climate shift and after the climate shift they had been increased considerably. Therefore, it had assumed that one way these facts decreased the strength of ENSO induced basin warming and at the same time it had also increased the strength of IOD induced fall warming after the climate shift.

The warming of tropical ocean in the decadal scale had been noticed since 1950 that had unexpected impact on the climate both within the Indian Ocean rim countries and far away through atmospheric teleconnection (Han et al., 2014). The warming of TIO got accelerated post 1980 period causing the frequency of IOD increased many folds in the decadal time scale. The large-scale warming appeared to weaken the inverse relationship between the Pacific El Niño and Indian Summer Monsoon Rainfall (ISMR) (Krishna kumar et al., 1999) probably due to the shifting of Walker circulation to the maritime continent that appeared to trigger the IOD formation in the decadal time scale. The EOF analysis of both surface and subsurface temperature fields during 1950-2014 periods established the fact that IOD was the prominent mode of variability prevalent in the decadal time scale. The mean pattern of variability of surface temperature (spatial pattern) indicated large positive anomalies off Sumatra coast and weak negative anomalies on the west reminding the characteristics of inter-monsoonal Wyrski jet. But the east-west polarity keeps changing with the fluctuations occurring in the temporal (decadal) scale. The dominant negative PCs during pre-1976 period emphasises the positive dipole patterns at the surface and it appeared to vanish during 1976-1995 period to establish prominence of negative IOD pattern in the decadal time scale. The accelerated warming in the post 1995 period probably triggered the frequent occurrence of IOD in the equatorial IO. The surface pattern was well supported by the leading mode of variability in the subsurface depths with few years overlap at the point of polarity-shift in the temporal component in the decadal time scale. Moreover, the leading PCs of both surface temperature and temperature at depths have significant correlations of 0.60 and 0.89 respectively with the PC's of IOD wind within the equatorial domain.

The significant correlations between the PCs of first EOFs of surface and subsurface salinity anomalies ($r=0.9$) in the decadal time scale prescribes the same mode of variability and the dynamics appears to complement each other. The PCs of both surface and subsurface salinity pattern indicated the dominance of equatorial westerlies (easterlies) during pre-1990 (post-1990) period often associated with negative IOD (positive IOD) derived from the contrasting zonal salinity pattern off Somali and Sumatra coast. The positive (negative) salinity anomalies at the east were sourced to the Arabian Sea (Bay of Bengal and western Pacific) that often carried by the prevailing westerlies (easterlies).

The mean surface temperature anomaly within the equatorial box (10° S- 10° N; 40° E- 110° E) indicated a warming trend of 0.12° C/decade which was higher than the Pacific and Atlantic since 1950s with an accelerated warming in post 1970 period. The eastern half of the equatorial IO was warming (0.018 - 0.24° C/decade) much higher than the western counterpart (0.06 - 0.12° C/decade) during 1950-2014 period in the decadal time scale. The eastern equatorial warming trend, however, intensified between 1950 and 1990 ($>0.24^{\circ}$ C/ decade), on the contrary, it witnessed accelerated cooling ($\sim -0.18^{\circ}$ C/ decade) in the 1980-2014 period especially the south-eastern equatorial Ocean. It is to be noted that the dominant pattern of the equatorial ocean since 1990 was the positive IOD in the decadal time scale where the south-eastern equatorial ocean was encompassed by cool upwelled water by the prevailing easterly winds.

The surface warming was restricted to only surface 50m depth at the west and gradually spreading downward to 100m at the east in the decadal scale with signs of accelerated warming (0.18° C/ decade) east of 70° E. On the other hand, the subsurface layer (80-150m) appears to be cooling in the decadal scale with accelerated cooling (-0.18° C/ decade) at the western equatorial IO. The slight warming of the intermediate layer below the thermocline especially west of 80° E was also observed in the decadal scale. Moreover, the accelerated western thermocline cooling noticed in our study is probably associated with the global conveyor belt that shoals in the vicinity of the western equatorial IO bringing cooler water from the deep in the decadal time scale.

Observational studies indicated that globally sea surface salinity (SSS) had increased over the past few decades in regions where evaporation exceeds precipitation and decreased in regions where precipitation exceeds evaporation (Hosoda et al., 2009; Durack and Wijffels, 2010; Helm et al., 2010). The spatial trend in SSS during 1960-2014 periods, on an average, indicated a positive slope all along the equator with slightly steeper ones occupying the eastern equatorial ocean. The linear trend analysis from 1960 to 2014 indicated that the AS (BoB), on an average, exhibited a positive (negative) trend of 0.03 (-0.04) PSU/ decade. The contrast was much more severe during the moderate warming period of 1960-1990 with steeper slopes indicating that the surface water of AS and the equatorial waters become more and more saltier (0.18 PSU/ decade) and accelerated freshening (-0.16 PSU/ decade) in southern AS and BoB under the notion of increasing (decreasing) salinity when evaporation (precipitation) exceeds precipitation (evaporation) in the warming climate.

In line with the trend analysis carried out in the vertical temperature field, an attempt has been made to study the SSS trend in the surface seven hundred meter water column across the basin in the decadal time scale. The presence of subsurface positive and negative slopes occupying western and eastern half of the equatorial ocean within 50-200 m layer exhibited subduction and advection of salinity anomalies in the decadal time scale. Subduction of positive anomalies in the west and advection of negative anomalies in the east appeared to be linked to the dynamics associated with the surface easterlies that often generate eastward pressure gradient at the thermocline. The zonal spreading of the positive anomalies could be related to the shoaling of thermocline towards east and the presence of negative anomalies close to Sumatra coast could be attributed to the process of upwelling. The SSS trend analysis at both surface and subsurface equatorial Indian Ocean indirectly hints the dynamics associated with the Indian Ocean Dipole often observed more frequently in a warming climate prevalent in the decadal time scale.

8.2 Concluding remarks

- Several previous studies have already documented the impact of IOD events occurring in the equatorial current system. Our results confirmed previous published literature on the IOD influence on fall surface currents in the equatorial IO, i.e. the intensity reduction

(intensification) of the fall Wyrтки surface jet in response to positive (negative) IODs through their control on fall equatorial wind intensity. Our result also supported the belief that the IOD event seldom affects the Wyrтки jet intensity. The strong correlations found between the two main modes of equatorial subsurface current variations in fall and winter and the IOD index (resp. 0.82 and 0.75) further demonstrated that IOD events control most of the equatorial current variability in these seasons. The originality of the present study had been to assess the specific remote impact of ENSO on the equatorial current system, by virtue of the long-term model integration that allowed disentangling of the respective influence of the often co-occurring ENSO and IOD events. Because of the delayed ENSO signature in the IO, our results showed that ENSO hardly influence the maximum intensity of the fall Wyrтки jet. This result somewhat contradicted results from Gnanaseelan et al. (2012), who suggested that ENSO forcing contribute to the fall Wyrтки jet intensity variations in the eastern part of the basin. We rather found a delayed influence of ENSO, which related to winter wind signature that induced surface current variations during that season. While the IOD influence does not extend into the following year, our results revealed that a significant ENSO influence into the following year, with ENSO forcing modulating the inter-annual variability of the late winter/early spring EUC induced by the delayed effect of the ENSO wind signal onto the equatorial zonal pressure gradient in that season.

- At the surface, the IOBM strengthened from PRE76 to POST76 and explain variability of 31% during PRE76 to 49% during POST76. During PRE76 the ENSO related warming occurred during winter while its peak shifted to spring and summer with increased intensity in POST76. The subsurface expression of IOBM also showed a strong dipole pattern in the thermocline region POST76, while during PRE76 the dipole pattern was absent and a singular mode was seen in the eastern Indian Ocean. The correlation between surface and subsurface modes reduced significantly from PRE76 to POST76. The subsurface signals were manifested at least a month ahead of surface manifestations of IOBM.

- The second mode accounted for 28% of SST variability during PRE76 which reduced to 13% POST76 due to the influence of IOD. The positive IOD and ENSO occurred concurrently after the climate shift, whereas such relationship was weak during PRE76. The IOD signals were strongest during September-November during both epochs. The correlation between surface and subsurface IOD signals weakened from PRE76 to POST76. The subsurface IOD signals also manifested ahead of surface signal during both epochs.
- Before the climate shift the correlation between ENSO and IOD indices was weak and after the climate shift they became stronger. The co-occurring events of ENSO and IOD were less before climate shift and after the climate shift they increased considerably. Decreased strength of ENSO induced basin scale warming during PRE76 era and at the same time increased the strength of IOD induced fall warming after the climate shift.
- Evolution of zonal SST structure in the decadal time scale indicated that the mean pattern of variability at the equatorial IO was the eastern (western) equatorial warming (cooling) and was more prevalent during 1976-95 periods when the descending walker cell moved to the west. The subsurface temperature patterns also corroborated well with these dynamics during this period in the decadal time scale. Therefore, the Wyrтки Jet intensification (negative IOD) is the mean pattern of variability during this period.
- However, the polarity reversed prior to 1976 and post 1995 periods due to the prevailing easterlies when the descending branch of walker cell migrated to the maritime continent. This brought upwelling at the Sumatra coast and down welling off Somalia. At depths, the warmer thermocline at west appeared to shoal towards east causing upwelling off Sumatra coast during these periods corroborated with the surface dynamics. Therefore, the Wyrтки Jet reduction (positive IOD) is the mean pattern of variability during this period.

- The surface and subsurface salinity variability in the decadal time scale supported the dynamics explained in the temperature field. As the strong correlation between the PCs ($r=0.9$) of horizontal and vertical field indicated both EOFs were related to the same mode of variability, the contours of positive anomaly that appeared to shoal eastward could be associated with the subsurface manifestation of the surface IOD pattern. The pre-1990 (post-1990) salinity structure, however, substantiate the dynamics associated with the Wyrтки Jet intensification (Wyrтки Jet reduction) during a negative (positive) IOD event.
- The mean surface temperature anomaly within the equatorial box indicated a warming trend of $0.12\text{ }^{\circ}\text{C}$ per decade which was higher than the Pacific and Atlantic since 1950s with an accelerated warming in post 1970 period. The eastern half of the equatorial IO is warming ($0.018\text{-}0.24\text{ }^{\circ}\text{C}/\text{decade}$) much higher than the western counterpart ($0.06\text{-}0.12\text{ }^{\circ}\text{C}/\text{decade}$) during 1950-2014 period in the decadal time scale. The eastern equatorial warming trend, however, intensified between 1950 and 1990 ($>0.24\text{ }^{\circ}\text{C}/\text{decade}$), on the contrary, it witnessed accelerated cooling ($\sim -0.18\text{ }^{\circ}\text{C}/\text{decade}$) in the 1980-2014 period especially the south-eastern equatorial Ocean. On the other hand, the subsurface layer (80-150m) appears to be cooling in the decadal scale with accelerated cooling ($-0.18\text{ }^{\circ}\text{C}/\text{decade}$) at the western equatorial IO.
- The spatial trend in SSS during 1960-2014 periods, on an average, indicated a positive slope all along the equator with slightly steeper ones occupying the eastern equatorial ocean. The contrast was much more severe during the moderate warming period of 1960-1990 with steeper slopes indicating that the surface water of AS and the equatorial waters become more and more saltier ($0.18\text{ PSU}/\text{decade}$) and accelerated freshening ($-0.16\text{ PSU}/\text{decade}$) in southern AS and BoB under the notion of increasing (decreasing) salinity when evaporation (precipitation) exceeds precipitation (evaporation) in the warming climate.

8.3 Future Programs

We have come across several issues while addressing the variability and trends of both temperature and salinity at the surface and at depths in the decadal time scale. As we depend heavily on model simulations to address the variability and trends in the decadal scale, proper validation of the model is essential to derive meaningful conclusions. Some model appeared to be capturing variability in the temperature field while other models compare well with the salinity structure. But all model simulations investigated somehow fared poorly with the comparisons made at the thermocline ridge regions due to unknown reason. We thought this case is to be taken up for future work.

Similarly, the salinity trend analysis over the TIO revealed a peculiar pattern of salinity trend especially over AS, BoB and eastern periphery of the equatorial IO during the accelerated warming period of 1980-2014. During this period, a negative (positive) trend in salinity was observed over AS (BoB) that make AS fresher and BoB saltier which was difficult to explain at this point of time and hence considered for taking up under the future programs.

It is just out of curiosity, we decided to study the impact of Pacific Decadal Oscillation on the temperature variability at the EIO in the multi-decadal time scale. An in-depth study is also planned to understand the driving mechanisms behind the EIO thermocline oscillation observed in the decadal time scale.

With this in mind, following scientific questions are formulated, which intended to address as future work of this Ph.D. program.

- Is there any impact of Pacific Decadal Oscillation on temperature at the EIO?
- The role of air-sea interaction and advection at the thermocline ridge region of the southwest equatorial Indian Ocean on the modulation of equatorial currents in the decadal time scale.
- The main driving mechanisms behind the EIO thermocline oscillations observed on the decadal time scale?
- A revisit on the positive and negative salinity trends in the Bay of Bengal and Arabian Sea respectively during the accelerated warming period of 1980-2014.

References

Akhil V. P., F. Durand, M. Lengaigne, J. Vialard, M.G. Keerthi, V.V. Gopalakrishna, C. Deltel, F. Papa, C. de Boyer Montégut (2014) A modeling study of the processes of surface salinity seasonal cycle in the Bay of Bengal, *J. Geophys. Res.*, 116, 3926-3947, doi: 10.1002/2013JC009632

Akhil, V. P., M. Lengaigne, J. Vialard, F. Durand, M. G. Keerthi, A. V. S. Chaitanya, F. Papa, V. V. Gopalakrishna, and C. de Boyer Montegut (2016) A modeling study of processes controlling the Bay of Bengal sea surface salinity interannual variability, *J. Geophys. Res. Oceans*, 121, 8471–8495, doi: 10.1002/2016JC011662.

Alexander, M. A., Bladé, I., Newman, M., Lanzante, J. R., Lau, N. C., and Scott, J. D(2002) The atmospheric bridge: The influence of ENSO teleconnections on air–sea interaction over the global oceans, *J. Climate*, 15, 2205–2231

Alexander, M. A., Lau, N. C. and Scott, J. D (2004) Broadening the atmospheric bridge paradigm: ENSO teleconnections to the tropical West Pacific-Indian Oceans over the seasonal cycle and to the North Pacific in summer. *Earth Climate: The Ocean-Atmosphere Interaction*, *Geophys. Monogr.*, 147, Amer. Geophys. Union, 85–103

Allan, R., D. Chambers, W. Drosowsky, H. Hendon, M. Latif, N. Nicholls, I. Smith, R. Stone, and Y. Tourre (2001) Is there an Indian Ocean dipole, and is it independent of the El Niño–Southern Oscillation?, *CLIVAR Exchanges*, 6, 18–22

Alory, G., G. Meyers (2009) Warming of the upper equatorial Indian Ocean and changes in the heat budget (1960-99), *J. Climate*, 22, 93- 113, doi: 10.1175/2008JCLI12330.1

Alory, G., S. Wijffels, and G. Meyers (2007) Observed temperature trends in the Indian Ocean over 1960 –1999 and associated mechanisms, *Geophys. Res. Lett.*, 34, L02606, doi: 10.1029/2006GL028044

Annamalai, H., J. Potemra, R. Murtugudde, and J. P. McCreary (2005b) Effect of preconditioning on the extreme climate events in the tropical Indian Ocean, *J. Climate*, 18, 3450– 3469

Annamalai, H., and Liu, P. (2005) Response of the Asian summer monsoon to changes in El Nino properties, *Q. J. R. Meteorol. Soc.*, 131, 805

Annamalai, H., R. Murtugudde, J. Potemra, S. P. Xie, P. Liu, and B. Wang (2003) Coupled dynamics over the Indian Ocean: Spring initiation of the zonal mode, *Deep Sea Res., Part II*, 50, 2305–2330

Annamalai, H., S. P. Xie and J. P. McCreary (2005a) Impact of Indian Ocean sea surface temperature on developing El Nino, *J. Climate*, 18, 302-319

Antonov, J. I., Locarnini, R. A., Boyer, T. P., Mishonov, A. V and Garcia, H. E (2006) World Ocean Atlas 2005, Volume 2:Salinity.NOAA Atlas NESDIS 62, NOAA, U.S. Government Printing Office, Washington D.C.

Antony, M. K., and Y. K. Somayajulu (2002) Surface currents in the equatorial Indian Ocean during spring and fall-an altimetry based analysis, *PORSEC BALI Proceedings*, 51-53

Ashok, K., S. K. Behera, S. A. Rao, H. Weng, and T. Yamagata (2007) El Niño Modoki and its possible teleconnection, *J. Geophys. Res.*, 112, doi:10.1029/2006JC003798

Ashok, K., Z. Guan, and T. Yamagata (2001) Impact of the Indian Ocean dipole on the relationship between the Indian monsoon rainfall and ENSO, *Geophys. Res. Lett.*, 28, 4499–4502, doi:10.1029/2001GL013294

Ashok, K., Guan, Z.Y., Saji, N.H., and T. Yamagata (2004) Individual and combined influences of ENSO and the Indian Ocean Dipole on the Indian summer monsoon, *J. Climate*, 17, 3141-3155

- Ashok, K., and Saji, N.H (2007) On the impacts of ENSO and Indian Ocean dipole events on sub- regional Indian summer monsoon rainfall, *Nat. Hazards*, 42, 273–285, <https://doi.org/10.1007/s11069-006-9091-0>
- Atlas, R., Hoffman, R., Bloom, S., Jusem, J., and Ardizzone, J(1996) A multi-year global surface wind velocity dataset using SSM/I wind observations, *Bull. Am. Meteorol. Soc.*, 77, 869–882
- Baquero-Bernal, A., M. Latif, and S. Legutke (2002) On dipole like variability of sea surface temperature in the tropical Indian Ocean, *J. Climate*, 15, 1358–1368
- Barnett, T. P., D. W. Pierce, K. M. Achuta Rao, P. J. Gleckler, B. D. Santer, J. M. Gregory, and W. M. Washington (2005) Penetration of human-induced warming into the world's oceans, *Science*, 309, 284–287, doi:10.1126/science.1112418
- Behera, S. K., J.-J. Luo, S. Masson, P. Delecluse, S. Gualdi, A. Navarra, and T. Yamagata (2005) Paramount impact of the Indian Ocean Dipole on the East African short rains: A CGCM study, *J. Climate*, 18, 4514–4530, doi:10.1175/JCLI3541.1
- Bhat, G. S., and Coauthors (2001) BOBMEX: The Bay of Bengal Monsoon Experiment, *Bull. Am. Meteorol. Soc.*, 82, 2217–2243
- Bindoff, N. L., and T. J. McDougall (2000) Decadal changes along an Indian Ocean section at 32°S and their interpretation, *J. Phys. Oceanogr.*, 30, 1207–1222, doi:10.1175/1520-0485(2000)0302.0.CO;2
- Bindoff, N.L., and Coauthors (2007) Observations: Oceanic climate change and sea level. *Climate Change 2007: The Physical Science Basis*, S. Solomon et al., Eds., Cambridge University Press, 385–432

- Bjerknes, J (1966) A possible response of the atmospheric Hadley circulation to equatorial anomalies of ocean temperature, *Tellus*, 18, 820–9
- Bjerknes, J (1969) Atmospheric teleconnections from the equatorial Pacific, *Mon. Weather Rev.*, 97, 163–172, 1969
- Bonjean, F., and G. S. E. Lagerloef (2002) Diagnostic model and analysis of the surface currents in the tropical Pacific Ocean, *J. Phys. Oceanogr.*, 32, 2938–2954
- Böning, C. W., A. Dispert, M. Visbeck, S. R. Rintoul, and F. U. Schwarzkopf (2008) The response of the Antarctic Circumpolar Current to recent climate change, *Nat. Geosci.*, 1, 864–869, doi:10.1038/ngeo362
- Brodeau, L., Barnier, B., Treguier, A. M., Penduff, T., Gulev, S (2010) An ERA 40-based atmospheric forcing for global ocean circulation models, *Sci.Direct*, 31, 88–104, doi:10.1016/j.ocemod.2009.10.005
- Bubnov, V. A (1994) Climatic zonal pressure gradient in the equatorial zone of the Indian Ocean, *Oceanology*, 33, 414-420
- Cai, W., P. van Rensch, T. Cowan, and H. H. Hendon (2011) Teleconnection pathways of ENSO and the IOD and the mechanisms for impacts on Australian rainfall, *J. Climate*, 24, 3910–3923
- Cai, W., X. T. Zheng, E. Weller, M. Collins, T. Cowan, M. Lengaigne, W. Yu, and T. Yamagata (2013) Projected response of the Indian Ocean Dipole to greenhouse warming, *Nat. Geosci.*, 6, 999–1007
- Cane, M. A (1980) On the dynamics of equatorial currents, with application to the Indian Ocean, *Deep Sea Res., Part A*, 27, 525–544, doi:10.1016/0198-0149(80)90038-2

- Carton, J. A., G. Chepurin, X. Cao, and B. Giese (2000) A simple ocean data assimilation analysis of the global upper ocean 1950–95. Part I: Methodology, *J. Phys. Oceanogr.*, 30, 294–309
- Chambers, D. P., Tapley, B. D., Stewart, R. H (1999) Anomalous warming in the Indian Ocean coincident with El Niño, *J. Geophys. Res.*, 104:3035–3047
- Chen, G., W. Han, Y. Li, D. Wang, and M. McPhaden (2015) Seasonal-to-Interannual Time Scale Dynamics of the Equatorial Undercurrent in the Indian Ocean, *J. Phys. Oceanogr.*, 45, 1532-1553, doi: <http://dx.doi.org/10.1175/JPO-D-14-0225.1>
- Chowdary, J. S., and Gnanaseelan, C (2007) Basin-wide warming of the Indian Ocean during El Niño and Indian Ocean dipole years, *Int. J. Climatology*, 27 (11):1421-1438
- Chowdary, J. S., Parekh, A., Sayantani, O., Gnanaseelan, C (2015) Role of upper ocean processes in the seasonal SST evolution over tropical Indian Ocean in Climate Forecasting System, *Climate Dyn.*, doi: 10.1007/s00382-015-2478-4
- Cravatte S., Madec G., Izumo T., Menkes C., Bozec, A (2007) Progress in the 3-D circulation of the eastern equatorial Pacific in a climate ocean model, *Ocean Model*, 17, 28– 48, doi:10.1016/j.ocemod.2006.11.003
- Dee, D. P., S. M. Uppala, A. J. Simmons, P. Berrisford, P. Poli, S. Kobayashi, U. Andrae, M. A. Balmaseda, G. Balsamo, P. Bauer, P. Bechtold, A. C. M. Beljaars, L. van de Berg, J. Bidlot, N. Bormann, C. Delsol, R. Dragani, M. Fuentes, A. J. Geer, L. Haimberger, S. B. Healy, H. Hersbach, E. V. Hólm, L. Isaksen, P. Kåll-berg, M. Köhler, M. Matricardi, A. P. McNally, B. M. Monge-Sanz, J.-J. Morcrette, B.-K. Park, C. Peubey, P. de Rosnay, C. Tavolato, J.-N. Thépaut, and F. Vitart (2011) The ERA-Interim reanalysis: configuration and performance of the data assimilation system, *Q. J. R. Meteorol. Soc.*, 137, 553–597

Du, Y., and S. P. Xie (2008) Role of atmospheric adjustments in the tropical Indian Ocean warming during the 20th century in climate models, *Geophys. Res. Lett.*, 35, L08712, doi:10.1029/2008GL033631

Du, Y., Xie, S.-P., Huang, G., and Hu, K (2009) Role of air– sea interaction in the long persistence of El Niño–induced north Indian Ocean warming, *J. Climate*, 22, 2023–2038, doi:10.1175/2008JCLI2590.1

Durack, P. J., and S. Wijffels (2010) Fifty-year trends in global ocean salinities and their relationship to broad-scale warming, *J. Climate*, 23, 4342–4362, doi:10.1175/2010JCLI3377.1

England, M. H., and F. Huang (2005) On the interannual variability of the Indonesian Through flow and its linkage with ENSO, *J. Climate*, 18, 1435–1444

Ffield, A., and A. L. Gordon (1992) Vertical mixing in the Indonesian thermocline, *J. Phys. Oceanogr.*, 22, 184–195

Findlater, J (1969) A major low-level air current near the Indian Ocean during the northern summer, *Q. J. R. Meteorol. Soc.*, 95, 404, doi.org/10.1002/qj.49709540409

Fischer, A., P. Terray, E. Guilyardi, S. Gualdi, and P. Delecluse (2005) Two independent triggers for the Indian Ocean Dipole/Zonal Mode in a coupled GCM, *J. Climate*, 18, 3428– 3449

Gadgil, S., Joseph, P. V., Joshi, N.V (1984) Ocean-atmosphere coupling over monsoon regions *Nature*, *Nature*, 312, 141-143, doi: 10.1038/312141a0

Gadgil, S., Vinaychandran, P. N., Francis, P. A., and Siddhartha, G. (2004) Extremes of Indian summer monsoon rainfall, ENSO, equatorial Indian Ocean Oscillation, *Geophys. Res. Lett.*, 31, doi: 10.1029/2004GL019733

- Ganachaud, A., C. Wunsch, and J. Marotzke (2000) The meridional overturning and large-scale circulation of the Indian Ocean, *J. Geophys. Res.*, 105, 26,117–26,134
- Gill, A. E., (1980) Some simple solutions for heat induced tropical calculation, *Q. J. R. Meteorol. Soc.*, 106, 447- 462
- Gill, A.E., (1982) *Atmosphere and Ocean Dynamics*, Academic Press, New York
- Gnanaseelan, C., Deshpande, A., McPhaden, M. J (2012) Impact of Indian Ocean Dipole and El Niño/Southern Oscillation wind-forcing on the Wyrтки jets, *J. Geophys. Res.*, 117, C08005, 2012
- Gnanaseelan, C, Roxy, M. K., Deshpande, A., (2017) Variability and trends of sea surface temperature and circulation in the Indian Ocean, *Springer Geology*, *Observed climate variability and change over the Indian Ocean*, doi: 10.1007/978-981-10-2531-0_10
- Godfrey, J. S., Johnson, G. C., McPhaden, M. J., Reverdin, G. & Wijffels, S (2001) The tropical ocean circulation, In *Ocean circulation and climate* (ed. J. Church, J. Gould & G. Siedler), pp. 215–245. Academic
- Gordon, A. L (2005) Oceanography of the Indonesian seas and their through flow, *Oceanography*, 18, 14–27
- Grodsky, S. A., J. A. Carton, R., Murtugudde (2001) Anomalous surface currents in the tropical Indian Ocean, *Geophys. Res. Lett.*, 28, No.22, 4207-4210
- Guo, F., Q. Liu, J. Yang, and L. Fan (2018) Three types of Indian Ocean basin modes, *Climate Dyn.*, 51, 4357–4370, doi.org/10.1007/s00382-017-3676-z
- Han, W., and J. P. McCreary (2001) Modelling salinity distributions in the Indian Ocean, *J. Geophys. Res.*, 106, 859–877

Han, W., P.J. Webster, R. Lukas, P. Hacker, and A. Hu (2004) Impact of atmospheric intraseasonal variability in the Indian Ocean: low-frequency rectification in equatorial surface current and transport, *J. Phys. Oceanogr.*, 34, 1350-1372

Han, W., Meehl, G., Rajagopalan, B. et al., (2010) Patterns of Indian Ocean sea-level change in a warming climate, *Nat. Geosci.*, 3, 546–550, doi:10.1038/ngeo901

Han, W., Meehl, G., Hu, A., Alexander, M., Yamagata, T., Yuan, D et al., (2014) Intensification of decadal and multi-decadal sea level variability in the western tropical Pacific during recent decades, *Climate Dyn.*, 43, 1357–1379. doi:10.1007/s00382-013-1951-1

Han, W., J. Vialard, M. J. McPhaden, T. Lee, Y. Masumoto, M. Feng, and W. P. M. de Ruijter (2014) Indian Ocean decadal variability: A review, *Bull. Am. Meteorol. Soc.*, 95, 1679–1703, doi: 10.1175/BAMS-D-13-00028.1

Hashizume, M., L. F. Chaves, A. S. G. Faruque, M. Yunus, K. Streatfield, and K. Moji (2013) A differential effect of Indian Ocean Dipole and El Niño on cholera dynamics in Bangladesh, *PLoS ONE*, 8(3), e60001, doi:10.1371/journal.pone.0060001

Hastenrath, S (2002) Dipoles, temperature gradients, and tropical climate anomalies, *Bull. Am. Meteorol. Soc.*, 83, 735-738

Helm, K. P., N. L. Bindoff, and J. A. Church (2010) Changes in the global hydrological-cycle inferred from ocean salinity, *Geophys. Res. Lett.*, 37, L18701, doi: 10.1029/2010GL044222

Hermes, J.C., and C. J. C. Reason (2008) Annual cycle of the South Indian Ocean (Seychelles-Chagos) thermocline ridge in a regional ocean model, *J. Geophys. Res.*, 113, C04035, doi: 10.1029/2007JC004363

Hoerling, M., J. Eischeid, J. Perlwitz, X. Quan, T. Zhang, and P. Pegion (2012) On the increased frequency of Mediterranean drought, *J. Climate*, 25, 2146–2161, doi:10.1175/JCLI-D-11-00296.1

- Hoerling, M., and A. Kumar, T. Xu, G. Bates, and A. Phillips (2004) Twentieth century North Atlantic climate change. Part II: Understanding the effect of Indian Ocean warming, *Climate Dyn.*, 23, 391–405, doi: 10.1007/s00382-004-0433-x
- Hoskins, B. J., and D. J. Karoly (1981) The steady linear response of a spherical atmosphere to thermal and orographic forcing, *J. Atmos. Sci.*, 38, 1179-1196
- Hosoda, S, T. Suga, N. Shikama, and K. Mizuno (2009) Global surface layer salinity change detected by Argo and its implication for hydrological cycle intensification, *J. Oceanogr.*, 65, 579–586, doi: 10.1007/s10872-009-0049-1
- Huang, B., Shin, C. S., Shukla, J., Marx, L., Balmaseda, M. A., Halder, S., et al. (2017) Reforecasting the ENSO events in the past 57 years (1958–2014), *J. Climate*, 30(19), 7669–7693, doi: 10.1175/JCLI-D-16-0642.1
- Ihara, C., Kushnir, Y., Cane, M.A (2008) Warming trend of the Indian Ocean SST and Indian Ocean dipole from 1880 to 2004, *J. Climate*, 21, 2035–2046
- Iizuka, S., T. Matsuura, and T. Yamagata (2000) The Indian Ocean SST dipole simulated in a coupled general circulation model, *Geophys. Res. Lett.*, 27, 3369– 3372
- Iskander, I., I., Masumoto, Y., and Mizuno, K (2009) Subsurface equatorial zonal current in the eastern Indian Ocean, *J. Geophys. Res.*, 114, C06005, doi:10.1029/2008JC005188
- Izumo, T., J. Vialard, M. Lengaigne, C. de Boyer Montégut, S. K. Behera, J-J. Luo, S. Cravatte, S. Masson and T. Yamagata (2010) Influence of the Indian Ocean Dipole on following year's El Niño, *Nat. Geosci.*, 3, 168-172

Izumo, T., M. Lengaigne, J. Vialard, G. Madec, S. K. Behera and T. Yamagata (2013) Influence of Indian Ocean Dipole and Pacific recharge on following year's El Niño: inter-decadal robustness, *Climate Dyn.*, 42, 291:310, doi:10.1007/s00382-012-1628-1

Jensen, T. G. (2003) Cross-equatorial pathways of salt and tracers from the northern Indian Ocean: Modelling results, *Deep Sea Res., Part II*, 50, 2111–2128

Joseph, S., A. J. Wallcraft, T. G. Jensen, M. Ravichandran, S. S. C. Shenoi, and S. Nayak (2012) Weakening of spring Wyrтки jets in the Indian Ocean during 2006–2011, *J. Geophys. Res.*, 117, C04012, doi: 10.1029/2011JC007581

Kalnay, E., et al. (1996) The NCEP/NCAR 40-year reanalysis project, *Bull. Am. Meteorol. Soc.*, 77, 437–471

Keerthi, M.G (2017) Mixed layer depth in tropical Indian Ocean: Intra seasonal to inter decadal variability and influence of Chlorophyll variations, PhD thesis, Goa University, India

Keerthi, M.G., M. Lengaigne, J. Vialard, C. de Boyer Montégut, P. M. Muraleedharan (2013) Interannual variability of the Tropical Indian Ocean mixed layer depth, *Climate Dyn.*, 40:743–759

Keerthi, M. G., M. Lengaigne, K. Drushka, J. Vialard, C. de Boyer Montégut, M. Levy, P. M. Muraleedharan (2016) Intraseasonal variations of the mixed layer depth in the Indian Ocean, *Climate Dyn.*, 46(7), 2633-2655, doi: 10.1007/s00382-015-2721-z

Kinter, J. L., K. Miyakoda and S. Yang (2002) Recent changes in the connection from the Asian Monsoon to ENSO, *J. Climate*, 15, 1203-1215

Kinter, J. L., M. J. Fennessy, V. Krishnamurthy, and L. Marx (2004) An evaluation of the apparent inter-decadal shift in the tropical divergent circulation in the NCEP-NCAR reanalysis, *J. Climate*, 17, 349-361

Klein, S. A., Soden, B. J., Lau, N. C (1999) Remote sea surface temperature variations during ENSO: evidence for a tropical atmospheric bridge, *J. Climate*, 12,917–932

Köhl, A (2015) Evaluation of the GECCO2 Ocean Synthesis: Transports of Volume, Heat and Freshwater in the Atlantic, *Q. J. R. Meteorol. Soc.*, 141(686), 166-181, doi: 10.1002/qj.2347

Koch-Larrouy, A., G. Madec, P. Bouruet-Aubertot, T. Gerkema, L. Bessie`res, and R. Molcard (2007) On the transformation of Pacific Water into Indonesian Through flow Water by internal tidal mixing, *Geophys. Res. Lett.*, 34, L04604, doi:10.1029/2006GL028405

Krishna Kumar, K., Rajagopalan, K. B., Cane, M. A (1999) On the weakening relationship between the Indian monsoon and ENSO, *Science*, 284, 2156–2159

Krishnan, R., and P. Swapna (2009) Significant influence of the boreal summer monsoon flow on the Indian Ocean response during dipole events, *J. Climate.*, 22, 5611–5634, doi: 10.1175/2009JCLI2176.1

Krishnamurti, T. N (1985) Summer Monsoon Experiment: A review, *Mon. Weather Rev.*, 113, 1590–1626

Krishnamurthy, V., and B. P. Kirtman (2003) Variability of the Indian Ocean: Relation to monsoon and ENSO, *Quart. J. Roy. Meteor. Soc.*, 129, 1623–1646

Lagerloef, G. S. E., G. T. Mitchum, R. Lukas, and P. P. Niiler (1999) Tropical Pacific surface currents estimated from altimeter, wind and drifter data, *J. Geophys. Res.*, 104, 23313–23326

Lakshmi, A. S. N., V. S. N. Murty, R. Murtugudde, M. Anil Kumar, M. S. S. Sarma, Y. Agarvadekar, and A. Almeida (2007) Semi-annual variability in the observed and OGCM simulated zonal currents in the equatorial Indian Ocean, *Proc. Celebrating the Monsoon: An Int. Monsoon Conf.*, Bangalore, India, Indian Institute of Science, pp 11

Lau, N. C., and M. J. Nath (1996) The role of the atmospheric bridge in linking tropical Pacific ENSO events to extra tropical SST anomalies, *J. Climate*, 9, 2036–2057

Lau, N.C., Nath, M.J (2000) Impact of ENSO on the variability of the Asian-Australian monsoons as simulated in GCM experiments, *J. Climate*, 13 (24):4287-4309

Leetmaa, A., and H. M. Stommel (1980) Equatorial current observations in the western Indian Ocean in 1975 and 1976, *J. Phys. Oceanogr.*, 10, 258-269

Lengaigne M., Boulanger, J. P., Menkes, C., Spencer, H (2006) Influence of the seasonal cycle on the termination of El Nino events in a coupled general circulation model, *J. Climate*, 19, 1850–1868, doi: 10.1175/JCLI3706.1

Lengaigne, M., and Vecchi, G. A. (2009) Contrasting the termination of moderate and extreme El Niño events in coupled general circulation models, *Climate Dyn.*, 35, 299–313

Lengaigne, M., Haussman, U., Madec, G., Menkes, C., Vialard, J., Molines, J. M (2012) Mechanisms controlling warm water volume interannual variations in the equatorial Pacific: diabatic versus adiabatic processes, *Climate Dyn.*, 38, 1031–1046

Levitus, S. (1998) Climatological atlas of the world ocean, Tech. Rep. 13, NOAA, Silver Spring, Md

Levitus, S., J. I. Antonov, T. P. Boyer, R. A. Locarnini, H. E. Garcia, and A. V. Mishonov, (2009) Global ocean heat content 1955–2008 in light of recently revealed instrumentation problems, *Geophys. Res. Lett.*, 36, L07608, doi:10.1029/2009GL039847

Lumpkin, R., and K. Speer (2007) Global ocean meridional over-turning, *J. Phys. Oceanogr.*, 37, 2550–2562.

- Luo, J.-J., S. Masson, S. Behera, and T. Yamagata (2007), Experimental forecasts of the Indian Ocean dipole using a coupled OAGCM, *J. Climate*, 20, 2178–2190
- Luo J-J, Zhang R, S. Behera, Y. Masumoto, Jin F-F, Lukas R, T. Yamagata (2010) Interaction between El Niño and extreme Indian Ocean Dipole. *J Climate*, 23:726–742
- Luyten, J. R., and D. H. Roemmich (1982) Equatorial currents at semi-annual period in the Indian Ocean, *J. Phys. Oceanogr.*, 12, 406-413
- Madden, R. A., and P. R. Julian (1971) Detection of a 40–50 day oscillation in the zonal wind in the tropical Pacific, *J. Atmos. Sci.*, 28, 702–708
- Madden, R. A., and P. R. Julian (1972) Description of global-scale circulation cells in the tropics with a 40–50 day period, *J. Atmos. Sci.*, 29, 1109–1123
- Madec G (2008) NEMO, the Ocean Engine. Tech. Rep, Notes de l'IPSL (27), ISSN 1288-1619, Université P. et M. Curie, B102 T15-E5, 4 Place Jussieu, Paris Cedex 5, p. 193
- McCreary, J. P (1981) A linear stratified ocean model of the coastal undercurrent, *Philos. Trans. R. Soc. London*, 298, 603–635
- McCreary, J. P., P. K. Kundu, and R. L. Molinari (1993) A numerical investigation of dynamics, thermodynamics and mixed-layer processes in the Indian Ocean, *Prog. Oceanogr.*, 31, 181–244
- McCreary, J. P., W. Han, D. Shankar, and S. R. Shetye (1996) Dynamics of east India coastal current 2-Numerical solutions, *J. Geophys. Res.*, 101, 13,993-14,010
- McCreary, J. P., R. Furue, T. Jensen, H.-W. Kang, B. Bang, and T. Qu (2007) Interactions between the Indonesian Through flow and circulations in the Indian and Pacific oceans, *Prog. Oceanogr.*, 75, 70–114

- McDonagh, E. L., H. L. Bryden, B. A. King, R. J. Sanders, S. A. Cunningham, and R. Marsh (2005) Decadal changes in the south Indian Ocean thermocline, *J. Climate*, 18, 1575–1590, doi:10.1175/JCLI3350.1
- McPhaden, M. J., G. Meyers, K. Ando, Y. Masumoto, V. S. N. Murty, M. Ravichandran, F. Syamsuddin, J. Vialard, L. Yu, and W. Yu (2009) RAMA: The Research Moored Array for African-Asian-Australian monsoon analysis and prediction, *Bull. Am. Meteorol. Soc.*, 90, 459 – 480
- Meyers, G (1996) Variation of Indonesian through flow and the El Niño–Southern Oscillation, *J. Geophys. Res.*, 101, 12, 255–12,263
- Miller, A., Cayan, D., Barnett, T., Graham, N., and Oberhuber, J (1994). The 1976-77 climate shift of the Pacific Ocean, *Oceanography*, 7(1), 21-26
- Miyama, T., J. P. McCreary, T. G. Jensen, J. Loschnigg, S. Godfrey, and A. Ishida (2003) Structure and dynamics of the Indian Ocean cross-equatorial cell, *Deep Sea Res., Part II*, 50, 2023–2047
- Molinari, R. L., D. Olson, and G. Reverdin (1990) Surface current distributions in the tropical Indian Ocean derived from compilations of surface buoy trajectories, *J. Geophys. Res.*, 95, 7217-7238
- Muraleedharan, P. M (1993) Inter Monsoonal equatorial jets, *Ind. J. Marine Sci.*, 22, 1-7, 1993
- Muraleedharan, P. M., and Prasannakumar, S (1992) Equatorial jet- a case study, *Ind. J. Marine Sci.*, 21,35-45
- Murtugudde, R. and H. Annamalai (2004) Role of the Indian Ocean in regional climate variability. *Ocean–Atmosphere Interaction and Climate Variability*, *Geophy. Mono. Seri.*, No. 147, Amer. Geophys. Union, 213–246, doi: 10.1029/147GM13

- Murtugudde, R., J. P. McCreary and A. J. Busalachi (2000) Oceanic processes associated with anomalous events in Indian Ocean relevance to 1997-98, *J. Geophys. Res.*, 105, 3295-3306
- Nagura, M., and M. J. McPhaden (2008) The dynamics of zonal current variations in the central equatorial Indian Ocean, *Geophys. Res. Lett.*, 35, L23, doi: 10.1029/2008GL035961
- Nagura, M., and M. J. McPhaden (2010a) Dynamics of zonal current variations associated with the Indian Ocean dipole, *J. Geophys. Res.*, 115, 11026, doi: 10.1029/2010JC006423
- Nagura, M., and M. J. McPhaden (2010b) Wyrтки jet dynamics: Seasonal variability, *J. Geophys. Res.*, 115, C07009, doi:10.1029/2009JC005922
- Neelin, J. D., Battisti, D. S. and Hirst, A. C et al (1998) ENSO theory, *J. Geophys. Res.*, 103, 14261–90
- Nidheesh, A. G., M. Lengaigne, Unnikrishnan, A. S, J. Vialard (2013) Decadal and long-term sea level variability in the tropical Indo-Pacific, *Climate Dyn.*, doi:10.1007/s00382-012-1463-4
- Nitta, T., and S. Yamada (1989) Recent warming of tropical sea surface temperature and its relationship to the Northern Hemisphere circulation, *J. Meteor. Soc. Japan*, 67, 375-383
- Nyadjro, E., and M. J. McPhaden (2014) Variability of zonal currents in the eastern equatorial Indian Ocean on seasonal to interannual time scales, *J. Geophys. Res.*, 119, 7969–7986, doi: 10.1002/2014JC010380
- O'Brien, J.J. And H. E. Hurlburt (1974) Equatorial jet in the Indian Ocean: theory, *Science*, 184, 1075-1077
- Ohba, M., and H. Ueda (2006) A role of zonal gradient of SST between the Indian Ocean and the western Pacific in localized convection around the Philippines, *SOLA*, 2, 176–179

Open ocean circulation (2002) University Press, 2nd ed.

Panofsky, H. A., and G. W. Brier (1958) *Some Applications of Statistics to Meteorology*, 224 pp., Pa. State Univ. Press, University Park

Pickard, G. L., and W. J. Emery (1990) *Descriptive Physical Oceanography*, Pergamon Press, New York, 5th Edition

Pierce, D.,W., Barnett ,T.P, AchutaRao, K.M., P. J. Gleckler, Gregory, J.M., Washington, W. M (2006) Anthropogenic warming of the oceans: observations and model results, *J. Climate*, 19(10):1873-1900

Potemra, J. T., and N. Schneider (2007) Interannual variations of the Indonesian Through flow, *J. Geophys. Res.*, 112, C05035, doi:10.1029/2006JC003808.

Potemra, J. T., M. Luther, and J. J. O'Brien (1991) The seasonal circulation of the upper ocean in the Bay of Bengal, *J. Geophys. Res.*, 96, 12 667–12 683

Qiu, Y., L. Li, and W. Yu (2009) Behaviour of the Wyrтки jet observed with surface drifting buoys and satellite altimeter, *Geophys. Res. Lett.*, 36, L18609

Rao, P. S., and D. R. Sikka (2005) Intraseasonal variability of the summer monsoon over the north Indian Ocean as revealed by the BOBMEX and ARMEX field programs, *Pure Appl. Geophys.*, 162(8–9), 1481–1510

Rao, R. R., R. L. Molinari, and J. F. Festa (1989) Evolution of the climatological near surface thermal structure of the tropical Indian Ocean: 1. Description of mean monthly mixed layer depth, and sea surface temperature, surface current, and surface meteorological fields, *J. Geophys. Res.*, 94, 10,801–10,815

Rao, S. A., S. K. Behera, Y. Masumoto, and T. Yamagata (2002) Interannual subsurface variability in the tropical Indian Ocean with a special emphasis on the Indian Ocean dipole, *Deep-Sea Res. II*, 49, 1549–1572

Rao, S. A., and S. K. Behera (2005) Subsurface influence on SST in the tropical Indian Ocean: Structure and interannual variability, *Dynam.Atmos.Ocean*, 39,103-135

Rasmusson, E.M., and Carpenter, T.H (1982) Variations in tropical sea surface temperature and surface wind fields associated with the Southern Oscillation/El Niño, *Mon Weather Rev.*, 110: 354–84.

Rayner, N. A., Parker, D. E., Horton, E. B., Folland, C. K., Alexander, L. V., Rowell, D. P., Kent, E. C., Kaplan, A (2003) Global analyses of sea surface temperature, sea ice, and night marine air temperature since the late nineteenth century, *J. Geophys. Res.*, 108, D14, 440710.1029/2002JD002670.

Reppin, J., F. A. Schott, and J. Fischer (1999) Equatorial currents and transports in the upper central Indian Ocean: Annual cycle and Interannual variability, *J. Geophys. Res.*, 104(C7), 15495-15514

Reynolds, R. W., Rayner, N. A., Smith, T. M., Stokes, D.C. and Wang, W (2002) An improved in situ and satellite SST analysis for climate, *J. Climate*,15,1609–1625

Roemmich, D., and J. Gilson (2009) The 2004–2008 mean and annual cycle of temperature, salinity, and steric height in the global ocean from the Argo program, *Prog. Oceanogr.*, 82, 81–100, doi:10.1016/j.pocean.2009.03.004

Roxy, M. K., Ritika, K., Terray, P., Masson, S (2014) The curious case of Indian Ocean warming, *J. Climate.*, 27 (22):8501-8509, doi:10.1175/JCLI-D-14-00471.1

Roxy, M. K., Ritika, K., Terray, P., Murtugudde, R., Ashok, K., Goswami, B. N (2015) Drying of Indian subcontinent by rapid Indian Ocean warming and a weakening land-sea thermal gradient, *Nature Communications*, 6:7423, doi:10.1038/ncomms8423

Saji, N. H., Goswami, B. N., Vinayachandran, P. N., T. Yamagata (1999) A dipole mode in the tropical Indian Ocean, *Nature* 401:360–363

Saji, N. H, and T. Yamagata (2003) Possible impacts of Indian Ocean Dipole mode events on global climate, *Clim. Res.*, 25, 151–169

Sardeshmukh, P.D., and B.J. Hoskins (1985) Vorticity balances in the tropics during the 1982-83 El Nino/Southern Oscillation event, *Q. J. R. Meteorol. Soc.*, 111, 261-278

Schoenefeldt, R., and Schott, F. A (2006) Decadal variability of the Indian Ocean cross-equatorial exchange in SODA, *Geophys. Res. Lett.*, 33, L08602, doi:10.1029/2006GL025891

Schott, F. A., J. P. McCreary and G. C. Johnson (2004) Shallow overturning circulations of the tropical- subtropical oceans, *Earth Climate: The Ocean- Atmosphere Interaction*, *Geophy. Mono. Seri.*, 147, 261- 304

Schott, F. A., and J. P. McCreary (2001) The monsoon circulation of the Indian Ocean, *Prog. Oceanogr.*, 51, 1–123

Schott, F., M. Dengler, and R. Schoenefeldt (2002) The shallow thermohaline circulation of the Indian Ocean, *Prog. Oceanogr.*, 53, 57–103

Schott, F. A., S.-P. Xie, and J. P. McCreary Jr. (2009) Indian Ocean circulation and climate variability, *Rev. Geophys.*, 47, RG1002, doi:10.1029/2007RG000245

- Schwarzkopf, F., and C. Böning, (2011) Contribution of Pacific wind stress to multi-decadal variations in upper-ocean heat content and sea level in the tropical south Indian Ocean., *Geophys. Res. Lett.*, 38, L12602, doi: 10.1029/2011GL047651
- Shankar, D., P. N. Vinayachandran, A. S. Unnikrishnan (2002) The monsoon currents in the north Indian Ocean, *Prog. Oceanogr.*, 52, 63-120
- Shukla, J., and J. M. Wallace (1983) Numerical simulation of the atmospheric response to equatorial Pacific sea surface temperature anomalies, *J. Atmos. Sci.*, 40, 1613-1630
- Smith, S. L (2001) Understanding the Arabian Sea: Reflections on the 1994–1996 Arabian Sea Expedition, *Deep Sea Res., Part II*, 48, 1385- 1402, doi.org/10.1016/S0967-0645(00)00144-2
- Song, Q., Vecchi, G. A., and Rosati, A. J (2007) Indian Ocean variability in the GFDL coupled climate model, *J. Climate*, 20, 2895–2916, doi:10.1175/JCLI4159.1
- Stewart, R (2008) Introduction to physical Oceanography, Texas A&M University, Department of Oceanography, 2nd ed., 235-254
- Suarez, M. J. and Schopf, P. S (1988) A delayed action oscillator for ENSO, *J. Atmos. Sci.*, 45: 3283–7
- Su, H., J. D. Neelin, and C. Chou (2001) Tropical teleconnection and local response to SST anomalies during the 1997-98 El Nino, *J. Geophys. Res.*, 106, 20025-20043
- Sun, B., Li, H. X. and Zhou, B. T (2019) Inter decadal variation of Indian Ocean basin mode and the impact on Asian summer climate, *Geophys. Res. Lett.*, 46, 21, doi: 10.1029/2019GL085019
- Swapna, P., and R. Krishnan (2008) Equatorial undercurrents associated with Indian Ocean dipole events during contrasting summer monsoons, *Geophys. Res. Lett.*, 35, L14S04, doi: 10.1029/2008GL033430

- Thompson, B., Gnanaseelan, C. and P. S. Salvekar (2006) Variability in the Indian Ocean circulation and salinity and its impact on SST anomalies during dipole events, *J. Mar. Res.*, 64, 853– 880, doi: 10.1357/002224006779698350
- Tomczak, M., and J. S. Godfrey (2001) *Regional Oceanography: An Introduction*, Pergamon Press, New York, pdf version, 175-198
- Trenary, L. L., and W. Han (2012) Intraseasonal-to-interannual variability of South Indian Ocean sea level and thermocline: Remote versus local forcing, *J. Phys. Oceanogr.*, 42, 602–627
- Trenary, L. L., and W. Han (2013) Remote and local forcing of decadal sea level and thermocline depth variability in the south Indian Ocean, *J. Geophys. Res.*, 118, 381–398, doi: 10.1029/2012JC008317
- Trenberth, K. E (1990) Recent observed interdecadal climate changes in the Northern Hemisphere, *Bull. Am. Meteorol. Soc.*, 71, 988–993
- Trenberth, K. E., G. W. Branstor, D. Karoly, A. Kumar, N. C. Lau, and C. Ropelewski (1998) Progress during TOGA in understanding and modeling global teleconnections associated with tropical sea surface temperatures, *J. Geophys. Res.*, 103, 14291-14324
- Uppala, S. M., P. W. Kållberg, A. J. Simmons, U. Andrae, V. Da Costa Bechtold, M. Fiorino, J. K. Gibson, J. Haseler, A. Hernandez, G. A. Kelly, X. Li, K. Onogi, S. Saarinen, N. Sokka, R. P. Allan, E. Andersson, K. Arpe, M. A. Balmaseda, A. C. M. Beljaars, L. Van De Berg, J. Bidlot, N. Bormann, S. Caires, F. Chevallier, A. Dethof, M. Dragosavac, M. Fisher, M. Fuentes, S. Hagemann, E. Hólm, B. J. Hoskins, L. Isaksen, P. A. E. M. Janssen, R. Jenne, A. P. McNally, J.-F. Mahfouf, J.-J. Morcrette, N. A. Rayner, R. W. Saunders, P. Simon, A. Sterl, K. E. Trenberth, A. Untch, D. Vasiljevic, P. Viterbo, and J. Woollen (2005) The ERA-40 re-analysis., *Quart. J. Roy. Meteor. Soc.*, 131, 2961–3012

- Vialard, J., C. Menkes, J-P. Boulanger, P. Delecluse, E. Guilyardi, M. J. McPhaden, and G. Madec (2001) A model study of oceanic mechanisms affecting equatorial Pacific sea surface temperature during the 1997–98 El Niño, *J. Phys. Oceanogr.*, 31,1649–1675
- Vialard, J., Drushka, K., Bellenger, H., M. Lengaigne, Pous, S., Duvel, J.P (2013) Understanding Madden–Julian induced sea surface temperature variations in the North Western Australian basin, *Climate Dyn.*, 41(11–12):3203–3218
- Vinayachandran, P. N., and S. R. Shetye (1991) The warm pool in the Indian Ocean, *Proceedings of Indian Academy of Science (Earth Planetary System Science)*, 100, No.2, 165-175
- Vinayachandran, P. N., N. H. Saji, and T. Yamagata (1999) Response of the equatorial Indian Ocean to an unusual wind event during 1994, *Geophys. Res. Lett.*, 26(11), 1613-1616
- Vinayachandran, P. N., S. Iizuka and T. Yamagata (2002) Indian Ocean Dipole mode events in an ocean general circulation model, *Deep Sea Res., Part II*, 49, 1573-1596
- Vinayachandran, P. N., J. Kurian, and C. P. Neema (2007) Indian Ocean response to anomalous conditions in 2006, *Geophys. Res. Lett.*, 34, L15602, doi: 1029/2007GL030194
- Visbeck, M., and F. Schott (1992) Analysis of seasonal current variations in the western equatorial Indian Ocean: Direct measurements and GFDL model comparison, *J. Phys. Oceanogr.*, 22, 1112–1128
- von Schuckmann, K., F. Gaillard, and P.-Y. Le Traon (2009) Global hydrographic variability patterns during 2003–2008, *J. Geophys. Res.*, 114, C09007, doi:10.1029/2008JC005237
- Wacongne, S., and R. Pacanowski (1996) Seasonal heat transport in a primitive equations model of the tropical Indian Ocean, *J. Phys. Oceanogr.*, 26(12), 2666–2699

Wallace, J.M., E. M. Rasmusson, T. P. Mitchell, V.E. Kousky, E.S. Sarachik, and H. Von Storch (1998) On the structure and evolution of ENSO-related climate variability in the tropical Pacific: Lessons from TOGA, *J. Geophys. Res.*, 103, 14241-14259

Wang, B (1995) Interdecadal changes in El Niño onset in the last four decades, *J. Climate*, 8, 267-285

Webster, P. J., E. F. Bradley, C. W. Fairall, J. S. Godfrey, P. Hacker, R. A. Houze Jr., R. Lukas, Y. Serra, J. M. Hummon, T. D. M. Lawrence, C. A. Russell, M. N. Ryan, K. Sahami, and P. Zuidema (2002) The JASMINE pilot study, *Bull. Am. Meteorol. Soc.*, 83, 1603–1630

Webster, P. J., A. W. Moore, J. P. Loschnigg, and R. R. Leben (1999) Coupled ocean-atmosphere dynamics in the IO during 1997-1998, *Nature*, 401, 356-360

Webster, P. J., and Yang. S (1992) Monsoon and ENSO: selectively interactive systems, *Q. J. R. Meteorol. Soc.*, 118: 877–926

Weng, H., Ashok, K. and Behera, S.K. et al. (2007) Impacts of recent El Niño Modoki on dry/wet conditions in the Pacific Rim during boreal summer, *Climate Dyn.*, 29: 113–29

Williams, A.P., Funk, C (2011) A westward extension of the warm pool leads to a westward extension of the Walker circulation, drying eastern Africa, *Climate Dyn.*, 37 (11-12):2417-2435

Wong, A. P. S., N. L. Bindoff, and J. A. Church (1999) Large-scale freshening of intermediate waters in the Pacific and Indian Oceans, *Nature*, 400, 440–443, doi: 10.1038/22733

Wyrtki, K. (1973) An equatorial jet in the Indian Ocean, *Science*, 181, 262-264

Xie, S. P., H. Annamalai, F. A. Schott, and J. P. McCreary (2002) Structure and mechanisms of south Indian Ocean climate variability, *J. Climate*, 15, 864–878

Xie, S. P., Hu, K., Hafner, J., Tokinaga, H., Du, Y., Huang, G., Sampe, T (2009) Indian Ocean capacitor effect on Indo-western Pacific climate during the summer following El Niño, *J. Climate*, 22:730–747

Xue, Y., and Coauthors, (2012) A comparative analysis of upper-ocean heat content variability from an ensemble of operational ocean reanalyses, *J. Climate*, 25, 6905–6929, doi:10.1175/JCLI-D-11-00542.1

Yamagata, T., S. K. Behera, J. J. Luo, S. Masson, M. R. Jury and S. A. Rao (2004) Coupled ocean atmosphere variability in the tropical Indian Ocean, in *Earth climate: The Ocean-atmosphere Interactions*, Geophys. Mono. Seri, Vol. 147

Yamagata, T., K. Mizuno, and Y. Masumoto (1996) Seasonal variations in the equatorial Indian Ocean and their impact on the Lombok through flow, *J. Geophys. Res.*, 101, 12, 465-12, 473

Yamagata, T., S. K. Behera, S. A. Rao., Z. Guan, K. Ashok, and H. N. Saji (2002) The Indian Ocean dipole: a physical entity, *CLIVAR Exchanges*, 24, 15–18, 2002

Yang, J., Q. Liu, S. P. Xie, Z. Liu, and L. Wu (2007) Impact of the Indian Ocean SST basin mode on the Asian Summer monsoon, *Geophys. Res. Lett.*, 34, L02708, Doi: 10.1029/2006GL028571

Yang, S., and Jiang, X (2014) Prediction of eastern and central Pacific ENSO events and their impacts on East Asian climate by the NCEP climate forecast system, *J. Climate*, 27, 4451–72

Yokoi, T., T. Tozuka and T. Yamagata (2008) Seasonal variation of the Seychelles Dome, *J. Climate*, 21, 3740–3754

Yu, L., O'Brien, J. J., Yang, J (1991) On the remote forcing of the circulation in the Bay of Bengal, *J. Geophys. Res.*, 96, 20449-20454

Yu, W., B. Xiang, L. Liu, and N. Liu (2005) Understanding the origins of interannual thermocline variations in the tropical IO, *Geophys. Res. Lett.*, 32, L24706

Yuan, D., and W. Han (2006) Roles of equatorial waves and western boundary reflection in the seasonal circulation of the equatorial Indian Ocean, *J. Phys. Oceanogr.*, 36, 930–944

Yuan, Y., and Yang, S (2012) Impacts of different types of El Niño on the East Asian climate: focus on ENSO cycles, *J. Climate*, 25: 7702–22

Yule, U. G., and M. G. Kendall (1950) *An Introduction to the Theory of Statistics*, 701 pp., Hafner, New York

Zhang, Y. C., Rossow, W. B., Lacis, A. A., Oinas, V., Mishchenko, M. I (2004) Calculation of radiative fluxes from the surface to top of atmosphere based on ISCCP and other global data sets refinements of the radiative transfer model and the input data, *J. Geophys. Res.*, 109, 27

Zhang, D., McPhaden, M. J., Lee, T (2014) Observed interannual variability of zonal currents in the equatorial Indian Ocean thermocline and their relation to Indian Ocean Dipole, *Geophys. Res. Lett.*, 41:7933–7941, doi: 10.1002/2014GL0614

List of Publications

Sachidanandan, C., Lengaigne, M., Muraleedharan, P. M., Mathew, B (2017) Inter annual variability of zonal currents in the equatorial Indian Ocean: respective control of IOD and ENSO, Ocean Dyn.,doi:10.1007/s10236-017-1061-4